# OBJECT DETECTION PERFORMANCE ANALYSIS AND IMPROVEMENTS FOR PASSIVE GLOBAL NAVIGATION SATELLITE SYSTEM BASED SYNTHETIC APERTURE RADAR

ZHENG, YU

PhD

The Hong Kong Polytechnic University

2019

The Hong Kong Polytechnic University

Department of Land Surveying and Geo-informatics

# Object Detection Performance Analysis and Improvements for Passive Global Navigation Satellite System based Synthetic Aperture Radar

ZHENG, Yu

A thesis submitted in partial fulfillment of the requirements for the degree

of Doctor of Philosophy

June 2018

# CERTIFICATE OF ORIGINALITY

I hereby declare that this thesis is my own work and that, to the best of my knowledge and belief, it reproduces no material previously published or written, nor material that has been accepted for the award of any other degree or diploma, except where due acknowledgement has been made in the text.

_____(Signed)

ZHENG, Yu (Name of student)

# Abstract

Passive Global Navigation Satellite System (GNSS)-based Synthetic Aperture Radar (SAR), known as GNSS-SAR, is a currently developing passive radar sensing system. As the system works in passive mode, GNSS-SAR is much cheaper with a much smaller size, thus it is more flexible to be installed under many application scenarios. However because of the restriction of GNSS signal bands, the resolution of GNSS-SAR is lower than conventional SAR. Also, the weak reflected GNSS signals is another limitation for the application of GNSS-SAR. Due to the fact that GNSS signals are low Equivalent Isotropically Radiated Power (EIRP) sources, the signal strength after reflection will be very weak.

In this study, a new GNSS-SAR imaging algorithm is proposed to improve object detectability under weak reflected signals. Both theoretical analysis and experimental study show that the proposed algorithm can result in obviously enhanced imaging detectability. For instance, using GPS C/A code signal receiver, the proposed algorithm can detect the object with the signal strength as low as $-160$ dBm, while the conventional algorithm cannot. Meanwhile, computation with the proposed imaging algorithm is significantly more efficient than with conventional GNSS-SAR imaging algorithm.

To enhance range resolution, two new range compression algorithms are pro-

posed to reduce the compressed ambiguity of main-lobe due to chip rate of the respective pseudo-random noise (PRN) code, respectively. In first proposed algorithm (see Chapter 4), range compression is carried out by correlating a reflected GNSS intermediate frequency (IF) signal with a synchronized direct GNSS base-band signal at range domain, where the main lobe ambiguity of the compressed pulse is narrowed down. Thereafter, spectrum equalization technique is applied to the compressed results for suppressing side lobes to obtain a final range-compressed signal. In the second proposed algorithm (see Chapter 5), the main-lobe ambiguity of range compressed signal is deduced by applying Diff2 peak extraction method. Both simulation and field experimental results demonstrate that the proposed range compression algorithms contribute to the resolution enhancement very significantly. For example, on the basis of GPS C/A code receiver platform with the IF value 4 MHz and sampling rate 16 MHz, the first proposed algorithm can improve the best attainable range resolution to 40 m level, while the second proposed algorithm can enhance the best attainable range resolution to 36 m level, compared to the best attainable range resolution 171 m provided by conventional range compression algorithm. In contrast with many current GNSS-SAR research works, the major novelty of the proposed range compression algorithms is that range compressed pulse ambiguity caused by PRN code correlation function has been addressed successfully.

**Key Words**: Global Navigation Satellite System, Synthetic Aperture Radar, GNSS-SAR, object detection performance, weak reflected signals, range resolution

# Publications arising from the thesis

[1 ] **Y. Zheng***, Y. Yang and W. Chen, 'Enhanced GNSS-SAR Range-Doppler Algorithm for The Target Detection of Weak Reflected Signals: An Experimental Study', *Journal of Aeronautics, Astronautics and Aviation, Series A*, Vol. 49, No. 2, pp. 83–92, 2017.

[2 ] **Y. Zheng***, Y. Yang and W. Chen, 'An New Imaging Algorithm for Passive GNSS-Based SAR under Weak Reflected Signals', *Radio Science* (Under Review).

[3 ] **Y. Zheng***, Y. Yang and W. Chen, 'Analysis of Radar Sensing Coverage of a Passive GNSS-Based SAR System', *2017 IEEE International Conference on Localization and GNSS (ICL-GNSS 2017)*, Nottingham, UK, June 2017, DOI: 10.1109/ICL-GNSS.2017.8376246.

[4 ] **Y. Zheng***, Y. Yang and W. Chen, 'A Novel Range Compression Algorithm for Resolution Enhancement in GNSS-SARs', *Sensors*, Vol. 17, No. 7, p. 1496, 2017.

[5 ] **Y. Zheng**$^*$, Y. Yang and W. Chen, 'Ocean Ship Sensing Using Passive GNSS-based SAR', *2017 International Symposium on GNSS (ISGNSS 2017)*, Hong Kong, December 2017.

[6 ] **Y. Zheng**$^*$, Y. Yang and W. Chen, 'Object Identification in Passive GNSS-based SAR under Background Scattering', *Journal of GPS* (Under Review).

[7 ] **Y. Zheng**$^*$, Y. Yang and W. Chen, 'A New Imaging Algorithm for Range Resolution Improvement in Passive GNSS-based SAR', *IET Radar Sonar & Navigation* (Under Review).

[8 ] Y. Yang, **Y. Zheng**, W. Yu, W. Chen and D. Weng, 'Deformation Monitoring Using GNSS-R Technology', *Advances in Space Research* (Under Review).

$*$ corresponding author

# Acknowledgements

First and foremost, my sincere appreciation should go to my supervisor, Prof. Wu Chen, for his meticulous guidance on both the issues arising from my research project and good writing skills for technical publications. This thesis can never be possible without his constructive suggestions.

I am grateful to the lab colleagues including Mr. Yang Yang, Dr. Duojie Weng, Dr. Rui Xu, Mr. Walid Darwish, etc very deeply for the guidance on programming and discussions of some specific research issues. Meanwhile, my special thanks goes to Office of Student Resources and Residential Life, The Hong Kong Polytechnic University, for offering me student hall tutorship at the second and third years of my PhD program. Not only an excellent accommodation is provided for promoting my study, but also my social ability has been cultivated.

Last but not the least, I am very thankful to my parents, Prof. Linhua Zheng and Mrs. Xiaoli Mo, for their continuous support. This thesis is dedicated to them.

# Table of Contents

# List of Tables

# List of Figures

# List of Abbreviations

| Acronyms | Definition |
|---|---|
| SAR | synthetic aperture radar |
| RAR | real aperture radar |
| GNSS | global navigation satellite system |
| GNSS-R | GNSS-reflectometry |
| GPS | global positioning satellite |
| CDMA | code division multiple access |
| FDMA | frequency diversion multiple access |
| BPSK | binary phase shift keying |
| QPSK | quadrature phase shift keying |
| DSSS | direct spread spectrum sequence |
| C/A code | coarse acquisition code |
| P code | encrypted precision code |
| SNR | signal to noise ratio |
| PRN | pseudo-random noise |
| ISAR | inverse synthetic aperture radar |

| | |
|---|---|
| PDF | probability density function |
| CDF | cumulative density function |
| dB | decibel |
| ms | mini-seconds |
| ROC | receiver operating characteristic |
| RF | radio frequency |
| IF | intermediate frequency |
| FOV | field of vision |
| AWGN | additive white Gaussian Noise |
| Diff2 | second order differentiation |
| DDM | delay Doppler mapping |

# List of Symbols

| Symbols | Definition |
|---|---|
| $s(\cdot)$ | transmitted GNSS signal |
| $A$ | transmitted GNSS signal magnitude |
| $C(\cdot)$ | pseudo-random noise code |
| $D(\cdot)$ | navigation bit |
| $f_c$ | transmitted frequency |
| $n$ | transmitted sample |
| $s_d(\cdot)$ | received direct GNSS signal |
| $A_d$ | received GNSS signal magnitude at direct channel |
| $A_r^l$ | reflected magnitude per scattering point |
| $t$ | range domain |
| $u$ | azimuth domain |
| $j$ | imaginary unit |
| $\tau$ | direct GNSS signal delay relative to |
| $\exp(\cdot)$ | exponential function |

| | |
|---|---|
| | transmitted signal |
| $f_d$ | Doppler frequency |
| $\phi_d$ | carrier phase of direct signal |
| $n_d$ | background noise at direct channel |
| $l$ | reflecting point |
| $s_R^l$ | received reflected GNSS signal per reflected point |
| $A_R^l$ | reflected magnitude per reflecting point |
| $\tau_r^l$ | reflecting delay relative to direct signal |
| $\phi_r^l$ | reflected phase per reflecting point |
| $n_r^l$ | background noise per reflecting point |
| $s_r(\cdot)$ | reflected GNSS signals |
| $s_{m\_f}$ | imaging matched filter |
| $T_{N_s-1,u}^r$ | range compressed signal based on conventional GNSS-SAR imaging algorithm |
| $*$ | conjugate |
| $N_t$ | range sample quantity of digitized GNSS signal at receiver |
| $M_u$ | azimuth sample quantity of digitized GNSS signal at receiver |
| $N_s$ | range samples for compression |
| $i$ | number of azimuth cell |

| | |
|---|---|
| $k_2$ | number of azimuth samples per cell |
| $M_s$ | total sample quantity per azimuth cell |
| $I^i_{(N_s-1)\times(M_s-1)}$ | the matrix of azimuth compressed signal per azimuth cell |
| $I^m$ | the matrix of final obtained GNSS-SAR image |
| $\|\cdot\|$ | absolute value |
| $P_f$ | false alarm probability in Chapter 3 with respect to the conventional imaging algorithm |
| $P_d$ | detection probability in Chapter 3 with respect to the conventional imaging algorithm |
| $\epsilon$ | detection threshold in Chapter 3 for the conventional imaging algorithm |
| $P_{f_p}$ | false alarm probability in Chapter 3 with respect to the proposed imaging algorithm |
| $P_{d_p}$ | detection probability in Chapter 3 with respect to the proposed imaging algorithm |
| $P_t$ | GNSS satellite transmission power |
| $G_t$ | GNSS satellite transmission antenna gain |

| | |
|---|---|
| $G_r$ | surveillance antenna gain |
| $\sigma_{\mathrm{RCS}}$ | object radar cross section |
| $R_t$ | distance between GNSS satellite and earth object |
| $R_r$ | distance between object and GNSS-SAR receiver |
| $k$ | Boltzmann constant |
| $T$ | environmental temperature expressed in Fahrenheit |
| $B$ | signal bandwidth (PRN code chip rate) |
| $A_s^2$ | signal energy in Chapter 3 |
| $\sigma^2$ | noise energy in Chapter 3 |
| $\gamma$ | received reflected SNR |
| $\gamma_r$ | range compressed SNR in Chapter 3 with regard to conventional GNSS-SAR imaging algorithm |
| $\gamma_a$ | azimuth compressed SNR per azimuth cell in Chapter 3 with regard to conventional GNSS-SAR imaging algorithm |
| $H_0$ | absence of an object |
| $H_1$ | presence of an object |
| $m_s$ | non overlapped mini-slot per azimuth cell |
| $T^{r_p}_{N_s-1,\lfloor u/m_s \rfloor}$ | range compressed signal in Chapter 4 |

| | |
|---|---|
| | with regard to the proposed GNSS-SAR imaging algorithm |
| $\gamma_{r_p}$ | range compressed SNR in Chapter 3 with regard to the proposed GNSS-SAR imaging algorithm |
| $T^{a_p}_{(N_s-1)\times(\lfloor M_s/m_s \rfloor-1)}$ | azimuth compressed signal per azimuth cell in Chapter 3 with regard to the proposed GNSS-SAR imaging algorithm |
| $\gamma_{a_p}$ | azimuth compressed SNR per azimuth cell in Chapter 3 with regard to the proposed GNSS-SAR imaging algorithm |
| $\Delta\varphi$ | phase difference between direct and reflected GNSS signals |
| $P_{f_1}$ | false alarm probability in Chapter 6 with regard to identifying object presence GNSS-SAR image |
| $P_{d_1}$ | detection probability in Chapter 6 with regard to identifying object presence GNSS-SAR image |
| $P_{f_2}$ | false alarm probability in Chapter 6 with regard to object extraction |
| $P_{d_2}$ | detection probability in Chapter 6 |

| | |
|---|---|
| | with regard to object extraction |
| $\circledast$ | arithmetic correlation |
| $\Lambda(\cdot)$ | triangle function |
| $\delta_{R_1}$ | range resolution in Chapter 4 with respect to conventional range compression algorithm |
| $s_{r_2}$ | reflected GNSS signal of intermediate frequency |
| $f_{\mathrm{IF}}$ | intermediate frequency (IF) |
| $\mathcal{F}$ | Fourier transform |
| $\mathcal{F}^{-1}$ | inverse Fourier transform |
| $R_{c\_\mathrm{proposed}}$ | Final range compressed signal of the proposed range compression algorithm in Chapter 6 |
| $\delta_{R_2}$ | range resolution in Chapter 4 with respect to the proposed range compression algorithm |
| $s_{m_{\mathrm{IF}}}$ | synchronized direct IF GNSS signal |
| $W$ | spectrum equalization window |
| $c$ | speed of light |
| $\beta$ | bi-static angle |
| $T_s$ | considered duration for performing range compression in Chapter 4 |

| | |
|---|---|
| $\mathcal{O}$ | arithmetic complexity |
| $f_s$ | sampling frequency of GNSS receiver |
| $R_{\text{in}}$ | intermediate range compressed signal in Chapter 5 |
| $N_R$ | total reflected signal samples |
| $\frac{\partial^2}{\partial x^2}$ | second order differentiation |
| $R_p$ | range compressed signal in Chapter 5 with respect to the proposed algorithm |

# Chapter 1

# Introduction

In recent decade, a novel developing passive radar imaging system – Passive Global Navigation Satellite System (GNSS) based Synthetic Aperture Radar (SAR), GNSS-SAR, has been attracted many research interests in the GNSS community. In contrast with the conventional SAR system, signals from Global Navigation Satellite Systems (GNSSs) such as the global positioning system (GPS), Galileo, GLONASS or Beidou are applied for SAR image formation. As the advantages of ready-to-use signal (no SAR transmitter is required), GNSS-SAR has a less cost budget and the system is more flexible to be installed for the various application scenarios. However, currently, object detection performance for such technique is limited by the two main problems – weak signal strength and low range resolution. Thus to address the two main problems is very crucial for promoting the applications of GNSS-SAR.

This chapter begins with the introduction of background of the research work,

followed by the research motivation, objective and contribution. At the final section of this Chapter, the structure of this thesis is given.

## 1.1 Research Background

The reflectometry technique – radar, which is the abbreviation of Radio Detection and Ranging, has been developing since the Second Word War period, and mainly used for object detection and classification [1, 2, 3, 4, 6]. In general, radar system contains the two types – Real Aperture Radar (RAR) [4] and Synthetic Aperture Radar (SAR) [1, 2, 4]. The major difference between RAR and SAR is that RAR uses a fixed short antenna for acquiring data, while SAR uses a long stationary antenna or a short antenna with moving platform for acquiring data [1, 2, 4]. Therefore SAR can provide a higher resolution than RAR. In radar system, magnitude information (obtained from radar images) and phase information (obtained from radar data tracking) are the two main parameters that extracted for the purpose of remote sensing investigations. Using magnitude and phase information, till now, radar technique has been implemented under a wide range remote sensing studies such as civil and military reconnaissance, forest coverage monitoring, surface deformation monitoring, etc. However because both transmitter and receiver need to be specifically designed and constructed, conventional active radar reflectometry system has a high cost budget and limited flexibility for the installation under various surveillance scenario. To deal with

this issue, passive reflectometry technique [6, 23, 31] was proposed and has been developing. In general, passive reflectometry system works under the mode that a passive receiver uses echo signals of other source as transmission of opportunity from reflecting surface. As no transmission module is used, passive reflectometry system is more cost effective for the construction under various implementation scenarios. Moreover the passive reflectometry receiver can be relatively safe concealed when performing reconnaissance, as the system only collects data, no one can detect it [23]. Currently the signals such as digital audio or TV signals [7, 8], FM signal [9], mobile communication signals [10, 11, 13] and global navigation satellite system (GNSS) signal [14, 20, 23, 92] have been demonstrated for passive surveillance purpose. Among them, the usage of GNSS signals is one of the most popular, which is known as GNSS reflectometry (GNSS-R). This is because as GNSS signals are global coverage and rarely fail to transmit, all day and all weather monitoring can be possible [23]. The concept GNSS-R was firstly proposed in [15]. Generally, traditional GNSS-R technique includes the two main categories – non-geometrical and geometrical methods. The measurement of non-geometrical method is based on the received signal power or signal to noise ratio (SNR), while the measurement of geometrical method is based on code delay between direct and reflected GNSS signals. Till current, various applications of traditional GNSS-R technique have been developing. The respective applications can be seen in sea state monitoring [16], biomass monitoring [17], soil moisture monitoring [18] and snow depth estimation [19], etc. To form radar images for

object detection and identification, recently, based on the concept of radar as aforementioned, traditional GNSS-R technique was further extended to GNSS radar technique. Similar to active radars, passive GNSS based radars also contain passive GNSS-based RAR and passive GNSS-based SAR (GNSS-SAR). This thesis particularly concentrates on GNSS-SAR technique, where SAR imaging algorithms for object detection are specifically investigated. As GNSS signals are low Equivalent Isotropically Radiated Power (EIRP) sources that not originally designed for remote sensing purpose, in GNSS-SAR surveillance, weak reflected GNSS signals and low range resolution are the two main problems. The detailed interpretations of the problems can be seen as follows:

- Weak reflected signals is mainly caused by the power budget of GNSS satellite, distance between GNSS satellite and earth surface, object reflectivity as well as the scattering path from object to GNSS-SAR receiver [12, 93, 69]. For instance, the transmission power of GNSS satellite is 50 w; the distance between satellites and earth is with the order of magnitude $10^7$ m [23, 24, 97]. Thus GNSS power flux density near the earth surface is extremely low at the level around $-130$ dBm [101]. The situation will become even worse for reflected GNSS signals for SAR purpose. The case that reflected signal strength as weak as $-160$ dBm can happen. With such low power density, GNSS-SAR images can be very noisy and it will be difficult to identify objects in the images.

- Low range resolution is another main problem that restricts the current implementation of GNSS-SAR technique [69]. Due to the low range resolution, if the two or more targets are placed in a closer range distance, they may not be able to be separated on the corresponding GNSS-SAR image. GNSS signal bandwidth and bi-static angle for sensing determine the range resolution level [23, 31]. With a fixed bi-static angle, GNSS signals bandwidth is the only factor that determines range resolution [23, 31]. Under this circumstance, if shape factors of a wave form are not considered, the best attainable range resolution identically equals the reciprocal of doubled signal bandwidth value. And for GNSS signals, the bandwidth value is equal to the pseudo-random noise (PRN) code chip rate [23, 31]. Since the chip rates of GPS C/A code signal, GLONASS signal, GPS P code signal and Beidou signal, joint Galileo E5 signal are 1.023 MHz, 5.11 MHz, 10.23 MHz and 50 MHz, respectively, the respective best range resolutions can be obtained at the levels 150 m, 30 m, 15 m and 3 m [29, 36, 37, 66, 67, 68, 23, 31, 44, 33, 49, 32, 53, 54, 55, 71, 98].

## 1.2 Recent Development in GNSS-SAR Research

Conventionally, GNSS-SAR imaging procedure contains two separated compressions i.e. range compression and azimuth compression [23, 31]. Based on the conventional algorithm, in recent years, the feasibility of GNSS-SAR has been

demonstrated by different research groups[29, 30, 32, 33, 35, 40, 41, 43, 44, 92], using various system configurations. Long dwell time on the target for providing an increased coherent duration for azimuth compression is commonly used for dealing with weak reflected signal problem.

For resolution study, under the conventional imaging algorithm, with a fixed bi-static angle, currently many works prefer to use the GNSS signals with a higher PRN code chip rate, as the matter of fact that a higher range resolution can be achieved. For example, the current best range resolution is achieved at 3 m level in the works [54, 55] that uses joint Galileo E5 signal with a code chip rate 51.115 MHz. At the same time, azimuth resolution is determined by carrier phase history, using the dwell time 5 min, azimuth resolution can be achieved at the level 3 to 4 meter [56, 96, 97, 98]. Because of this, the works [56, 96, 97, 98] improve spatial resolution based on azimuth resolutions diversity. In specific, GNSS-SAR signals are acquired through different azimuth direction for forming a group of bi-static images, where each bi-static images are generated by conventional imaging algorithm. Thereafter to exploit spatial diversity, multi-static image fusion approach is applied to the group of bi-static images.

In terms of applications, the works [38, 48, 93] demonstrated GNSS-SAR implementations in surface change monitoring by comparing the correlation coefficient of two SAR images. At the same time, the works [57, 58, 59] applied GNSS-SAR techniques in maritime monitoring based on delay Doppler mapping (DDM).

However, the current research still has the following problems:

- Although weak reflected signal negatively impacts GNSS-SAR imaging, few related works have discussed the method to address it. Increasing the integration length is a common method improve signal strength [24, 25, 21, 94, 95] for improving the detectability, however this process can add significant increment of the computational burdens for GNSS-SAR. This is because the integration is carried out on the basis of signal correlation processing when performing range and azimuth compressions.

- For resolution improvement, as aforementioned, range resolution is limited by the ranging code chip rate of the utilized GNSS signals under a fixed bi-static observation angle. Even though multi-image fusion approach using GNSS-SAR images that generated from different azimuth direction can promote spatial resolution than single azimuth direction case [56, 96, 97, 98], the approach still do nothing about range compressed pulse ambiguity region caused by the PRN code correlation function that due to the respective code chip rate. Meanwhile another shortcoming of the approaches [56, 96, 97, 98] is that the methods are time consumptive because they are applied based on the multiple full preliminary GNSS-SAR images.

## 1.3 Research Motivation and Objectives

This research is mainly motivated by the main problems in GNSS-SAR and the drawbacks in the respective current research. The main aim of this thesis is to

improve object detection performance for GNSS-SAR. To achieve the main aim, the following objectives are contained:

- Improving signal detectability and reducing computational complexity for GNSS-SAR imaging simultaneously by combining addition and correlation scheme for azimuth processing.

- Improving range resolution by addressing range compressed pulse main-lobe ambiguity caused by PRN code correlation function.

## 1.4 Thesis Contributions

Working towards the objectives, the main contributions of this thesis are listed as follows.

- Based on the point that joint coherent and non-coherent integration can better improve SNR than either single coherent or single non-coherent integration [21], we propose a new imaging algorithm to improve the image quality for GNSS-SAR under weak reflected signals, where imaging quality is quantified by compressed signal strength and the respective detection probability. In the proposed algorithm, each pre-determined azimuth resolution cell is further divided into multiple non-overlapped mini-slots. Then to both enhance imaging signal detectability for object identification and reduce the computational times, the azimuthally distributed range compressed of migration correction within each mini-slot are added together for

azimuth compression. Theoretical analysis and experimental results both indicate that the proposed algorithm is apparently less strict in its signal strength requirements with a given object detection probability, and can show significantly greater detectability under the typical weak reflected signal scenario, compared to the conventional GNSS-SAR imaging algorithm. Using a GPS C/A code signal receiver as an example, the objects with a reflected signal strength $-160$ dBm can still be imaged under the proposed algorithm, but the conventional algorithm cannot. At the same time, the proposed algorithm is obviously more time efficient than the conventional GNSS-SAR imaging algorithm.

- Novel range compression algorithms are proposed on the basis of reducing range compressed ambiguity of the main-lobe. In one of the proposed algorithms (see Chapter 4), reflected GNSS intermediate frequency (IF) signals are employed to correlation with synchronized direct base-band signal for range compression, in which, the main-lobe ambiguity is deducted. The side-lobes are suppressed by spectrum equalization method. For the other proposed algorithm (see Chapter 5), to narrow down range compressed ambiguity, Diff2 scheme [105] for correlation peak extractions under multi-path scenario is applied on range compressed signals. Both simulation and field experimental results have successfully demonstrated that the proposed algorithms can significantly improve range resolution for GNSS-SAR. In specific, for GPS C/A code signal receiver, the range resolution can be improved to

40 m from 171 m with the IF value 4 MHz; with Diff2 scheme, under the range sampling frequency $1.6 \times 10^7$ Hz, range resolution is enhanced to 36 m level. In summary, the proposed range compression algorithms have addressed range compressed ambiguity issue caused by GNSS signal, and this is the major innovation compared to many current GNSS-SAR related works.

Apart from the main contributions, we implement GNSS-SAR under several environmental sensing scenarios by combining all the proposed algorithms in this thesis. Radar sensing distance and maritime ship identification with ocean background interference are specifically studied. The field results show that with such a low cost GNSS software defined receiver, targets of the field of vision (FOV) around 2 km can be clearly identified on GNSS-SAR image. Meanwhile, the capability of GNSS-SAR to perform maritime ship identification under ocean background scattering is verified. In summary, the results from the application study show that when compared with conventional imaging algorithm, comprehensively combining the proposed algorithms are better for the GNSS-SAR applications.

## 1.5 Thesis Outline

The thesis is organized as follows.

In Chapter 2, we introduce the system, signal model and imaging procedure of GNSS-SAR. Meanwhile we review the current development of such technique, and point out the associated problems.

The proposed GNSS-SAR imaging algorithm for enhancing image quality under weak reflected signals is given and analyzed in Chapter 3. Both simulations and field experiments are carried out to validate the proposed algorithm.

In Chapter 4, the proposed novel range compression algorithm using reflected GNSS IF signals for imaging is given and analyzed. The relevant theoretical derivation, simulation and field experimental results are provided.

Another new range compression algorithm on the basis of applying Diff2 peak extraction scheme on range compressed signals in shown in Chapter 5. The simulation and experimental confirmations are given in the same chapter.

Chapter 6 implements GNSS-SAR into several environmental sensing scenarios as examples. Radar sensing distance and maritime ship identification under ocean background scattering are investigated.

Chapter 7 concludes the thesis and presents the future development.

# Chapter 2

# Principle of GNSS-SAR

In this chapter, at the beginning, the concept of SAR, the GNSS-SAR system and signal model are introduced, respectively. Thereafter, the general step of imaging is provided, and the associated main problems – weak reflected signals and low range resolutions are analyzed, and the associated disadvantages are pointed out.

## 2.1 Concept of SAR

In general, most active SAR transmitters transmit the radio signal in the form of chirp signal [22] for surveillance purpose, and SAR receiver collect radio echo signals from the objects through a moving platform with a certain trace [1, 2, 4]. The trace can be either direct moving trace or angular moving trace. The overall diagram of SAR can be seen in Fig. 2.1.

In Fig. 2.1, it can be seen that to form a SAR image, data are collected through

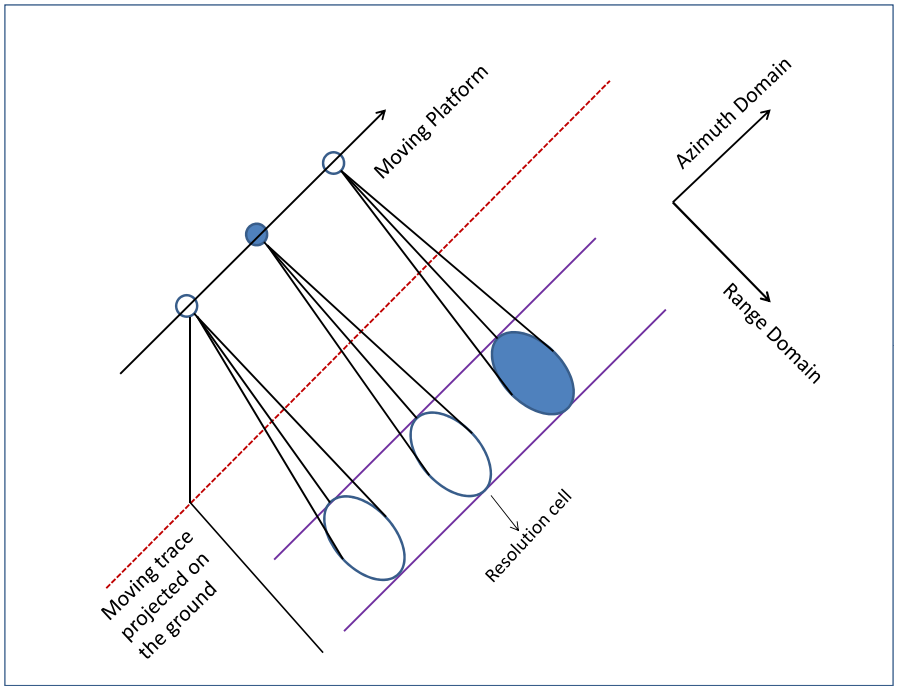


Fig. 2.1: The overall diagram of SAR system.

two dimensions. The dimension that perpendicular to the moving trace is known as range domain, while the dimension that parallel to the moving trace is known as azimuth domain. For SAR receiver, generally it can be categorized into three modes – mono-static mode, bi-static mode and multi-static mode. The respective schematic diagrams can be seen as Fig. 2.2. For mono-static SAR receiver, both transmitter and receiver are located in the same platform. For bi-static SAR receiver, the transmitter and receiver are located on separated platforms, and only one receiver is employed for receiving signals from the transmitter. As for multi-static SAR, multiple separated transmitters and multiple receivers (two or more) can be used for transmitting and receiving signals. In SAR system, with a sufficient received echo signal strength, by carrying out the separated compressions in both range and azimuth domains, a fine pulse response of a scattering point for

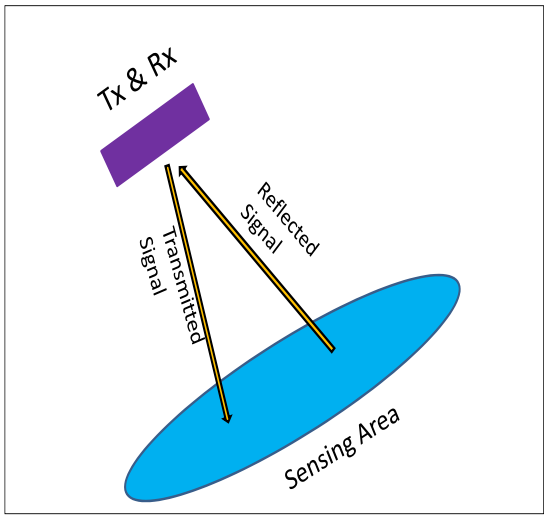


(a)

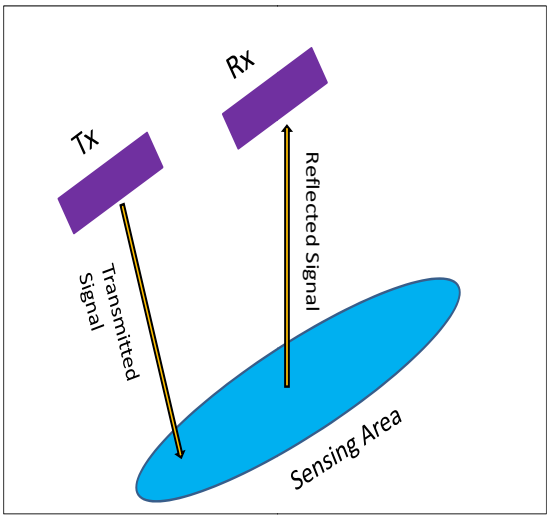


(b)

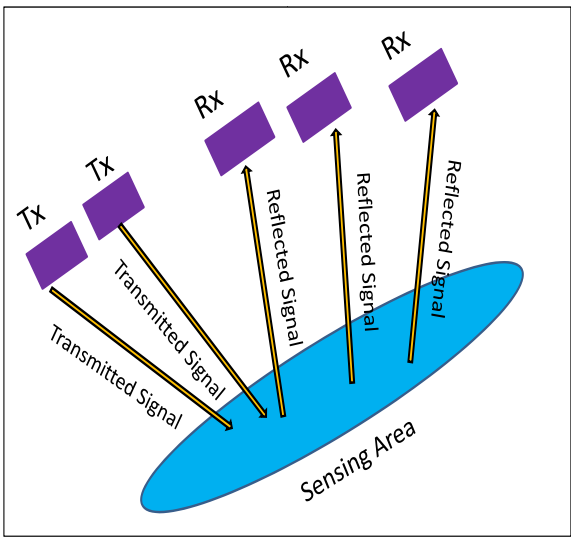


(c)

Fig. 2.2: The SAR receiver mode: (a) mono-static SAR, (b) bi-static SAR, (c) Multi-static SAR.

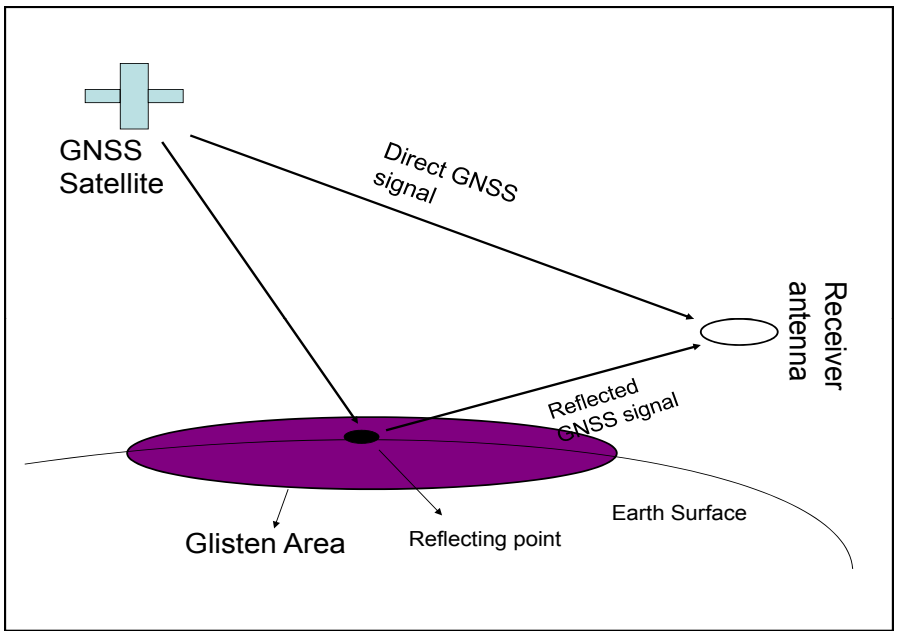


Fig. 2.3: The overall schematic diagram of GNSS-SAR.

object identification can be obtained.

The current applications of SAR can be summarized as oceanography (wave spectra, wind speed, velocity of ocean currents), glaciology (snow wetness, snow water equivalent, glacier monitoring), agriculture (crop classification and monitoring, soil moisture), geology (terrain discrimination, subsurface imaging), forestry (forest height, biomass, deforestation), deformation monitoring (volcano, Earthquake and subsidence monitoring with differential interferometry), environment monitoring (oil spills, flooding, urban growth, global change) etc [5].

## 2.2 GNSS-SAR System and Signal Model

Based on the concept of SAR, a new SAR system known as GNSS-SAR was proposed. The overall schematic diagram of GNSS-SAR is shown in Fig. 2.3.

In Fig. 2.3, it can be seen that generally GNSS-SAR consists the following segments.

- GNSS satellite(s): source of opportunity for transmitting GNSS signals,
- glisten area: the interested region for remote sensing observation,
- direct and surveillance receiving antennas: collect direct and reflected signals respectively, and generally direct antenna is faced to sky while surveillance antenna is faced to the glisten area.

### 2.2.1 GNSS Signals

GNSS, the short form of Global Navigation Satellite System, is known as satellite-based system with a global coverage that transmits signals for navigation and positioning [24, 23, 25, 31]. Currently GNSS contains GPS, GLONASS, Galileo and Chinese Beidou systems, respectively.

- GPS [24, 25, 75] was developed by Unite States in 1970 s, and it is the first global positioning satellite system for offering in both civil and military purpose. The system contains 24 satellites. The system is operated in code division multiple access (CDMA) [81, 82, 83, 84] mode with binary phase shift keying (BPSK) modulation [80, 81]. All the satellites transmit within the same frequency band. Different Pseudo-random Noise (PRN) codes [70] are employed to distinguish different satellites. Two kinds of PRN codes i.e.

coarse acquisition (C/A) code and Precision (P) code are used, in which, C/A code is for civil service while P code is for military service.

- GLONASS [23, 26] was developed by Russia in 1976. Till now, the system contains 24 satellites. Like GPS, the PRN codes P code and C/A code are employed in GLONASS system. However different from GPS, P code and C/A code are the same for all satellites, frequency division multiple access (FDMA) [81] scheme is used to distinguish each satellite.

- In recent decade, European Union developed a new GNSS system – Galileo system [27]. Since 2008, Galileo system has been commercially operated. The full constellation of the system is planed to be completed by 2020. The same as GPS, in Galileo system, all the satellites are modulated in the same frequency band. Unlike GPS and GLONASS, Galileo system PRN codes are contained by primary code and secondary code. Primary code is the same for all satellites but secondary code varies from satellite to satellite. Quadrature phase shift keying (QPSK) [81] is utilized for modulating the transmission signals.

- Beidou [28] is a newly developing GNSS satellite by Chinese scientists. Till now 15 satellites are in the sky. The full system is hopefully be developed by the year 2020. Thirty five satellites will be consisted in the fully developed system. The same as GPS, CDMA scheme is adopted in Beidou system as well. Two kinds of PRN codes are used to distinguish each satellite. The

TABLE 2.1: Parameter values of GPS and GLONASS satellites

| GNSS | GPS | GLONASS |
|---|---|---|
| Channel | L1, L2 and L5 | L1 and L2 |
| Operating frequency | L1 = 1575.42 MHz | L1 = $1602 + n \times 0.5625$ MHz |
| | L2 = 1227.6 MHz | L2 = $1246 + n \times 0.4375$ MHz |
| | L5 = 1176.45 MHz | |
| Chip rate (M/s or MHz) | C/A code: 1.023 | C/A code: 0.511 |
| | P code: 10.23 | P code: 5.11 |
| Orbit altitude (km) | 22200 | 19130 |

TABLE 2.2: Parameter values of Galileo and Beidou satellites

| GNSS | Galileo | Beidou |
|---|---|---|
| Channel | E5a, E5b, E6 | B1, B2, B5 and B6 |
| Operating frequency | E5a = 1176.45 MHz | B2 = 1561.098 MHz |
| | E5b = 1207.14 MHz | B5 = 1207.14 MHz |
| | E6 = 1278.75 MHz | B6 = 1268.52 MHz |
| | | B1 = 1575.42 MHz |
| Chip rate (M/s or MHz) | E5 signal: 20.460 | B2 and B5b-I signals: 2.046 |
| | E5b-Q and E6 signals: 10.23 | |
| Orbit altitude (km) | 23222 | 21150 |

localization accuracy for Beidou system is 10 meter.

Parameter values of the aforementioned GNSS satellites are summarized in TABLE 2.1 and TABLE 2.2 [24, 23, 25, 31, 26, 27, 28].

At each GNSS satellite, the generation procedure of GNSS signal can be model as Fig. 2.4.

Based on Fig. 2.4, the general model transmitted signal per channel each satellite can be mathematically expressed as follows

$$s(n) = A \cdot C(n) \cdot D(n) \cdot \sin(2\pi f_c \cdot n) \tag{2.1}$$

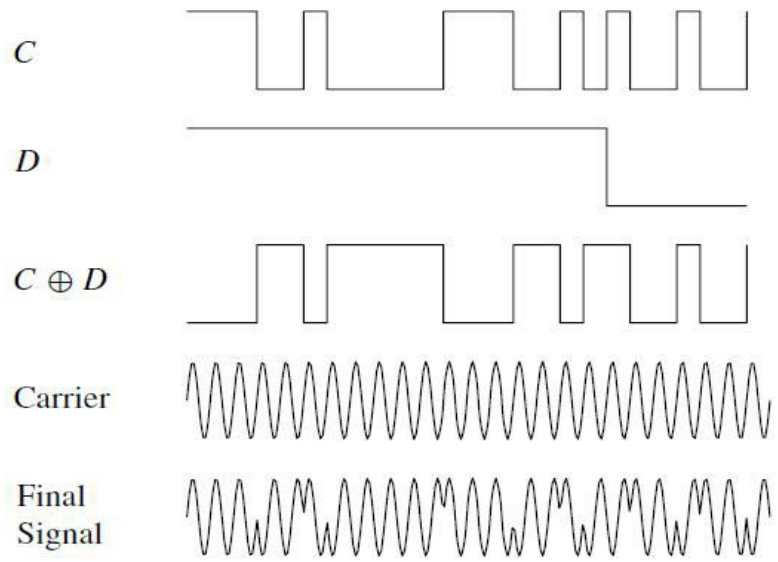


Fig. 2.4: The flow diagram of generating GNSS signal [24].

or

$$s(n) = A \cdot C(n) \cdot D(n) \cdot \cos(2\pi f_c \cdot n) \tag{2.2}$$

where $A$ represents transmitted magnitude, $C(\cdot)$ represents PRN code, $D(\cdot)$ represents navigation message, $f_c$ represents transmission frequency and $n$ represents the number of transmitted sample. Specifically, taking GPS as an example, the transmitted signal at each satellite can be expressed as [24, 76]

$$\begin{aligned} s_{\mathrm{g}}(n) = \; & \sqrt{2P_{\mathrm{C/A}}} \cdot \mathrm{C/A}(n) \cdot D(n) \cdot \cos(2\pi f_{L1} \cdot n) \\ & + \sqrt{2P_{\mathrm{PL1}}} \cdot \mathrm{P}(n) \cdot D(n) \cdot \sin(2\pi f_{L1} n) \\ & + \sqrt{2P_{\mathrm{PL2}}} \cdot \mathrm{P}(n) \cdot D(n) \cdot \sin(2\pi f_{L2} \cdot n) \end{aligned} \tag{2.3}$$

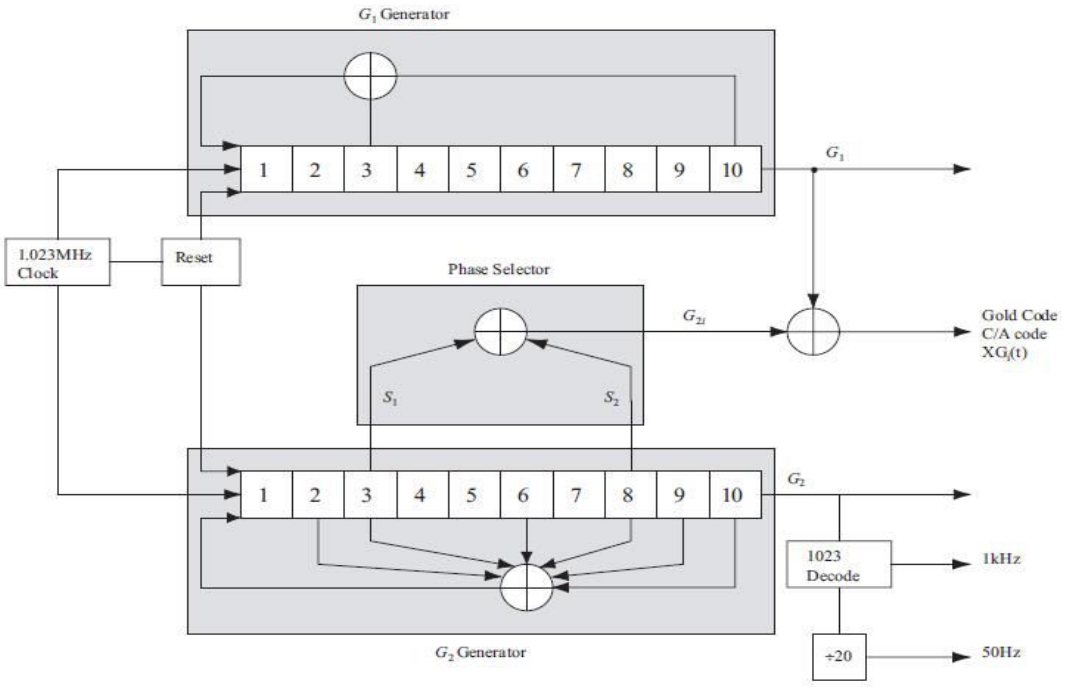


Fig. 2.5: The flow diagram of gold code generation [24].

where C/A represents C/A code, $P(\cdot)$ represents P code, $f_{L1}$ represents L1 frequency band, $f_{L2}$ represents L2 frequency band, $P_{\mathrm{C/A}}$ and $P_{\mathrm{P}}$ represents power of C/A code signal and P code signal, respectively.

For PRN code in GNSS signals, using GPS C/A code signal as an instance, the code is generated based on Gold sequence [78, 79], which generation procedure [24, 77] is shown in Fig. 2.5

As it can be seen that gold code sequence is generated by two shift registers. The correlation properties of PRN code using GPS C/A code as an instance is shown in Fig. 2.6.

In Fig. 2.6, it can be seen that PRN code has approximated no cross correlation. Also PRN code has approximated no auto-correlation except for zero tag.

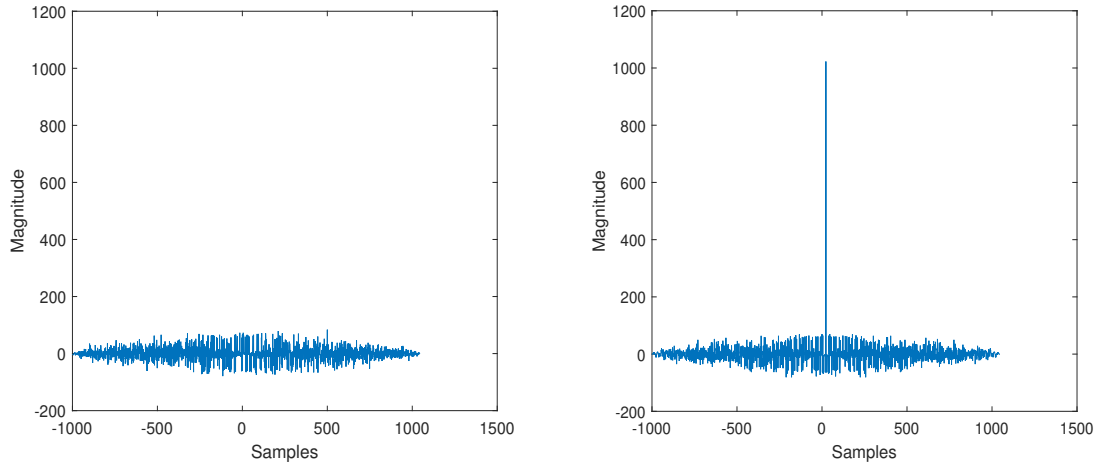


Fig. 2.6: The correlation property of GPS C/A code: (a) cross correlation, (b) auto-correlation.

Because of the no cross correlation property, in GPS, Galileo and Beidou systems, different PRN code sequence are used for distinguishing different satellites.

### 2.2.2 Passive SAR Receiver

For passive SAR such as GNSS-SAR, since the signals should be from other sources of opportunity, the receiver can only work in the mode bi-static SAR or multi-static SAR. However if the receiver locates at the same horizontal axis as the target, the system can be considered as quasi mono-static [23, 36], where the bi-static observation angle can be regard as zero.

At software defined passive GNSS-SAR receiver, direct and surveillance antennas are employed for receiving direct and reflected GNSS signals, respectively, where the movement of the surveillance antenna is performed for aperture synthe-

sis [23, 33, 54]. For achieving time synchronization, both direct and surveillance channels are connected to the GNSS receiver with the same clock for receiving signals. The received direct and reflected GNSS signals are quadrature demodulated to base-band (normally demodulated to intermediate frequency (IF) at front end for the storage, and then further demodulated to base-band for post processing), digitally sampled and save into two domains i.e. range domain and azimuth domain [23, 31], respectively. Assume after digitizing, the received signals have $N_t$ samples in range time domain and $M_u$ samples in azimuth time domain, then the signal from direct channel can be expressed as

$$\begin{aligned} s_d(t,u) = \; & A_d(t,u)\, C[t-\tau(u)]\, D[t-\tau(u)] \\ & \times \exp\left(j\left(2\pi \cdot f_d(u)\, t + \phi_d(u)\right)\right) + n_d(t,u) \end{aligned} \tag{2.4}$$

where $A_d(\cdot)$ represents the received signal amplitude, $C(\cdot)$ represents GNSS signal PRN code; $D(\cdot)$ represents navigation message; $u$ denotes azimuth time domain, which length is limited by the duration for performing synthetic aperture; $t$ denotes range time domain, which length is constrained by PRN code period; $\tau(\cdot)$ denotes range delay per azimuth bin (azimuth coordinate), where each azimuth bin is identically the equivalent pulse repetition time that represented by one PRN code period; $f_d(\cdot)$, $\phi_d(\cdot)$ denotes Doppler rate and carrier phase; $n_d(\cdot)$ represents background noise of direct signal. The parameters $f_d(\cdot)$, $\phi_d(\cdot)$ can be considered as unchanged within the same azimuth position, and $D(\cdot)$ is considered as a constant within the same range domain.

The signal received at surveillance channel of reflecting point at the corresponding range coordinate (range position) $l$ per azimuth bin can be considered as a delayed version of that at direct channel (2.4), which can be expressed as

$$s_r(t,u) = \begin{cases} A_r^l(t,u)\, C\left[t-\tau(u)-\tau_R^l(u)\right] & \\ \quad \cdot D\left[t-\tau(u)-\tau_R^l(u)\right] & \\ \times \exp\left(j\left(2\pi \cdot f_d(u)\, t+\phi_r(u)\right)\right)+n_r(t,u) & \text{presence of reflected GNSS signals} \\ n_r(t,u) & \text{absence of reflected GNSS signals} \end{cases} \tag{2.5}$$

where $A_r^l(\cdot)$ denotes reflected magnitude, $\tau_R^l$ denotes delay of the scattering point at range position $l$, $\phi_r^l$ represent reflected carrier phase; $n_r(\cdot)$ represents the noise of reflected signal. The parameters $f_d$, $\phi_r$ can be considered as unchanged within the same azimuth position as well. The received reflected signal of the targeted area is an accumulation of each single reflection point with different signal strength $A_r^l$ and delayed values $\tau_R^l$ in both range and azimuth domains, which can be expressed as

$$s_R(t,u) = \sum\sum s_r(t,u)\,. \tag{2.6}$$

The length of an azimuth bin equals to one PRN code period; Received Doppler frequency of direct and reflected GNSS signals can be regarded as approximately the same for non moving objects.

Before performing imaging, direct signal synchronization [39] based acquisition and tracking procedure is performed for constructing imaging matched filter [45].

During this stage, the local replica for matched filtering purpose is constructed at range domain for each azimuth bin based on the synchronized parameters $\tau(\cdot)$, $f_d(\cdot)$ and $\phi_d(\cdot)$. Since signal synchronization is a mature technique in GNSS-SAR and not the concentration in this thesis, the detailed description is omitted correspondingly. The synchronized local replica is formed into the same size as digitized direct signal as well. Denote the symbol $s_{m\_f}(\cdot)$ as the local replica for matched filtering purpose for GNSS-SAR imaging, the corresponding expression can be seen as follows

$$\begin{aligned} s_{m\_f}(t,u) &= A_d(t,u)\, C[t-\tau(u)]\, D[t-\tau(u)] \\ &\quad \times \exp\left(j\left(2\pi f_d(u)\, t + \phi_d(u)\right)\right). \end{aligned} \tag{2.7}$$

## 2.3 GNSS-SAR Imaging Processing

### 2.3.1 Imaging Procedure

Back projection approach is a widely used conventional method for SAR imaging [23, 37], where two separated compression i.e. range compression and azimuth compression are contained. Assume the digitized range domain is upper bounded by $N_t$ samples and azimuth domain is upper bounded by $M_u$ samples, the overall view of GNSS-SAR image formation procedure are introduced and analyzed as follows:

1). Forming azimuth cells based on the expected azimuth resolution. Theoretically in general, the azimuth signal samples received from the same reflecting

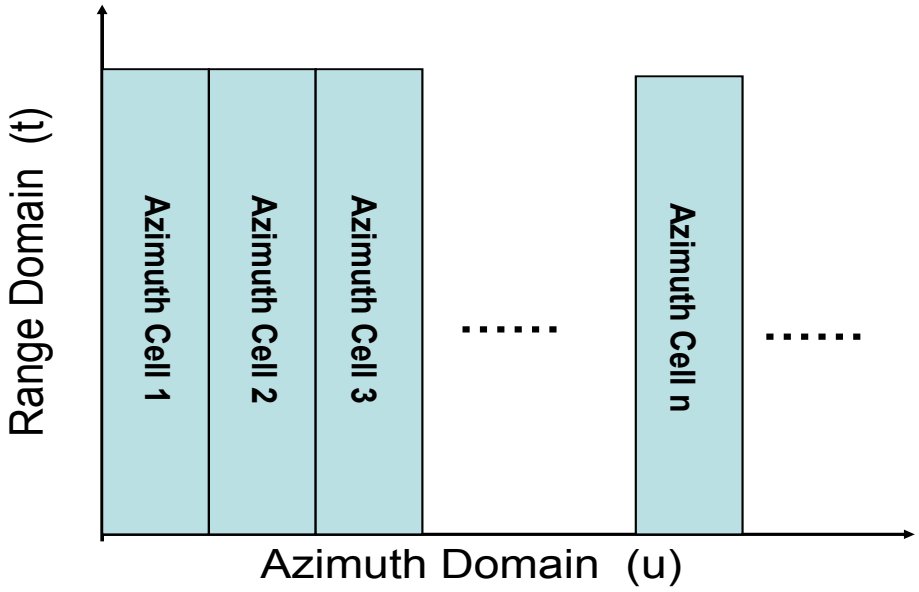


Fig. 2.7: The illustration of azimuth cell partition.

point are partitioned into the same cell. The illustration of the step can be seen in Fig. 2.7.

2). Range compression is performed by correlating reflected GNSS signal with direct GNSS signal at range domain, the result can be mathematically expressed as

$$T^r\left(N_s-1,u\right)=\frac{1}{N_s}\sum_{k=-\frac{N_s}{2}}^{\frac{N_s}{2}}s_r\left(t,u\right)s_{m\_f}^*\left(t-k,u\right) \tag{2.8}$$

where $*$ represents conjugate, $k$ denotes the each range sample (represents each range position) for performing compression per azimuth bin, $N_s$ ($N_s \leq N_t$) denotes total range sample quantity selected for range compression and

$T^r(N_s-1,u)$ denotes range compressed signal per azimuth bin.

3). Range migration correction is performed, which can be referred in [23, 31, 33]. The details of range migration correction are not focused in this thesis, thus it is omitted. Denote $\Delta R(u)$ as real range history per azimuth bin, then the correction factor can be formed as $\exp\left(j\frac{2\pi}{\lambda}\Delta R(u)\right)$, where $\lambda$ represents the signal wavelength. The migration procedure at range time domain per azimuth bin is performed as follow

$$T^c(N_s-1,u) = T(N_s-1,u) \times \exp\left(j\frac{2\pi}{\lambda}\Delta R(u)\right). \tag{2.9}$$

4). Azimuth compression within each resolution cell is performed by sliding correlating the azimuth signal with the azimuth matched filter segment in the current azimuth cell per range bin. The azimuth signal is identically range compressed signal samples along the moving trace of receiver, and azimuth matched filter segment is the template of azimuth signal in the current azimuth cell. The range bin is defined as the unit of range position within a PRN code period. Denote $i$ as the number of partitioned azimuth resolution cells, $T^c_{m_i}(\cdot)$ as the matched filter signal in the current azimuth cell, $k_2$ as the number of azimuth samples for compression and $M_s$ ($1 < M_s < M_u$) as the total azimuth sample quantity within the single azimuth cell. The azimuth compressed result matrix in the current resolution cell, denoted as $I^i_{(N_s-1)\times(M_s-1)}$, can then be expressed as follows

$$I^{i}_{(N_s-1)\times(M_s-1)} = \frac{1}{M_s} \sum_{k_2=-\frac{M_s}{2}}^{\frac{M_s}{2}} T^{c}_{m_i}\left(N_s-1,u\right)\left(T^{c}\left(N_s-1,u-k_2\right)\right)^{*}. \quad (2.10)$$

5). The total number of partitioned azimuth resolution cell during aperture synthesizing can be derived as $M_u - M_s$. The final GNSS-SAR image, denoted as $I^m$, is generated based on merging azimuth compressed result each azimuth cell and getting the absolute value, which can be seen as follows

$$I^{m} = \left| \begin{pmatrix} I^{1}_{(N_s-1)\times(M_s-1)} \\ I^{2}_{(N_s-1)\times(M_s-1)} \\ \cdot \\ \cdot \\ \cdot \\ I^{i}_{(N_s-1)\times(M_s-1)} \\ \cdot \\ \cdot \\ \cdot \\ I^{M_u-M_s-1}_{(N_s-1)\times(M_s-1)} \\ I^{M_u-M_s}_{(N_s-1)\times(M_s-1)} \end{pmatrix} \right| \quad (2.11)$$

where $|\cdot|$ denotes the symbol of absolute value. For obtaining final GNSS-SAR image $I^m$, there exists the numbers of operations $M_u - M_s$ during merging.

Taking GNSS-SAR receiver based on GPS C/A code signal as an example, the unit of $M_s$ and $M_u$ are mini-second. For straight moving receiver, if the receiver moving speed is $V_t$, the length azimuth resolution cell along the moving trace can be expressed as $V_t \cdot M_s \times 10^{-3}$ m, and the length for performing aperture synthetic along the moving trace can be expressed as $V_t \cdot M_u \times 10^{-3}$ m; for angular moving receiver, if the receiver angular speed is $\omega_t$ rad/s, then at the range distance $r$ m, the length of azimuth resolution cell along the moving trace can be expressed as $\omega_t \cdot r \cdot M_s \times 10^{-3}$ m, and the length for performing aperture synthetic along the moving trace can be expressed as $\omega_t \cdot r \cdot M_u \times 10^{-3}$ m.

### 2.3.2 Performance Analyses

**Signal Detectability for Object Identification:**

In each azimuth cell, the reflected signal strength comes from the same range delay with the same material is considered as the same. Within an azimuth cell, denoting the received reflected signal mean value at GNSS receiver radio frequency (RF) front end per range delay as $A_s^k$, the mean value of matched filter signal (2.7) is $A_s$ and noise energy at GNSS receiver RF front end as $\sigma^2$, then after performing (2.9), the compressed signal mean value per range delay in each range domain can be derived as $A_s A_s^k$, and the noise energy per range position can be derived as $A_s^2 \cdot \sigma^2$. After performing azimuth compression within the $M_s$ samples duration, The compressed signal mean per range delay in each azimuth cell can be derived as $A_s^2 \left(A_s^k\right)^2$, and the noise energy per range position in each azimuth cell can be

derived as $\frac{1}{M_s}A_s^4 \cdot \sigma^4$. In the absence of a reflected signal, the static distribution of (2.9) and (2.10) are zero mean with the same variance of the presence of the reflected signal according to the derivation. For study the object detectability for each azimuth cell, the following binary hypothesis [103] problem can be formed as

$$I^i_{(N_s-1)\times(M_s-1)} \underset{H_0}{\overset{H_1}{\gtrless}} \epsilon \tag{2.12}$$

where $\epsilon$ represents signal detection threshold, $H_1$ represents presence of compressed signals and $H_0$ represents absence of compressed signals. Because the samples for performing compression are sufficiently large, according to central limit theory [104], the static distribution of (2.10) can be considered as a Gaussian process. Therefore, the false alarm probability per range position with respect to the hypothesis (2.12) can be expressed as

$$P_f = Q\left(\frac{\epsilon}{A_s^2\sigma^2} \times \sqrt{M_s}\right) \tag{2.13}$$

and detected probability per range position with respect to the hypothesis (2.12) can be derived as

$$P_d = Q\left(\frac{\epsilon - A_s^2\left(A_s^k\right)^2}{A_s^2\sigma^2} \times \sqrt{M_s}\right) \tag{2.14}$$

where $Q(\cdot)$ represents the cumulative probability density function of the Gaussian process. If the threshold of $P_f$ is determined at the level $P_f^\circ$, the receiver operating curve (ROC) [104] expression of $P_d$ with respect to $P_f^\circ$ is derived as

$$P_d = Q\left(Q^{-1}\left(P_f^\circ\right) - \frac{\left(A_s^k\right)^2}{\sigma^2} \times \sqrt{M_s}\right). \tag{2.15}$$

(2.15) represents the detectability of the conventional GNSS-SAR imaging algorithm for each scattering point, where the term $\sqrt{M_s}$ represents the gain of signal strength after performing imaging, the term $\left(A_s^k\right)^2$ represents the reflected signal strength per range delay at GNSS receiver RF front end and the term $\frac{\left(A_s^k\right)^2}{\sigma^2}$ represents the respected signal-to-noise ratio (SNR). The noise power $\sigma^2$ at GNSS receiver RF front end can be expressed as $\sigma^2 = kBTF$, where $k$ represents the Boltzmann constant $1.38 \times 10^{-23}$, $B$ represents signal bandwidth, $T$ represents environment temperature, $F$ represents noise factor and $F = 1 + \frac{T}{290\text{K}}$ [23]. Using as an example the GPS C/A code receiver developed by ip-solutions (http://www.ip-solutions.jp) and the environmental temperature $T = 300$K, we can have $B = 1.023 \times 10^6$Hz, $F \approx 2.03$. Thus it can be derived that the noise power $\sigma^2$ is approximated $-130$ dBm. The total gain before imaging, which includes antenna gain and RF gain, is approximately 20dB. Taking reflected signal value $-160$dBm, the typical weak signal case at earth surface [102] for the study, then we can have $\left(A_s^k\right)^2 = -140$ dBm. Assume $P_f^\circ$ is constrained no larger than 0.1 and $M_s = 60000$ azimuth samples, which corresponds to 1 min, substituting all the relevant values into (2.15), we can have that $P_d \approx 0.18$, which represents an unfavorable image quality. Furthermore based on (2.15), if we increase $M_s$ value, which means to increase azimuth coherent correlation length, the value $P_d$ will increase as well, however at the meantime, the numbers of computations are increased.

**Range Resolution:**

In this thesis, range resolution is analyzed based on the ambiguity of the compressed pulse. A more detailed expression of range compressed signal with respect to the noise absence term each scattered point in a range time domain can be expressed as

$$\begin{aligned} & s_r \circledast s^*_{m\_f} \\ & \quad = A_r^l \cdot \Lambda\left(t - \tau\left(u\right) - \tau_R^l\left(u\right)\right) \times \exp\left(j\left(\phi_r\left(u\right) - \phi_d\left(u\right)\right)\right) \end{aligned} \tag{2.16}$$

where $\Lambda\left(\cdot\right)$ indicates triangle function and its duration is determined by the PRN code chip rate of the GNSS signal. In (2.16), because the Doppler frequencies of $s_r$ and $s_{m\_f}$ respectively are similar, the frequency component after performing range correlation for the compression can be approximated as zero. Assuming the chip rate of PRN code $C\left(\cdot\right)$ is $B$, then the frequency value of the triangle function $\Lambda\left(\cdot\right)$ is $B$. Thus the main lobe of pulse duration of the triangle function $\Lambda\left(\cdot\right)$ can be derived as $0.586 \cdot \frac{1}{B}$, where 0.586 represents shape factor of waveform [23]. Because the terms $A_r^l$ and $\exp\left(j\left(\phi_r\left(u\right) - \phi_d\left(u\right)\right)\right)$ are constants with respect to range compressed delay $\tau_R^l$, the duration of (2.16) is only determined by the term $\Lambda\left(\cdot\right)$. Thus, the attainable range resolution with respect to pulse $\Lambda\left(\cdot\right)$ duration can be expressed as [23, 31, 56, 54, 55]

$$\delta_{R_1} = 0.586 \cdot \frac{c}{\cos\left(\beta/2\right) \cdot B} \tag{2.17}$$

where $c$ denotes the speed of light, $\beta$ represents bi-static angle, $\delta_{R_1}$ represents the achievable range resolution by the conventional algorithm and the value 0.586 represents the shape factor of a waveform. According to (2.17), it can be seen that for the conventional range compression algorithm in the GNSS-SAR, if bi-static angle is given prior, the range resolution is limited by signal code chip rate, and the best range resolution can be achieved at the level $0.586 \cdot \frac{c}{B}$ when $\beta = 0$. For instance, for GPS C/A code signal receiver, the value $B = 1.023$ MHz, thus the best range resolution can only be obtained at the level 171 m.

## 2.4 Summary

In this chapter, initially, the concept GNSS-SAR is introduced. The signal model of GNSS-SAR transmitter and receiver is given. Thereafter, the steps of conventional imaging algorithm are analyzed. The respective drawbacks are pointed out through the analyses.

# Chapter 3

# Imaging Enhancement under Weak Reflected Signals

## 3.1 Introduction

In this chapter, the compressed signal strength and the respective detectability are used to quantify the imaging quality. A new imaging algorithm is proposed. The main idea of the proposed imaging algorithm is to use joint coherent and non-coherent integration for azimuth compression processing in each azimuth cell to further improve signal detectability than single coherent or non-coherent integration. In the proposed algorithm, each pre-determined azimuth resolution cell is further divided into multiple non overlapped mini slots. Within each mini-slot, before azimuth compression, an addition scheme based on azimuthally distributed range compressed signal with migration correction is performed for both enhanc-

ing imaging signal detectability and reducing computational burden. Theoretical analysis and experimental results both indicate that the proposed algorithm can provide a greater imaging gain in signal strength and the respective detectability. At the same time, the proposed algorithm is obviously more time efficient than the conventional GNSS-SAR imaging algorithm. Specifically, using GPS C/A code receiver platform, the experiments show that the proposed algorithm can still detect the signal with the strength $-160$ dBm, while the conventional algorithm cannot. Also, the proposed algorithm increases computational speed 6 times higher than conventional imaging algorithm [60, 64].

The rest of this chapter is organized as follows. The proposed GNSS-SAR imaging algorithm under weak reflected signals is introduced in section 3.2. The main properties of the new imaging algorithm, compared to conventional GNSS-SAR imaging algorithm, is derived in the same section as well. Experimental study is carried out in section 3.3 to verify the proposed algorithm. Final concluding remarks are shown in section 3.4.

## 3.2 Signal Detectability of The Proposed Imaging Algorithm

In this chapter, a novel enhanced GNSS-SAR imaging algorithm is proposed for improvement of image quality of weak reflected signals. Different from the conventional imaging algorithm, in the proposed algorithm, a joint coherent and

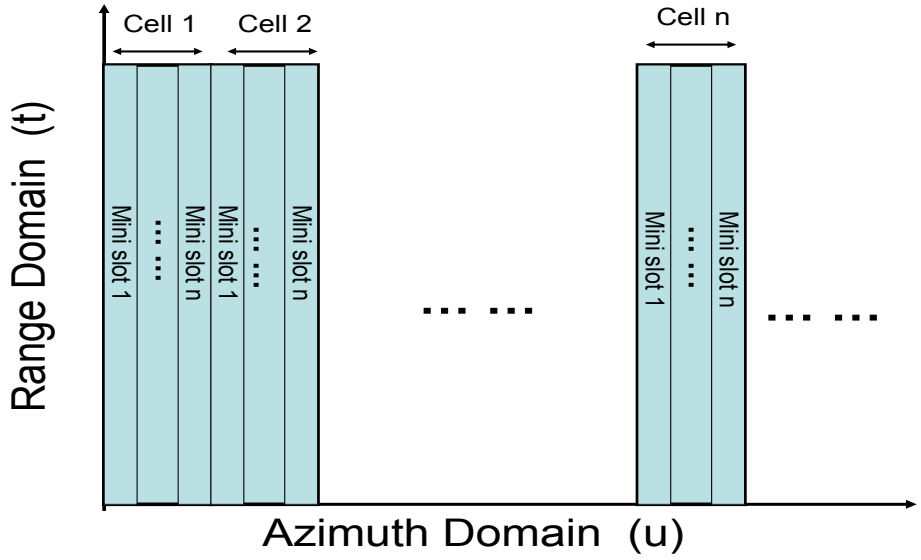


Fig. 3.1: Multiple mini-slot with $m_s$ samples duration division.

non-coherent scheme is used for azimuth compression each azimuth cell to further improve signal detectability. Working towards the main idea, the essential steps are summarized as follows.

- Further partition each azimuth cell into consecutive mini-slots as shown in Fig. 3.1.
- Adding together range compressed signals distributed in each mini-slot.
- Azimuth correlation for compression in each azimuth cell is based on the azimuth signal template after performing the addition scheme in each mini-slot.

After performing the step in the second bullet, since the signal samples for azimuth correlation processing is reduced, the numbers of computation is reduced.

This indicates a higher computational speed can be achieved. The detailed steps of the proposed algorithm are introduced and analyzed as follows.

Before imaging, azimuth resolution cells are firstly partitioned with $M_s$ samples duration as Fig. 2.7. However different from the conventional algorithm, each partitioned azimuth cell in Fig. 2.7 is then further divided into multiple non overlapped consecutive mini-slots. The signals received from approximated the same azimuth position, assumed to be bounded by $m_s$ $(1 < m_s < M_s)$ azimuth samples duration, are contained under the same mini-slot. Therefore the length of each mini-slot is $m_s$ azimuth samples. The adjacent code periods can be added into the same azimuth position is because the respective receiver displacement is very small, compared to the length of an azimuth cell. For instance, if the azimuth cell is partitioned at the level 1 m, the displacement of SAR receiver within centimetres level is not significant, which can be regarded as the same azimuth position.

Range compression and range migration correction are then performed in the same manner as the conventional GNSS-SAR imaging algorithm, and the range compressed signal of the proposed algorithm is the same as (2.9).

An addition scheme within each mini-slot of $m_s$ samples duration is applied on the azimuthally distributed range compressed signal (2.9). The signal after the accumulation per mini-slot can be expressed as follows

$$T^{r_p}\left(N_s - 1, \lfloor u/m_s \rfloor\right) = \frac{1}{m_s} \sum_{l_1=0}^{m_s-1} \left(T^c\left(N_s - 1, \lfloor u/l_1 \rfloor\right)\right) \tag{3.1}$$

where $l_1$ represents the sample in the $m_s$ mini slot, $\lfloor \cdot \rfloor$ represents the floor function and $T^{r_p}\left(N_s-1, \lfloor u/m_s \rfloor\right)$ represents the signal on the basis of accumulating range compressed energy in the proposed algorithm. Within an azimuth cell, if a reflected GNSS signal is present, the mean of (3.1) per range delay can be derived as $A_s A_s^k$, and the corresponding noise power can be derived as $\frac{1}{m_s} A_s^2 \cdot \sigma^2$. When absence of signal, the static mean of (3.1) will be zero with the same noise power.

Because multiple mini-slots within the resolution cell are partitioned, the samples quantity for completing the azimuth compression is converted into $M_s/m_s$. And azimuth matched filter is generated based on the azimuthal template of (3.1) per azimuth cell. Denote $i_2$ as the number of azimuth cell in this section and $T_{m_{i_2}}^{r_p}(\cdot)$ as azimuth matched filter signal in the current azimuth cell, then after performing azimuth compression for each azimuth cell, the compressed result can be expressed as

$$\begin{aligned} & T_{i_2}^{a_p}\left((N_s-1) \times (\lfloor M_s/m_s \rfloor - 1)\right) \\ & \quad = \tfrac{1}{\lfloor M_s/m_s \rfloor} \textstyle\sum_{l_2=-\lfloor M_s/m_s \rfloor/2}^{\lfloor M_s/m_s \rfloor/2} T_{m_{i_2}}^{r_p}\left(N_s-1, \lfloor u/m_s \rfloor\right) \\ & \qquad\qquad \times \left(T^{r_p}\left(N_s-1, \lfloor u/m_s \rfloor - l_2\right)\right)^* \end{aligned} \tag{3.2}$$

where $l_2$ represents the sample in the azimuth resolution cell for performing compression of the transformed sample quantity $M_s/m_s$, and $l_2 = \lfloor u/m_s \rfloor$; $T_{i_2}^{a_p}(\cdot)$ represents the azimuth compressed signal matrix per azimuth cell of the proposed algorithm. When a reflected GNSS signal is present, the static signal mean of (3.2) per range delay in an azimuth cell can be derived as $A_s^2\left(A_s^k\right)^2$ and the cor-

responding noise power can be derived as $\frac{1}{M_s/m_s}\left(\frac{1}{m_s}A_s^2\cdot\sigma^2\right)^2$. When absence of signal, the static mean of (3.2) will be zero as well.

To obtain the final GNSS-SAR image, the compressed signal each azimuth cell is merged in the same manner as in (2.11). However, the numbers of operations performed during addition process changes into $\frac{M_u-M_s}{m_s}$.

In total, the overall view of the proposed algorithm are shown in Algorithm 3.1.

**Algorithm 3.1** Steps of the proposed GNSS-SAR imaging algorithm of weak reflected signals

1: Partitioning azimuth resolution cell with the length $M_s$ samples duration.
2: Within each azimuth resolution cell, partitioning $M_s$ into non overlapped multiple mini-slots. Each mini slot has the length $m_s$ ($m_s < M_s$) azimuth samples.
3: Performing range compression by using $N_s$ range samples as (2.8) per azimuth bin.
4: Range migration correction based on (2.9).
5: Accumulating the azimuthally distributed range compressed signal (2.9) within each $m_s$ mini slot by the $\frac{1}{m_s}\sum_{l_1=0}^{m_s-1}(\cdot)$ adder per azimuth cell as (3.1).
6: The azimuth samples quantity per azimuth resolution cell is transformed into $M_s/m_s$ after performing Step 5.
7: Azimuth compression per azimuth cell with the $M_s/m_s$ samples as (3.2).
8: Merging the azimuth compressed signals per azimuth resolution cell.
9: Outputting final GNSS-SAR image.

In terms of object detectability for each azimuth position of the proposed algorithm, similarly the binary hypothesis problem is also formulated as

$$T^{a_p}\left((N_s-1)\times(\lfloor M_s/m_s\rfloor-1)\right)\underset{H_0}{\overset{H_1}{\gtrless}}\epsilon_p \tag{3.3}$$

where $\epsilon_p$ represents the signal detection threshold per azimuth cell of the proposed algorithm. Still based on central limit theory, the false alarm probability of the

hypothesis (3.3) can be derived as

$$P_{f_p} = Q\left(\frac{\epsilon_p}{A_s^2 \cdot \sigma^2} \times \sqrt{M_s \cdot m_s}\right) \tag{3.4}$$

detected probability of the hypothesis (3.3) can be derived as

$$P_{d_p} = Q\left(\frac{\epsilon_p - A_s^2 \cdot \left(A_s^k\right)^2}{A_s^2 \cdot \sigma^2} \times \sqrt{M_s \cdot m_s}\right). \tag{3.5}$$

Assuming that $P_{f_p}$ is also constrained at the level $P_f^\circ$, the ROC expression of the detected probability $P_{d_p}$ with respect to $P_f^\circ$ can be expressed as follows

$$P_{d_p} = Q\left(Q^{-1}\left(P_f^\circ\right) - \frac{\left(A_s^k\right)^2}{\sigma^2} \times \sqrt{M_s \cdot m_s}\right). \tag{3.6}$$

(3.6) represents the detectability of the proposed algorithm, in which, the term $\sqrt{M_s \cdot m_s}$ represents gain in signal strength. Compared with the conventional imaging algorithm, it can be seen that the proposed algorithm can give an enhanced gain in signal at the level $\sqrt{m_s}$. And because $m_s > 1$, the value in (3.6) is larger than that of (2.15). Assume that $m_s$ is determined as 100 azimuth samples duration (obtained by trials and error test and smaller than the $M_s$ value), again using as an example the GPS C/A code signal receiver developed by ip-solutions with the aforementioned parameter values in section 2.3 of chapter 2, when the corresponding values are substituted into (3.6), the detected probability $P_{d_p}$ can be achieved at a level no less than 0.9. The proposed algorithm can thus pro-

vide significantly greater detectability than the conventional GNSS-SAR imaging algorithm under weak reflected signals.

Next, we compare the computational complexity of the proposed imaging algorithm with conventional imaging algorithm. For conventional GNSS-SAR imaging algorithm, there has $(N_s)^2 \times M_u$ times of computations throughout range compression state, $M_s \times M_u \times N_s$ times of computation throughout azimuth compression state per azimuth resolution cell and $M_u - M_s$ times of computation when merging the compressed results each azimuth cell. Therefore the overall complexity during imaging procedure is derived as

$$\mathcal{O}\left(N_s \times M_u \times \left(N_s + \left(M_u - M_s\right) \times M_s\right)\right). \tag{3.7}$$

For the proposed algorithm, there has $\left(\left(N_s\right)^2 + N_s\right) \times M_u$ times of computation throughout range signal correlation processing, $\frac{1}{m_s^2} \times M_s \times M_u \times N_s$ times of computation in obtaining the compressed result per azimuth resolution cell and $\left(M_u - M_s\right)/m_s$ times of computation when merging the compressed result each azimuth cell. Thus the overall complexity during imaging procedure is derived as

$$\mathcal{O}\left(N_s \times M_u \times \left(N_s + 1 + \frac{1}{m_s^3} \times \left(M_u - M_s\right) \times M_s\right)\right). \tag{3.8}$$

Comparing (3.8) with (3.7), it can be that the computation complexity for (3.8) is deducted by the level

$$\mathcal{O}\left(N_s \times M_u \times \left(\left(1-\frac{1}{m_s^3}\right) \times (M_u - M_s) \times M_s - 1\right)\right). \tag{3.9}$$

The properties of the proposed algorithm are summarized as follows.

**Property 3.1**: The proposed algorithm can provide a higher gain in signal strength after performing image formation so that the image detectability increased significantly.

**Property 3.2**: The proposed GNSS-SAR imaging algorithm has a significantly lower computational complexity than the conventional GNSS-SAR imaging algorithm.

## 3.3 Experimental Evaluation

Experiments were carried out to evaluate the performance of the proposed imaging algorithm. A dual channel GPS C/A code software defined receiver was used for the experiment to record direct and reflected GNSS signals respectively as an example. The receiver is ground-based model. The parameter values at receiver end for the experiment are given in TABLE 3.1.

Based on TABLE 3.1 and the aforementioned exampled $M_s$ and $m_s$ values (which obtained by trials and errors tests) in section 2.3 in chapter 2 and section 3.2 in this chapter for imaging processing, at first, we can have that the theoretical

TABLE 3.1: Field experimental parameter values

| Parameters | Types or Values |
|---|---|
| Utilized signal | GPS C/A code signal |
| Operating frequency | 1575.42 MHz (L1 band) |
| Transmission power | 50 w |
| Code period | 1 ms |
| Signal bandwidth $B$ | 1.023 MHz |
| Duration for synthetic aperture formation | 2 min |
| Sampling frequency | $1.6369 \times 10^7$Hz |
| Total number of range samples in each code period $N_t$ | 16369 samples |
| Number of range samples $N_s$ for performing range compression | 12800 samples |
| Total number of samples in azimuth domain each range bin $M_u$ | 120000 samples |
| Antenna gain + RF gain | 20 dB |
| Boltzmann constant $k$ | $1.38 \times 10^{-23}$ |
| Experimental temperature | 300K |
| Distance between satellite and earth surface | $22,200$ km |

noise factor $F = 1 + \frac{T}{290\text{K}} \approx 2.03$ and the noise power for the implemented GNSS RF end is $\sigma^2 = kBTF \approx -130$ dBm. Then a simulation of ROC expression with regard to detection probability of both conventional and the proposed imaging algorithm is carried out. The typical GNSS signal strengths $-130$ dBm, $-140$ dBm, $-160$ dBm and $-165$ dBm are considered, respectively, where $-160$ dBm represents the typical weak GNSS signal case that received by the receiver. The simulation results obtained by Monte Carlo method [61] are shown as in Fig. 3.2.

In Fig. 3.2, it can be seen that with the same level of reflected signal strength and false alarm threshold, the proposed imaging algorithm outer performs the conventional one in detectability, particularly under the typical weak signal strength cases. With the same feasible detection probability larger than 0.9 and false alarm threshold 0.1, the proposed algorithm can cope a weaker signal case by the level around 10 dB weaker in general than that of the conventional imaging algorithm. This also indicates that the proposed algorithm can provide a higher imaging gain with regard to signal strength. Meanwhile, the numbers of computations of both conventional GNSS-SAR imaging algorithm and the proposed algorithm based on the parameter values are given accordingly in TABLE 3.2

Based on TABLE 3.2, it can be seen that the proposed algorithm has a significantly less computational complexity than the conventional algorithm, in which, the numbers of computations is deducted by the level $10^5$.

To further test the image quality can be potentially provided by the proposed

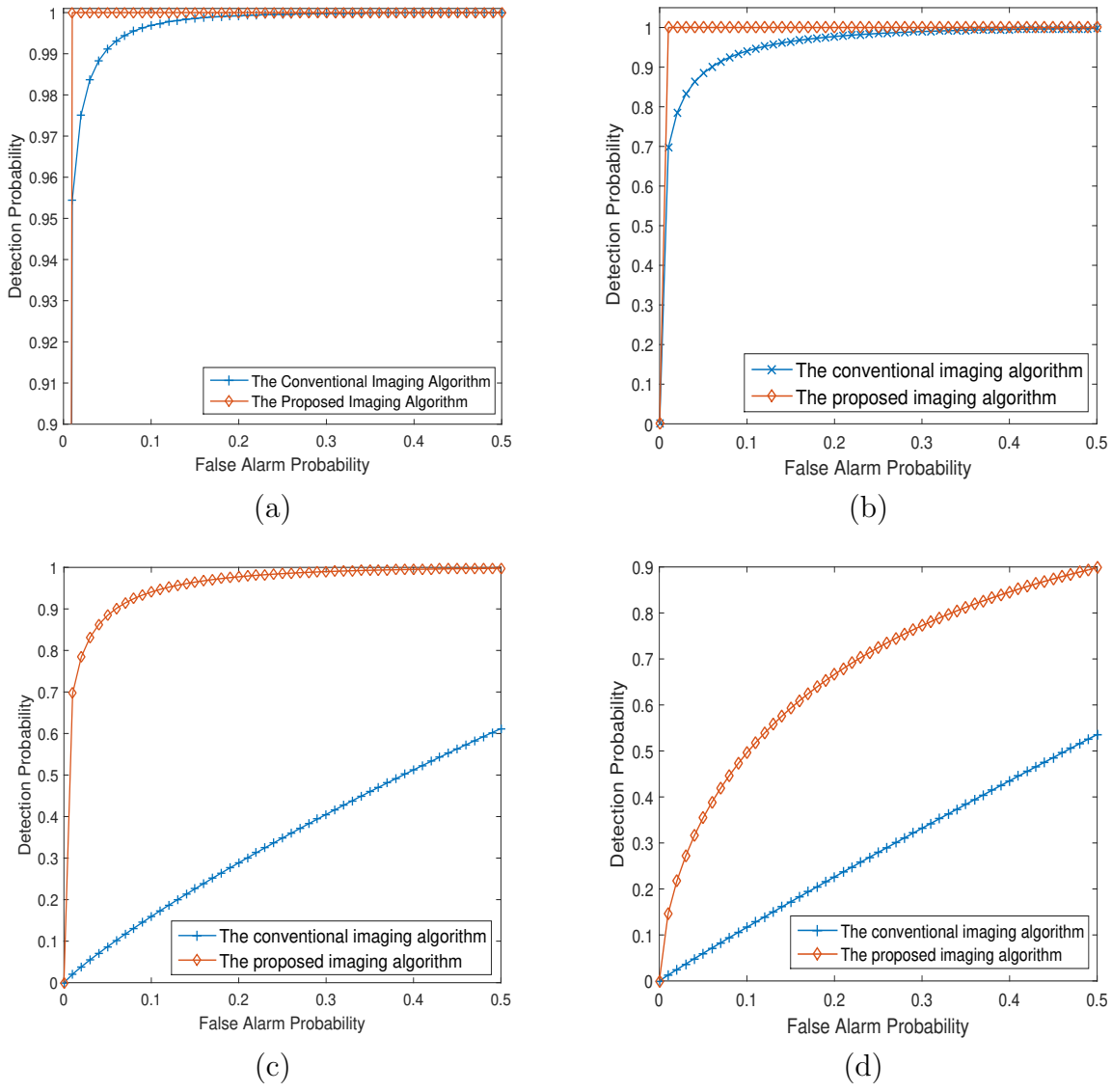


Fig. 3.2: (a) Detectability with respect to the reflected signal strength $-130$ dBm; (b) Detectability with respect to the reflected signal strength $-140$ dBm; (c) Detectability with respect to the reflected signal strength $-160$ dBm; (d) Detectability with respect to the reflected signal strength $-165$ dBm.

TABLE 3.2: Computational complexity based on the parameter values

| Algorithms | Numbers of computations |
|---|---|
| Conventional imaging algorithm | $\mathcal{O}\left(4.18 \times 10^{18}\right)$ |
| The proposed imaging algorithm | $\mathcal{O}\left(3.75 \times 10^{13}\right)$ |

algorithm, based on the parameter values listed in TABLE 3.1, two field case studies were carried out, respectively. The equipment for the field study are shown as Fig. 3.3.

In Fig. 3.3(e), direct and reflected GPS signals were collected through two separated antenna i.e. direct antenna and surveillance antenna, respectively, where the direct antenna is right hand circular polarization (RHCP) and faced to the sky; the surveillance antenna is left hand circular polarization (LHCP) and faced to the targeted glisten region. The appearance of direct and surveillance antennas and their respective models can be seen in Fig. 3.3(a) to (d), respectively. To achieve time synchronization, both signals from direct antenna and surveillance antenna are save by the same software defined GPS receiver radio frequency (RF) front end as shown in Fig. 3.3(f), simultaneously, in which, the signal saving processing is controlled by the specific software (see Fig. 3.3(g)) on laptop computer through a USB line. The RF front end is the model ET09/C developed and produced by ip-solutions (http://www.ip-solutions.jp). The direct signal synchronization and SAR imaging stages were carried out in post processing manner on MATLAB platform. The overall data flow diagram of the field experiment is summarized in Fig. 3.4.

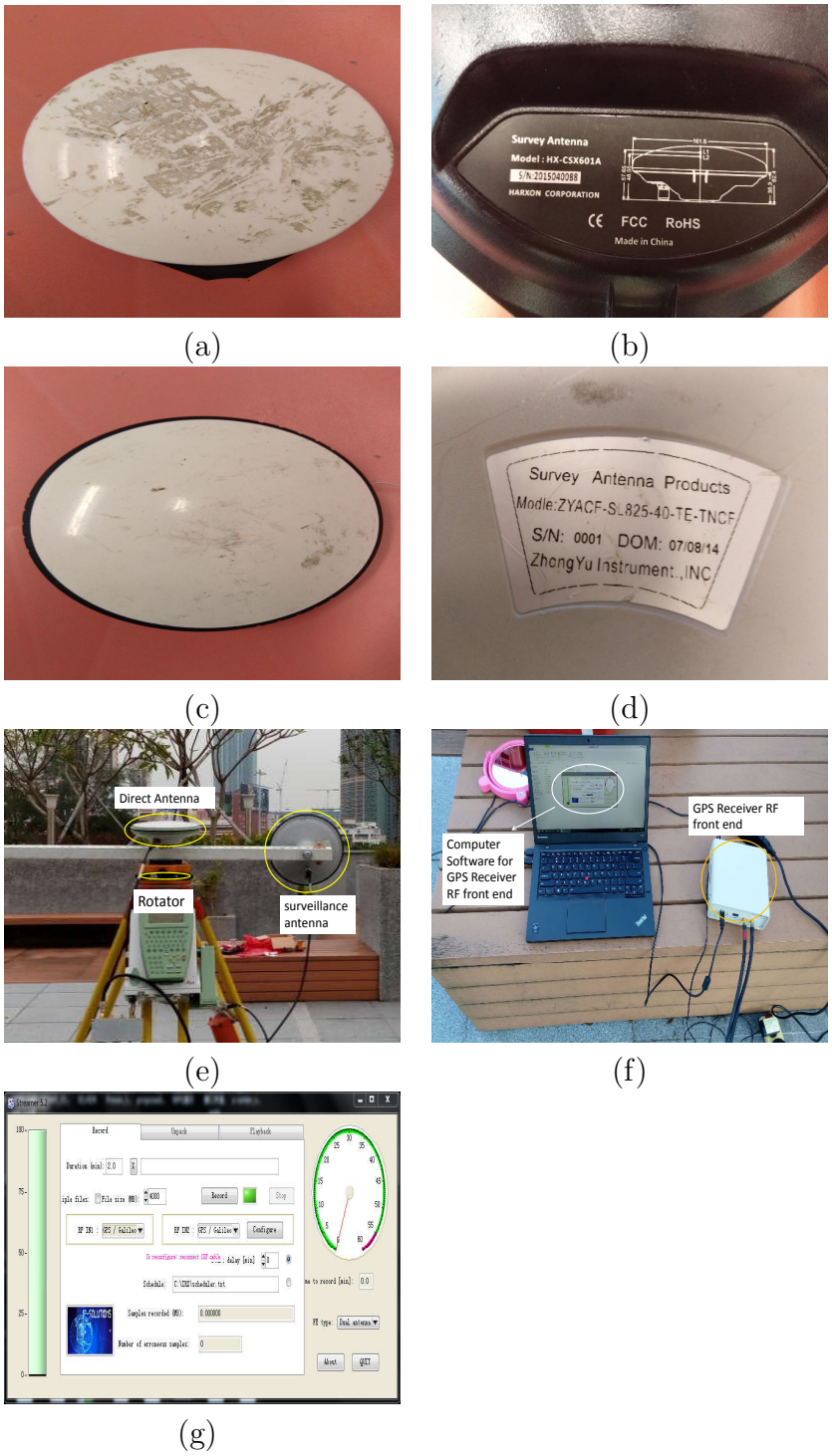


Fig. 3.3: GNSS-SAR equipment at receiver end: (a) Direct antenna; (b) The model of direct antenna; (c) Surveillance antenna; (d) The model of surveillance antenna; (e) The geometric position of direct and surveillance antenna; (f) The software defined GPS receiver front end; (g) The computer software for the receiver front end data collection.

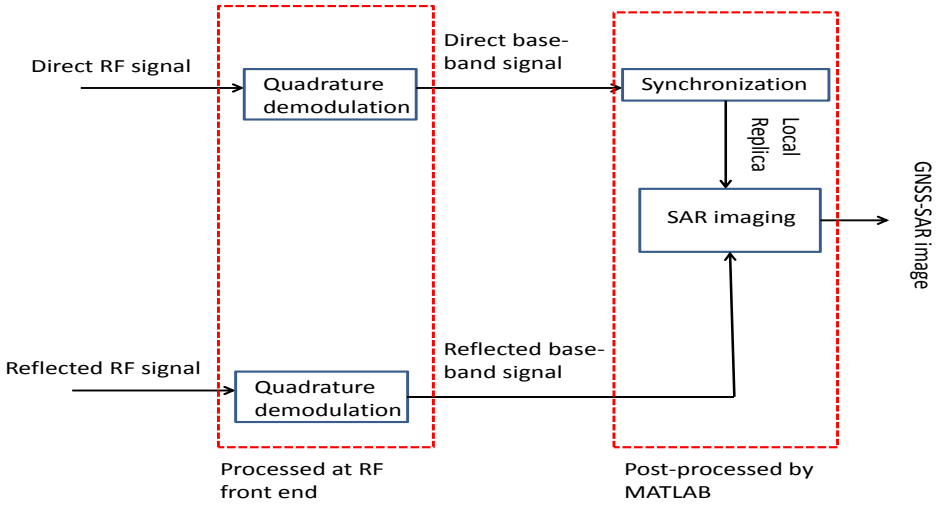


Fig. 3.4: Diagram of data flow of the field experiment.

### 3.3.1 Case Study 3.1

The current experiment is a closer range distance case, which aims to examine whether the proposed algorithm can provide a increased gain of signal strength on GNSS-SAR image when the theoretical detection probability is feasible for the both algorithms. The geometric positions of direct and surveillance antennas is the same as Fig. 3.3(a). The rotational movement of the rotator (see Fig. 3.3(a)) is used to provide an uniform circular movement of the surveillance antenna for forming synthetic aperture. The optical image for the experiment is shown in Fig. 3.5.

The targeted objects, two reflection broads and one terrace, are circled in Fig. 3.5, which are relatively strong scattering targets. From the left to the right, the azimuth distances between the first reflection broad and the terrace, and between

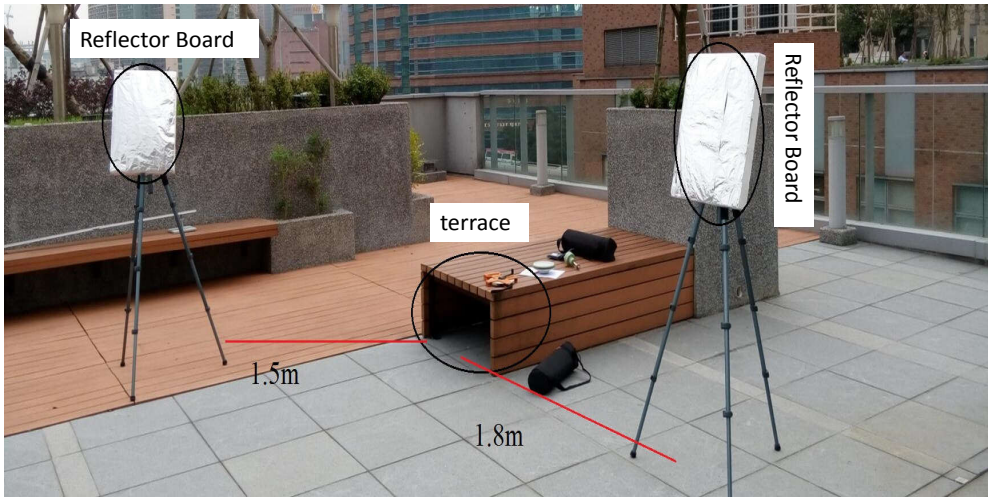


Fig. 3.5: Optical image for case study 3.1.

the terrace and the second reflection broad are 1.5 m and 1.8 m, respectively. The range distances between the three objects and the radar antenna are around 3 m. Aperture synthetic duration is 2 minutes and azimuth angular distance for radar antenna movement is around 120°. Based on the set up and TABLE 3.1, according to radar theory [101], it can be derived that the reflected signal strength at surveillance antenna is around $-130$ dBm. Combining the factors that noise power at RF front end is around $\sigma^2 = kBT\left(1 + \frac{T}{290\text{K}}\right) = -130$ dBm and RF gain is 20 dB, we can theoretically estimate that the received SNR for the current experiment is around 25 dB level.

In this experiment, based on radar back-scattering model [101], the satellite GPS PRN 27 is chosen as transmission of opportunity, as it is in the geometric position that direct signal interference can be maximally eliminated at surveillance antenna. The parameters $m_s$ and $M_s$ remain the same as the aforementioned values in section 2.3 in chapter 2 and section 3.2 in this chapter. Based on the set-

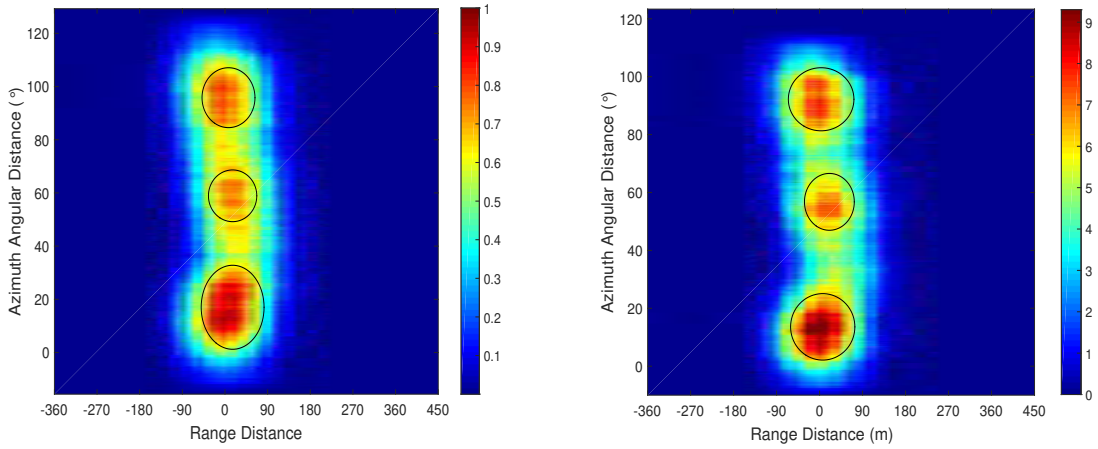


(a) (b)

Fig. 3.6: (a) GNSS-SAR image based on conventional GNSS-SAR imaging algorithm in case study 3.1, (b) GNSS-SAR image based on the proposed algorithm in case study 3.1 (color scale: pixel intensities sweep from the smallest value to the largest value)

up, according to Fig. 3.2(a), the detection probability for both the conventional and the proposed algorithms is feasible at the level higher than 0.95 for the case study, where the false alarm threshold is constrained by 0.1. The signal strength gain of the proposed algorithm is supposed to be around 10 dB higher than the conventional one in theoretical. The obtained GNSS-SAR images with respect to both conventional GNSS-SAR imaging algorithm and the proposed algorithm are shown in Fig. 3.6. For the ease of comparison, we normalized the image pixel intensity based on the conventional imaging algorithm, while the image pixel intensity based on the proposed imaging algorithm is zoomed out by the level of the same normalization factor as that of the conventional imaging algorithm.

In Fig. 3.6, due to the fact that the theoretical detection probability is feasible, the targets can be detected on both Fig. 3.6(a) and (b). The peak value in the

color bars of Fig. 3.6 represents the peak pixel intensity of the related images. According to the formula $\sigma = kBTF$, where $F = 1 + T/290\text{K}$, we can have that the noise power at RF end can be considered as constant under the same environmental temperature and signal bandwidth. Therefore the changes of peak pixel intensity in Fig. 3.6(b) is caused by the imaging signal strength gain. And because Fig. 3.6(b) is obtained on basis of zooming out by the normalization factor of Fig. 3.6(a), the peak pixel intensity in Fig. 3.6(b) exactly represents the enhanced signal strength the proposed imaging algorithm can provide, compared to the conventional one. Based on Fig. 3.6(b), it can be seen that indeed the proposed imaging algorithm can give a gain in signal strength at around 10 dB level higher than the conventional one under the considered experimental set-up. Decline in azimuth samples in Fig. 3.6(b) is because of the accumulation scheme within each $m_s$ mini slot of 100 azimuth samples. The range ambiguity of Fig. 3.6 is due to the correlation property of GPS C/A code. In summary, the results in Fig. 3.6 has demonstrated that with an expected theoretical detectability and fixed azimuth cell size, the proposed algorithm is obviously less strict in received reflected signal strength.

Based on the determined $N_s$, $m_s$, $M_s$, $N_t$ and $M_u$ values in this experiment, the computational complexity of conventional GNSS-SAR imaging algorithm and the proposed algorithm with respect to numbers of computations are studied as well, which result is similar as TABLE 3.2. Moreover, computational speed is studied. Both proposed and conventional algorithm were carried out on the same

TABLE 3.3: Algorithm Speed

| Algorithms | Speed |
|---|---|
| Conventional imaging algorithm | 20867.157 s |
| The proposed imaging algorithm | 3792.538 s |

computer platform, the speed values are extracted based on programme running time, which are shown in TABLE 3.3.

According to TABLE 3.3, the proposed algorithm is around 6 times faster than conventional algorithm.

### 3.3.2 Case Study 3.2

This experiment focus on a further sensing range case than the subsection 3.3.1, where the reflected signal at surveillance antenna will be weaker. The purpose of this experiment is to test whether the proposed algorithm can give a higher detectability with respect to a weaker signal strength. In this experiment, the geometric positions of direct and surveillance antennas are still the same as Fig. 3.3(a), in which, the same as the subsection 3.3.1, aperture synthetic was achieved by the circular trace of the surveillance antenna. Similarly, to maximally avoid the direct signal interference at radar channel, on the basis of geometric position and radar back-scattering model, the satellite GPS PRN 10 was chosen as transmission of opportunity. The targets are two building blocks shown in Fig. 3.7(a) which can be separated in both range and azimuth domains, are with a relatively far range of several hundreds meters far from GNSS-SAR receiver. The geometry


(a) (b)

Fig. 3.7: (a) The photo of targets at receiver's location; (b) The geometric locations of the targeted scenes and receiver based on Google map.

relationship of the targets and GNSS-SAR receiver is shown on Fig. 3.7(b).

Surface of Target 1 in this experiment is mainly covered by glass material; surface of Target 2 is mainly covered by concrete material. The cross-sectional area of Target 1 that faces to the GNSS-SAR receiver is around 300 to 400 $m^2$, while it is around 100 to 150 $m^2$ for Target 2. In Fig. 3.7, through the measurement on Google map, the distance between target 1 and GNSS-SAR receiver is around 168.44 m; the distance between target 2 to GNSS-SAR receiver is around 507.51 m. Thus range distance gap between target 1 and 2 is 339.07 m. The angular distance duration is upper bounded at 45° for the target 1 and lower bounded of 60° for the target 2. The azimuthal angular distance gap between the two targets is 15°. The aperture synthetic duration is 2 minutes with an angular distance length 90°, and an angular velocity $0.75°/s$. Based on the target to receiver

distances in this experiment, material reflectability and propagation degradation [101], theoretically the reflected signal strength at surveillance antenna from the Target 1 is approximated $-140$ dBm, and $-160$ dBm from the Target 2.

In this experiment, the parameter values $M_s$ and $m_s$ are kept the same as the subsection 3.3.1, and the rest of parameter values are the same as in TABLE 3.1 as well. Assume the false alarm is constrained by 0.1, then based on the set-up in this subsection, the theoretical detection probability for target 1 will be around 0.8 level under the conventional imaging algorithm, while it will be higher than 0.9 under the proposed imaging algorithm. For target 2, the theoretical detection probability will fall into around 0.2 for the conventional imaging algorithm, while it will be still around 0.9 for the proposed one. The obtained respective GNSS-SAR images are shown in Fig. 3.8, where the image obtained by the conventional imaging algorithm is normalized in pixel intensities, and the one obtained by the proposed imaging algorithm is zoomed out by the same level of the normalization factor as the conventional algorithm.

In Fig. 3.8(b), it can be seen that using the proposed imaging algorithm, the two block targets can be easily identified, as the theoretical detected probability of the proposed algorithm is more than 90% for the target 1 and around 90% for the target 2. Through measurement by using MATLAB software, it can be denoted that the range samples difference between the center of the two illuminated regions is 18 samples. Due to the fact at range distance domain of GPS software defined receiver, the distance value between two range samples is 18 m.

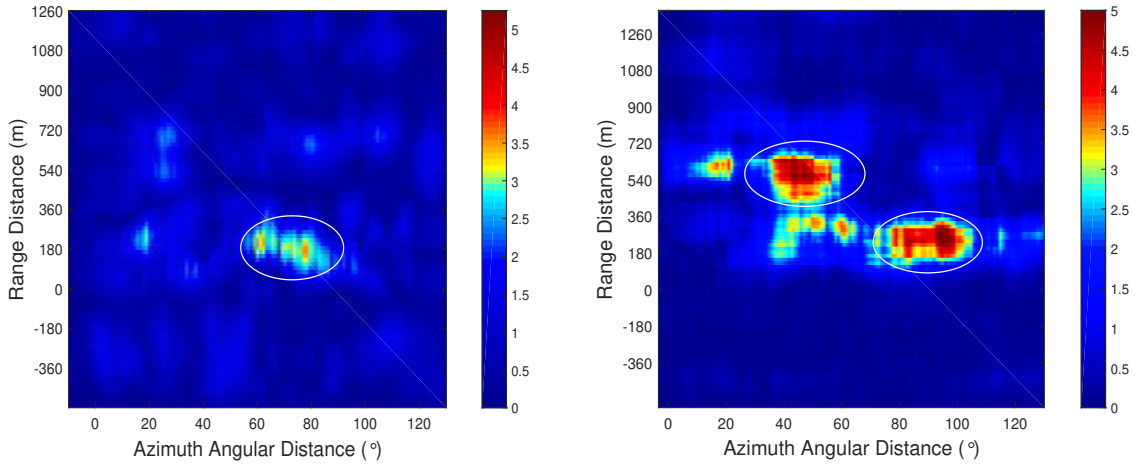


(a) (b)

Fig. 3.8: (a) GNSS-SAR image by the conventional imaging algorithm in case study 3.2; (b) GNSS-SAR image based on the proposed algorithm in case study 3.2 (color scale: pixel intensities sweep from the smallest value to the largest value)

Therefore 18 range samples difference corresponds to 18m $\times$ 18 = 324 m range distance value difference, which generally matched with the measured result on Google map 339.07 m. In terms of azimuth direction, the gap between the two illuminated scene is 247 samples. Due to the fact that the accumulation scheme by the factor $m_s = 100$ azimuth samples is adopted, the quantity of azimuth samples is declined. Thus 247 azimuth samples corresponds 19.76 s. This also corresponds to the azimuthal angular distance as $0.75°/\text{s} \times 19.76\text{s} = 14.82°$, which generally matches with the measurement value 15° on Google map. In total, the geometric position of detected targets on Fig. 3.8(b) can be matched with the field measured results in general. The illuminated region in yellow and light blue between the two illuminated regions in red on Fig. 3.8(b) is due to the scattering from the bridge

and trees between Target 1 and Target 2. However in Fig. 3.8(a), using conventional imaging algorithm, because noise is not sufficiently suppressed within the azimuth cell size 60000 samples, the corresponding obtained GNSS-SAR image is much noisier, particularly for target 2, compared to Fig. 3.8(b). Moreover, it is very hard to identify the target 2 on Fig. 3.8(a), as the corresponding detection probability is merely around 0.2 in theoretical. All in all, the results in Fig. 3.8 has verified that the proposed algorithm can provided a significantly enhanced detectability with regard to the typical weaker signal strength circumstance than the conventional GNSS-SAR imaging algorithm.

For computational complexity in this subsection, through investigations, the numbers of computation value during imaging is similar as TABLE 3.2 as well, while the computational speed is similar as TABLE 3.3.

Then we compare the performance between the proposed imaging algorithm and the approach that increasing azimuth matched filtering length. In this remit, based on conventional imaging algorithm, we increase the duration for synthetic aperture formation to 5 minutes, and the matched filtering length for each azimuth cell is increased to 4 minutes. The obtained GNSS-SAR image can be seen in Fig. 3.9(a), and the numbers of computational for generating Fig. 3.9(a), compared to the proposed algorithm can be seen in TABLE 3.4, and the algorithm running speed is shown in TABLE 3.5.

From Fig. 3.9, TABLE 3.4 and TABLE 3.5, we can see that although the objects are illuminated on the GNSS-SAR image, the number of computations

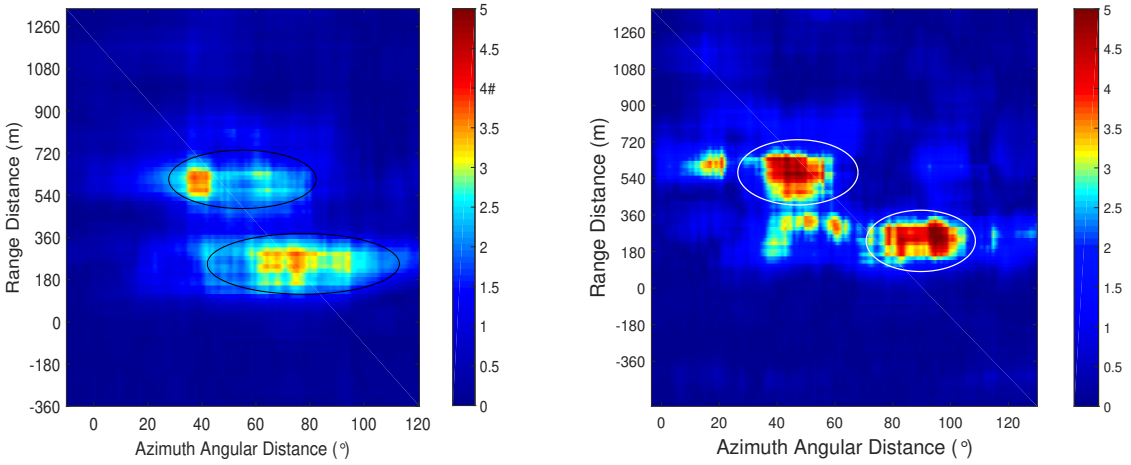


(a) (b)

Fig. 3.9: (a) GNSS-SAR image by the conventional imaging algorithm in case study 3.2 with increased azimuth matched filtering length; (b) GNSS-SAR image based on the proposed algorithm in case study 3.2 (color scale: pixel intensities sweep from the smallest value to the largest value)

TABLE 3.4: Computational complexity based on the parameter values

| Algorithms | Numbers of computations |
|---|---|
| Conventional GNSS-SAR imaging algorithm with the lengthened $M_s$ value | $\mathcal{O}\left(5.53 \times 10^{20}\right)$ |
| The proposed imaging algorithm | $\mathcal{O}\left(3.75 \times 10^{13}\right)$ |

TABLE 3.5: Algorithm speed

| Algorithms | Speed |
|---|---|
| Conventional imaging algorithm with lengthened $M_u$ and $M_s$ values | 38132.776 s |
| The proposed imaging algorithm | 3792.538 s |

during image formation is significantly increased, this largely slows down the algorithm speed as well.

In summary, the field experimental studies in the subsections 3.3.1 and 3.3.2 have demonstrated property 3.1 and property 3.2 in section 3.2.

## 3.4 Summary

This chapter proposes a new GNSS-SAR imaging algorithm under weak reflected signals to improve image quality, in which, the image quality is quantified based on compressed signal strength and the respective detectability. In the proposed algorithm, based on each pre-determined azimuth resolution cell, multiple non-overlapped mini slots are partitioned. Then before azimuth compression, the azimuthally distributed range compressed signals of migration correction are coherently added within each partitioned mini slot to improve the signal detectability and computational efficiency simultaneously. The results show that for ground based receiver, compared to conventional GNSS-SAR imaging algorithm, with a given detectability, the proposed algorithm can provided an obviously higher compressed gain in signal strength; under the same weak reflected signal strength, the proposed algorithm can give a significant higher detectability. Specifically, based on the experiment in this paper, the proposed imaging algorithm can still clearly detect the object when the received signal strength falls into $-160$ dBm, while the conventional one cannot. Meanwhile, the proposed algorithm is apparently

less time consumptive than the conventional GNSS-SAR imaging algorithm, in which, the computational speed is improved around 6 times.

However the proposed algorithm also has some limitations. At first, if the GNSS-SAR receiver is mounted in the space, which distance to earth surface is at the static level $10^7$ m, the received reflected signal strength can be far lower than $-160$ dBm. In this case, the values of (3.6) and (2.15) will be almost the same, which means that the proposed algorithm will not be that effective for the space-based receiver. At second, the determination method of azimuth cell length value $M_s$ and mini-slot length value $m_s$ has not been specifically considered in this research, as they are obtained through trials and errors tests. However the values $M_s$ and $m_s$ will also impact the image quality on the basis of azimuth resolution, because they are closely related to the receiver motion speed and object moving azimuth velocity (for moving object case). Therefore in our future work, firstly, we would like to jointly design the receiver parameters and imaging algorithm for space-based GNSS-SAR system to enhance object detection with a reflected signal strength far more lower than $-160$ dBm. Secondly, we will work on a mechanism to determine the suitable $M_s$ value and $m_s$ value for maintaining both imaging signal strength and azimuth resolution for the target detectability, a machine learning based approach [108] would be helpful to be implemented.

# Chapter 4

# Range Resolution Enhancement Using Intermediate Frequency Reflected Signals for Imaging

## 4.1 Introduction

In previous chapter, it can be seen that the objects formed by GNSS-SAR are with certain levels of ambiguities in range time domain. This is mainly because of the compressed pulse ambiguity caused by narrower bandwidths of baseband GNSS surveillance signals. Therefore to develop a new algorithm for range resolution enhancement by addressing signal ambiguity issue is very meaningful.

In this chapter, the main contribution is to propose a new range compression algorithm for GNSS-SAR imaging signal processing to improve range-compressed

resolution. In the proposed algorithm, within each azimuth bin, at first, the received intermediate frequency (IF) reflected GNSS signals of different delays are correlated with the synchronized direct baseband GNSS signal at the range domain for each azimuth bin for performing range compression, which aims to narrow down the main lobe duration of the compressed pulses. Then spectrum equalization [54] is applied to suppress side lobes of the compressed result for achieving the final range-compressed signal. The theoretical derivation, simulation results and field experimental results show that the proposed range compression algorithm can improve range resolution in the GNSS-SAR significantly, compared to conventional range compression algorithm. To be more specific, based on GPS C/A code signal receiver, the proposed algorithm can give the range resolution 40 m with IF value 4 MHz, while the best range resolution obtained by conventional range compression approach is only 171 m. Compared to the approaches in [96, 97, 98, 56], the proposed range compression algorithm for enhancing range resolution is more time efficient as there is no necessity for obtaining multiple full preliminary GNSS-SAR images; and the proposed range compression algorithm can separate targets within the original compressed ambiguity caused by GNSS ranging code. In summary, the research in this chapter provides a new knowledge that range resolution of GNSS-SAR can be adjusted based on IF values at receivers [63].

The rest of the chapter is organized as follows. Resolution of the proposed range compression algorithm is analyzed in Section 4.2. The simulation tests are provided in Section 4.3. Field experimental demonstration is provided in Section

4.4. Section 4.5 discusses the associated issues of this research as well as future developments. Section 4.6 provides the final concluding remark of the chapter.

## 4.2 Resolution of the Proposed Range Compression Algorithm

According to the analysis in chapter 2, it can be seen that one of the important approach to improve range resolution is to narrow down the main lobe ambiguity of the compressed pulse. According to [54] and [80], we can have that if a triangle function $\Lambda(\cdot)$ is modulated by a waveform with a frequency component larger than $B$, the main lobe will be significantly narrowed down. The auto-correlation of baseband GNSS signal can be seen in Fig. 4.1(a) and Fig. 4.2(a), while the correlation between IF and baseband GNSS signals are shown in Fig. 4.1(b).

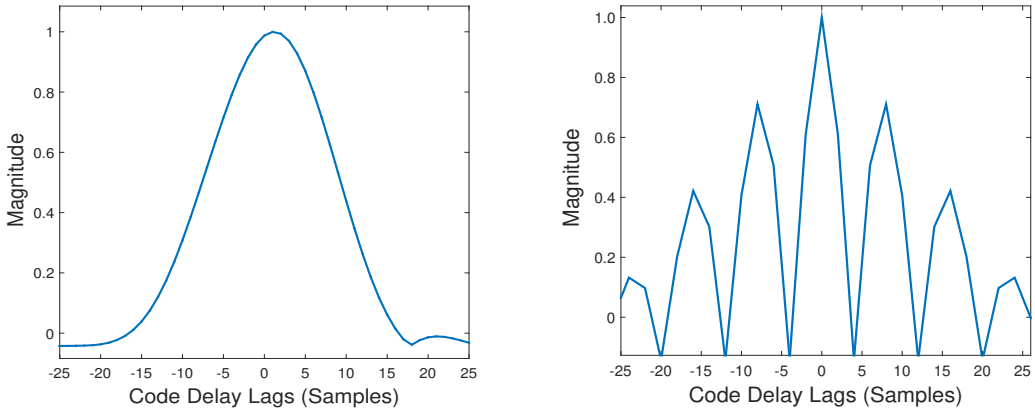


(a) (b)

Fig. 4.1: (a) Auto-correlation of baseband GNSS signal; (b) Correlation between IF and baseband GNSS signals (IF is assumed as 2 MHz)

If spectrum equalization is performed on Fig. 4.1(b), then the respective result can be seen in Fig. 4.2(b).

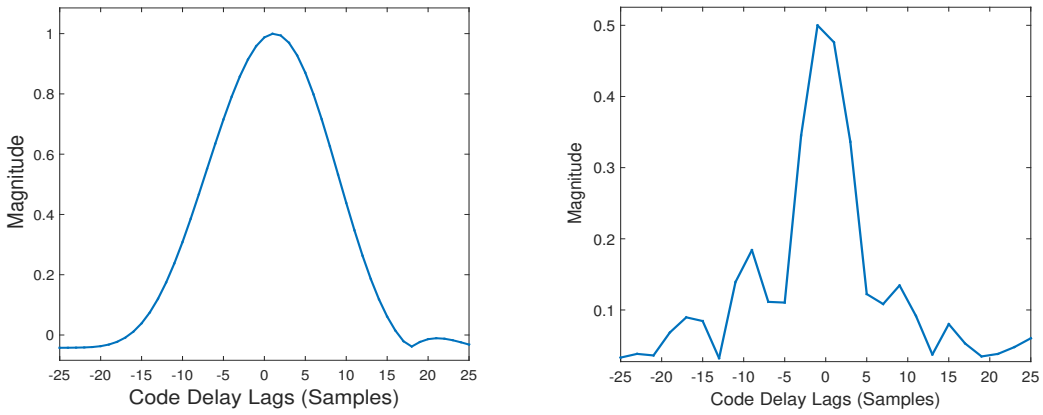


(a) (b)

Fig. 4.2: (a) Auto-correlation of baseband GNSS signal; (b) Correlation between IF and baseband GNSS signals after spectrum equalization (IF is assumed as 2 MHz)

Based on Fig. 4.1 and Fig. 4.2, it can be seen that using GNSS IF signal for performing correlation operation is very helpful for reducing the main-lobe ambiguity caused by PRN code correlation function, and spectrum equalization is another helpful tool for suppressing side-lobes. As for GNSS-SAR, range compression is identically the correlation operation between reflected GNSS signal and the respective local replica. Based on all these respects, in this chapter, we aim to use GNSS IF reflected signal for performing range compression for enhancing range resolution. Under the aim, a new range compression algorithm is proposed. The detailed steps of the proposed range compression algorithm can be seen in Fig. 4.3.

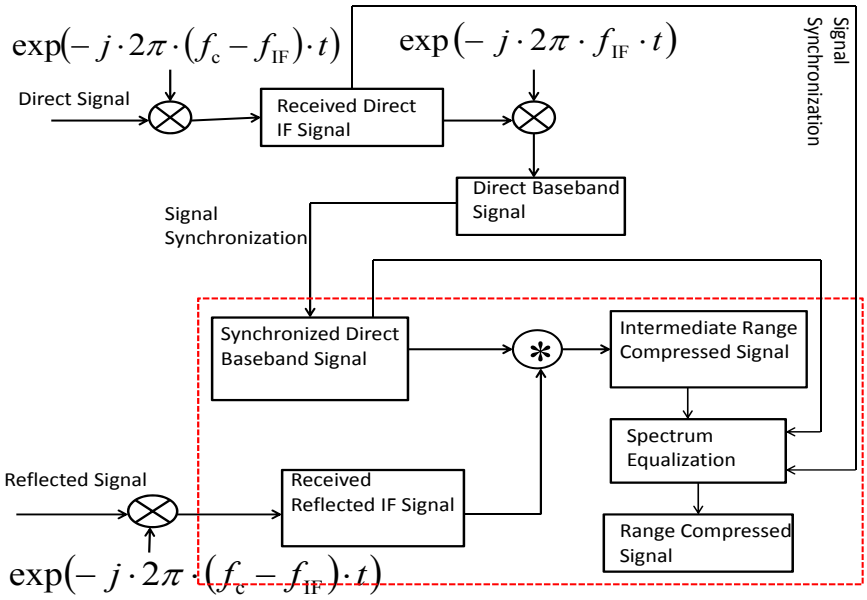


Fig. 4.3: The flow diagram of the proposed range compression algorithm in Chapter 4.

In Fig. 4.3, at GNSS RF front end, the signals (both direct and reflected) are converted to the IF band at the front-end GNSS receiver as well by the waveform component $\exp(-j2\pi\cdot(f_c - f_{\mathrm{IF}})\cdot t)$. However, in contrast to the conventional range compression algorithms, at the post-processing stage, only direct signal is converted to base-band for synchronization by the component $\exp(-j2\pi\cdot f_{\mathrm{IF}}\cdot t)$. Range compression is performed by correlating the received reflected GNSS IF signal with the synchronized direct GNSS baseband signal $s_{m\_f}$ in the range domain per azimuth bin. The noise absence term of the reflected GNSS IF signal per scattering point, denoted as $s_{r\_2}(\cdot)$ , can be expressed as follows:

$$
\begin{aligned}
s_{r\_2}(t,u) \quad &= A_r^l(t,u)\, C\left[t-\tau(u)-\tau_R^l(u)\right] \\
&\quad \times D\left[t-\tau(u)-\tau_R^l(u)\right] \\
&\quad \times \exp\left(j\left(2\pi\left(f_{\mathrm{IF}}+f_d(u)\right)\cdot t+\phi_r(u)\right)\right) \\
&\quad + n_r(t,u)
\end{aligned}
\tag{4.1}
$$

and the noise absence term with respect to intermediate range-compressed result (i.e., the noise absence result after performing $s_{r\_2} \circledast s_{m\_f}^*$) can be expressed as follows:

$$
\begin{aligned}
& s_{r\_2} \circledast s_{m\_f}^* \\
&\quad = A_r^l \cdot \Lambda\left(t-\tau(u)-\tau_R^l(u)\right) \\
&\qquad \times \exp\left(j\left(2\pi f_{\mathrm{IF}}\cdot t+\left(\phi_r(u)-\phi_d(u)\right)\right)\right).
\end{aligned}
\tag{4.2}
$$

In (4.2), the triangle function $\Lambda(\cdot)$ is modulated by the waveform with $f_{\mathrm{IF}}$ frequency component. Thus the main lobe duration of (4.2) is jointly determined by the triangle function $\Lambda(\cdot)$ and the waveform component. According to [80], the frequency of the signal (4.2) is derived as $f_{\mathrm{IF}}+B$.

Based on the intermediate range-compressed result (4.2), to suppress the compressed side lobes, spectrum equalization [54] is performed. When applying spectrum equalization technique in this paper, the detailed procedure in the module 'spectrum equalization' in Fig. 4.3 can be further presented as Fig. 4.4.

As we can see in Fig. 4.4, Fourier transform of intermediate range-compressed signal as (4.2) is conducted. The noise absence Fourier transformed result each

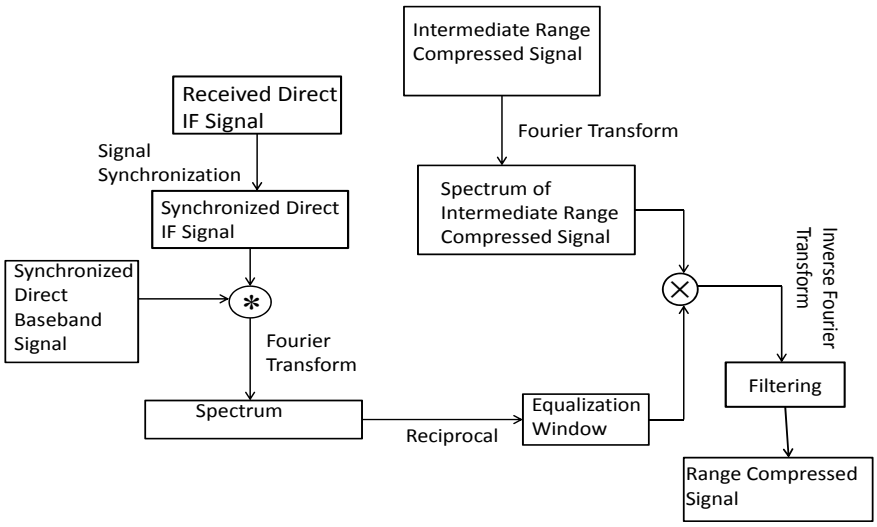


Fig. 4.4: The flow diagram of 'spectrum equalization' module of the proposed range compression algorithm in Chapter 4.

scattering point is expressed as follows

$$\begin{aligned}
&\mathcal{F}\left[s_{r_2} \circledast s_{m_f}^{*}\right] \\
&\quad = \int_{-\frac{T_s}{2}}^{\frac{T_s}{2}} A_r^l \cdot \Lambda\left(t-\tau\left(u\right)-\tau_R^l\left(u\right)\right) \\
&\qquad \times \exp\left(j\left(2\pi f_{\mathrm{IF}} \cdot t+\left(\phi_r\left(u\right)-\phi_d\left(u\right)\right)\right)\right) \\
&\qquad \times \exp\left(-j\omega \cdot t\right) dt \\
&\quad = A_r^l \cdot \exp\left(j\left(\phi_r\left(u\right)-\phi_d\left(u\right)\right)\right) \\
&\qquad \times \mathrm{sinc}^2\left(2\pi \cdot f_{\mathrm{IF}}-\omega\right)
\end{aligned} \tag{4.3}$$

where $T_s$ denotes the considered duration for performing range compression, which length is limited by one PRN code period; $\omega$ denotes the frequency range of the triangle function $\Lambda\left(\cdot\right)$ in (4.2) with an interval of $[-2\pi \cdot B, 2\pi \cdot B]$ and $\mathcal{F}\left[\cdot\right]$ represents Fourier transform. Meanwhile, the spectrum equalization window is

designed, which is based on the reciprocal of the spectrum with respect to the correlation between the synchronized direct IF signal $s_{m_{\mathrm{IF}}}$ and the synchronized direct base-band signal $s_{m\_f}$. In Fig. 4.4, the synchronized direct IF signal $s_{m_{\mathrm{IF}}}$ is given as follows:

$$\begin{aligned} s_{m_{\mathrm{IF}}}(t,u) &= C\left[t-\tau(u)\right] D\left[t-\tau(u)\right] \\ &\quad \times \exp\left(j\left(2\pi\left(f_{\mathrm{IF}}+f_d(u)\right)\cdot t+\phi_d(u)\right)\right) \end{aligned} \tag{4.4}$$

the correlated result between $s_{m_{\mathrm{IF}}}$ and $s_{m\_f}$ is given as:

$$\begin{aligned} & s_{m_{\mathrm{IF}}} \circledast s^*_{m\_f} \\ &= \Lambda\left(t-\tau(u)\right) \times \exp\left(j2\pi f_{\mathrm{IF}}\cdot t\right) \end{aligned} \tag{4.5}$$

and the spectrum of the correlated result is identical to the Fourier transform of (4.5), which can be expressed as

$$\mathcal{F}\left[s_{m_{\mathrm{IF}}} \circledast s^*_{m\_f}\right] = \mathrm{sinc}^2\left(2\pi\cdot f_{\mathrm{IF}}-\omega\right). \tag{4.6}$$

Then the equalization window is designed as follows

$$W = \begin{cases} \frac{1}{\mathcal{F}\left[s_{m_{\mathrm{IF}}} \circledast s^*_{m\_f}\right]} = \frac{1}{\mathrm{sinc}^2(2\pi\cdot f_{\mathrm{IF}}-\omega)}, & \text{when frequency } \epsilon\left[f_{\mathrm{IF}}-B, f_{\mathrm{IF}}+B\right] \\ 0, & \text{Otherwise} \end{cases}. \tag{4.7}$$

The key step of spectrum equalization is performed as follows:

$$\begin{aligned}
&\mathcal{F}\left[s_{r_2} \circledast s^*_{m_f}\right] \times W \\
&= \begin{cases} A_r^l \cdot \exp\left(j\left(\phi_r\left(u\right) - \phi_d\left(u\right)\right)\right), & \text{when frequency } \epsilon\left[f_{\mathrm{IF}} - B, f_{\mathrm{IF}} + B\right] \\ 0, & \text{otherwise} \end{cases}.
\end{aligned} \tag{4.8}$$

The equalized result is a rectangular function at frequency domain, where the rising edge appears at the frequency $f_{\mathrm{IF}} - B$ and the falling edge appears at the frequency $f_{\mathrm{IF}} + B$. Due to the fact that spectrum equalization is conducted at frequency domain, side lobes of the reflected signals at different range positions can be suppressed simultaneously.

To obtain the final range-compressed signal each scattering point, inverse Fourier transform based on the spectrum equalized result shown in (4.8) with respect to $\tau_R^l$ is conducted, which result is expressed as follows

$$\begin{aligned}
&\mathcal{F}^{-1}\left\{\mathcal{F}\left[s_{r_2} \circledast s^*_{m_f}\right] \times W\right\} \\
&\quad = \tfrac{1}{2\pi} \cdot A_r^l \cdot \exp\left(j\left(\phi_r\left(u\right) - \phi_d\left(u\right)\right)\right) \times \tfrac{1}{j \cdot \left(t - \tau(u) - \tau_R^l(u)\right)} \\
&\qquad \times \Big\{2 \cdot \sin\left(2\pi \cdot f_{\mathrm{IF}} \cdot \left(t - \tau\left(u\right) - \tau_R^l\left(u\right)\right)\right) \\
&\qquad\quad \times \sin\left(-2\pi \cdot B \cdot \left(t - \tau\left(u\right) - \tau_R^l\left(u\right)\right)\right) \\
&\qquad\quad + j \cdot \sin\left(2\pi \cdot \left(f_{\mathrm{IF}} + B\right) \cdot \left(t - \tau\left(u\right) - \tau_R^l\left(u\right)\right)\right) \\
&\qquad\quad + j \cdot \sin\left(2\pi \cdot \left(B - f_{\mathrm{IF}}\right) \cdot \left(t - \tau\left(u\right) - \tau_R^l\left(u\right)\right)\right)\Big\}
\end{aligned} \tag{4.9}$$

where $\mathcal{F}^{-1}$ represents inverse Fourier transform. The detailed derivation of (4.9)

can be seen in Appendix A. To extract the sharpest pulse duration component, the frequency components lower than $f_{\mathrm{IF}}+B$ in (4.9) are filtered out. Then the final range-compressed signal module per scattering point in Fig. 4.3 and Fig. 4.4 with regard to noise absence term is expressed as follows

$$\begin{aligned} & R_{c\_\mathrm{proposed}} \\ & \quad = A_r^l \cdot \exp\left(j\left(\phi_r\left(u\right)-\phi_d\left(u\right)\right)\right) \times \left(f_{\mathrm{IF}}+B\right) \\ & \qquad \times \mathrm{sinc}\left(2\pi \cdot \left(f_{\mathrm{IF}}+B\right) \cdot \left(t-\tau\left(u\right)-\tau_R^l\left(u\right)\right)\right) \end{aligned} \tag{4.10}$$

where $R_{c\_\mathrm{proposed}}$ represents the final range compressed signal of the proposed range compression algorithm. The detailed derivation of (4.10) can be seen in Appendix A as well. In (4.10), it can be seen that $\mathrm{sinc}\left(\cdot\right)$ function is only the term with respect to range delay $\tau_R^l$ for both real and imaginary parts. Therefore the compressed pulse duration is determined by the main lobe of $\mathrm{sinc}\left(\cdot\right)$ function, and can be derived as $\frac{1}{f_{\mathrm{IF}}+B}$. Compared to (5.1), the main lobe of (4.10) is reduced by the factor $1+\frac{f_{\mathrm{IF}}}{B}$. And the attainable range resolution with regard to the compressed pulse is 0.586 of the $\mathrm{sinc}\left(\cdot\right)$ function main lobe duration, which can be expressed as:

$$\delta_{R_2} = 0.586 \cdot \frac{c}{\cos\left(\beta/2\right) \cdot \left(f_{\mathrm{IF}}+B\right)} \tag{4.11}$$

where $\delta_{R_2}$ denotes the range resolution obtained by the proposed algorithm. It can be seen that (4.11) is $\frac{1}{1+f_{\mathrm{IF}}/B}$ times superior than the range resolution (2.17) pro-

vided by the conventional range compression algorithm. Meanwhile, from (4.10), we can see that the reflected phase information $\phi_r^l - \phi_d$ is still preserved.

For selecting the IF value in the proposed algorithm, sampling frequency of the employed GNSS receiver should be taken into consideration. Denoting the sampling frequency of the GNSS receiver as $f_s$, according to sampling theory [110], the condition $f_{\mathrm{IF}} + B \leq \frac{1}{2} f_s$ should be satisfied. To make the proposed algorithm effective, the condition $f_{\mathrm{IF}} + B > B$ should be satisfied at the same time as well. Therefore, the determination of $f_{\mathrm{IF}}$ value should satisfy the following constraint:

$$0 < f_{\mathrm{IF}} \leq \frac{1}{2} f_s - B. \tag{4.12}$$

Finally, azimuth compression is conducted for forming the full GNSS-SAR image based on (4.10) with different differential phase value $\phi_r^l(u) - \phi_d(u)$ in the azimuth domain [23, 33].

## 4.3 The Simulation Experiment

To test the proposed algorithm for enhancing range resolution, simulations of the GNSS-SAR based on the standard GPS C/A code signal software defined receiver configuration are carried out in this section as an example. We consider that the objects and GNSS-SAR receiver located in the same horizontal coordinate. Therefore, the bi-static angle $\beta$ can be considered as zero [23, 36]. Based on the mode, range resolutions of the conventional algorithm and the proposed algorithm

TABLE 4.1: The parameter values for Chapter 4

| Parameters | Values |
|---|---|
| Signals type | GPS C/A code signal |
| Signal wavelength | 0.19m (L1 band) |
| PRN code chip rate $B$ | 1.023 MHz |
| Signal transmission frequency $f_c$ | 1575.42MHz (L1 band) |
| Signal transmission speed $c$ | $3 \times 10^8$m/s |
| The length of each code period | 1 ms |
| Sampling frequency | 16.368 MHz |
| Experimental temperature $T$ | 300 K |
| Boltzmann constant $k$ | $1.38 \times 10^{-23}$ |
| Antenna + RF gains | 20 dB |

are expressed as follows, respectively,

$$\delta'_{R_1} = 0.586 \cdot \frac{c}{B} \tag{4.13}$$

and

$$\delta'_{R_2} = 0.586 \cdot \frac{c}{(f_{\text{IF}} + B)}. \tag{4.14}$$

The parameter values of the considered GPS C/A code receiver are given in TABLE 4.1.

Based on the sampling frequency value in TABLE 4.1 and the constraint (4.12), two different IF frequencies $f_{\text{IF}_1} = 2.092$ MHz and $f_{\text{IF}_2} = 5.115$ MHz are employed in the simulation tests. Theoretically based on (4.13), range resolution for the conventional algorithm can be achieved at the level of 171 m. For the proposed algorithm, based on (4.14), range resolution can be obtained at the levels of 56 m

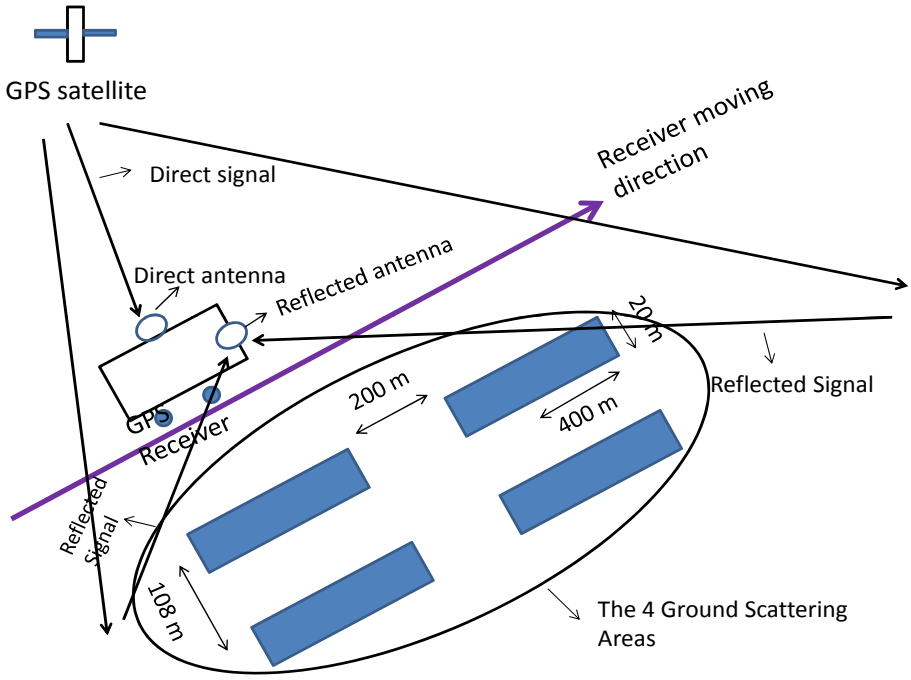


Fig. 4.5: The simulation scenario.

and 28 m with $f_{\mathrm{IF}_1}$ and $f_{\mathrm{IF}_2}$, respectively in theoretical.

To verify the proposed range compression algorithm, a simulation test is carried out. The purpose for the simulation is to test whether the proposed algorithm can separate objects with a range distance difference less than 171 m, using the parameters in TABLE 4.1. The simulation experiment is set out as shown in Fig. 4.5. In the simulation test, a moving receiver case and a short-range geometry is considered.

In Fig. 4.5, four strong reflection objects with length of 400 m and width of 18 m are arranged with 200 m along the azimuth direction and 108 m with the range direction. The reflectabilities of the strong reflection objects are higher than 90%, while no reflections from the background. The direct and surveillance antennas are moving along the azimuth direction by a vehicle with a constant speed to

perform synthetic aperture. The GPS data are simulated using parameters listed in Table 4.1. The channels of both direct and surveillance antenna are assumed to be additive white Gaussian Noise (AWGN) channel. The received direct and reflected signals for the simulation are generated based on the models (2.4) and (2.5), respectively. Based on the set ups in Fig. 4.5, the GNSS-SAR images (both 2-D and 3-D view) generated by both conventional range compression algorithm and the proposed range compression algorithm in this chapter are given in Fig. 4.6. Similarly, we normalized the image obtained by the conventional algorithm, while the images obtained by the proposed algorithm are zoomed out the at the level of the normalization factor.

As can be seen in Fig. 4.6(b), (c) (Fig. 4.6 (e), (f)), due to the fact that the proposed range compression algorithm can offer a superior range resolution, the four scattering areas in Fig. 4.5 can be well separated. Through the comparisons, Fig. 4.6(c) (Fig. 4.6(f)) has a less range ambiguity because a higher IF value is employed at the GPS receiver. In Fig. 4.6(a) (Fig. 4.6(d)), the two scatters located at different range positions cannot be separated on the GNSS-SAR image with the conventional range compression algorithms, as the resolution of this algorithm is around 171 m according to (4.13) with the code ambiguity restraint $B = 1.023$ MHz.

In summary, the simulation results in this section have demonstrated that the proposed range compression algorithm can provide a superior range resolution to the conventional range compression algorithm.

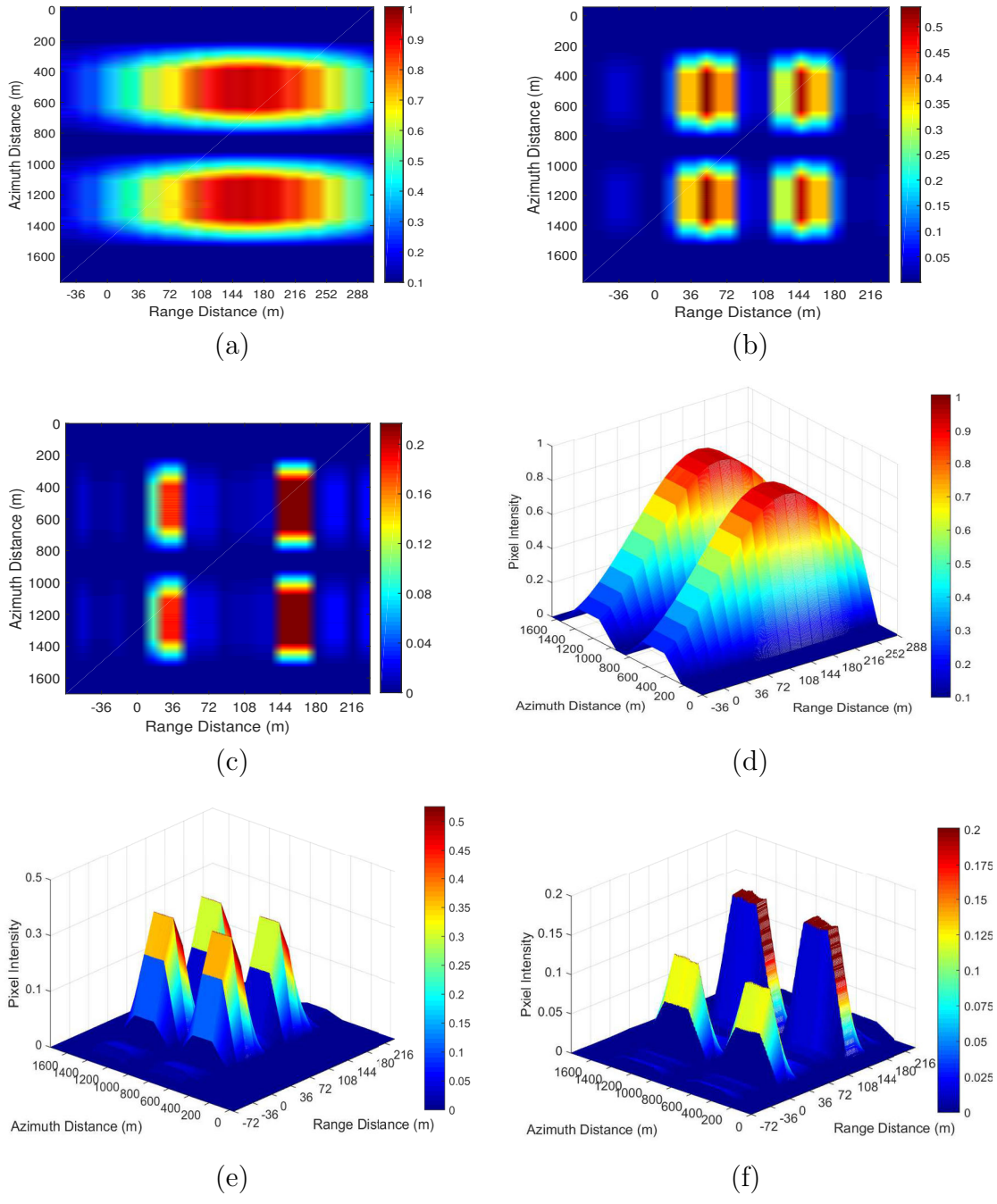


Fig. 4.6: (a) GNSS-SAR image generated by the conventional range compression algorithm; (b) GNSS-SAR image generated by the proposed range compression algorithm with $f_{\mathrm{IF}_1} = 2.092\,\mathrm{MHz}$; (c) GNSS-SAR image generated by the proposed range compression algorithm with $f_{\mathrm{IF}_2} = 5.115\,\mathrm{MHz}$; (d) Three-dimensional image of (a); (e) Three-dimensional image of (b); (f) Three-dimensional image of (c) (color scale: pixel intensities in the images sweep from the smallest value to the largest value).

## 4.4 Field Experimental Verification

To further demonstrate the proposed range compression algorithm, a field experiment is carried out to evaluate the range compressed ambiguity correspondingly. The employed GNSS software defined receiver RF front end is the mode GPS ET09/C, developed and produced by ip-solutions (http://www.ip-solutions.jp), shown in Fig. 3.3(b), where the IF value determined by the manufacture is 4 MHz. The geometric positions of direct and surveillance antennas are given the same as Fig. 3.3(a), where the synthetic aperture for SAR imaging is achieved by the angular movement of the surveillance antenna. The utilized GNSS signal as source of opportunity is still GPS C/A code signal. Based on the geometric position for maximally prevent direct signal interference, the satellite PRN 15 is chosen for SAR imaging. The rest of parameters for the field experiment is the same as TABLE 4.1. The data flow is similar as Fig. 3.4, where the main difference in the section is that the output at surveillance channel of RF front end is reflected IF signal.

The experiment was carried out at Victoria Harbour, Hong Kong. The optical image for the field experiment can be seen in Fig. 4.7.

In Fig. 4.7, the targets are two strong reflection boards with a surface area 0.2 $m^2$. One is located at the range position 6 m, and the other is located at the range position 70 m, relative to the receiver's location (noted as 0 m in Fig. 4.7). We continue to use the circular movement trace of the surveillance antenna for form-


Fig. 4.7: The optical image of the field experiment in Chapter 4.

ing synthetic aperture, which duration is 100° angular distance. Along the moving trace, the board at 70 m range position is earlier being covered by surveillance antenna region than the one at 6 m range position. Based on the experimental set-up, the obtained GNSS-SAR images with respect to both conventional range compression algorithm and the proposed range compression algorithm in this chapter are illustrated in Fig. 4.8(a) and (b), respectively. Fig. 4.8(a) is normalized, Fig. 4.8(b) is zoomed out by the level as the normalization factor of Fig. 4.8(a).

Compare Fig. 4.8 (b) to (a), it can be seen that apparently, two objects at different range positions can be distinguished using the proposed range compression algorithm (see Fig. 4.8(b)), through a coarse measurement on Fig. 4.8(b), indeed, range distance between the centers of the two illuminated regions is around 70 m. However in Fig. 4.8(a), with the conventional range compression algorithm, due to the narrow bandwidth of base-band GPS C/A code signal, the best range

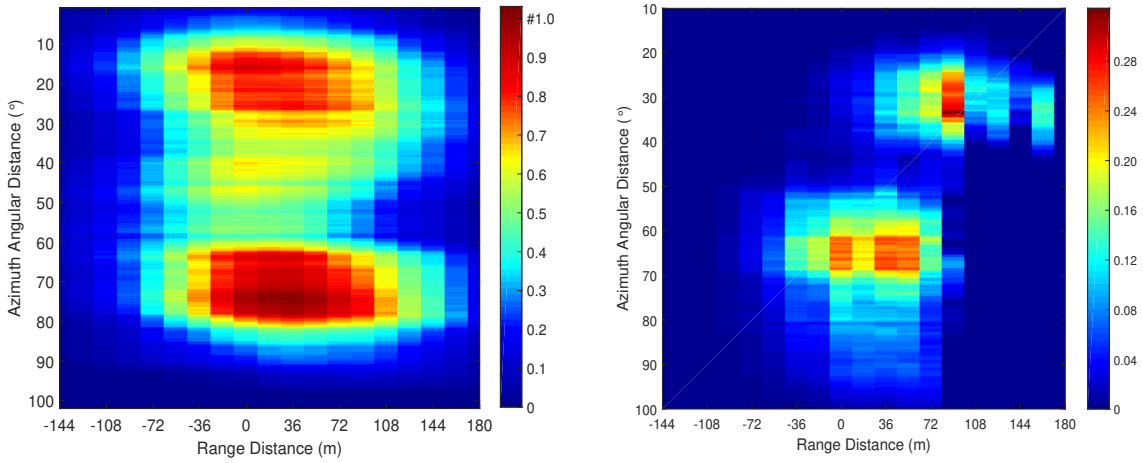


(a) (b)

Fig. 4.8: (a) GNSS-SAR image based on field experimental data with regard to the conventional range compression algorithm; (b) GNSS-SAR image based on field experimental data with regard to the proposed range compression algorithm (color scale: pixel intensities in the images sweep from the smallest value to the largest value).

resolution, which obtained on the basis of code correlation function, can be only achieved at the level 171 m. Therefore it is hard to distinguish two objects at different range positions in Fig. 4.8(a).

In conclusion, the property of the proposed algorithm is confirmed by the field experimental results as well.

Furthermore through tests, the proposed range compression algorithm is also applicable for the GNSS-SAR receiver based on the other GNSS signals of opportunity. In the standard GNSS receivers, the IF value is typically higher than baseband frequency (which equals the PRN code chip rate) of the corresponding compatible signal. Therefore, a superior range resolution should be achieved by employing the proposed range compression algorithm. However, because the

GNSS receivers differ in the PRN code types and IF values for signal reception, the achievable range resolutions by the proposed algorithm will varies among the receivers.

## 4.5 Discussion

### 4.5.1 Discussion on the Associated Issues

Based on the theoretical derivation, simulation experiment and field experiment, it has been demonstrated that the proposed range compression algorithm enhances range resolution significantly more than the conventional range compression algorithm during the GNSS-SAR imaging procedure. For instance, in joint Galileo E5 signal receiver-based GNSS-SARs (where the original range resolution is 3 m [54, 55]), the range resolution can be potentially obtained at a level less than 1 m using the proposed range compression algorithm. For the bistatic GNSS-SAR where range and azimuth direction are not orthogonal [67, 42], although imaging performance will be largely impacted by other factors, such as the angle between range and azimuth direction, besides range and azimuth resolution indicators, using the proposed range compression algorithm for obtaining superior range resolution value can still help in achieving higher quality images. However, according to Fig. 4.1, Fig. 4.2, Fig. 4.6 and Fig. 4.8, it can be seen that the magnitude or the scene illumination level decreases with respect to $f_{\mathrm{IF}}$ values. This is because when performing spectrum equalization, signal-to-noise

ratio (SNR) will be decreased with respect to the selected cutoff frequency [54], which is the main associated problem of the proposed range compression algorithm compared to multi-static image processing [44, 56]. Since the mathematical expression of SNR loss caused by spectrum equalization is introduced in [54, 55], it is omitted at here. According to the corresponding mathematical expression in [54, 55], it can be seen that by performing spectrum equalization, SNR will decrease at approximated the same amount as the ratio between the selected cutoff frequency and the preliminary frequency. Considering in this chapter, this equally means that the signal strength will decrease with the approximated the same amount of the increment in range resolution. The phenomenon can be seen in both simulation and field experimental results. Assume $N_e$ is required range sample for performing the sensing within the expected range distance on the basis of accepted signal strength level, combining (4.12), the further constraint of $f_{\text{IF}}$ value can be derived as follows

$$f_{\text{IF}} \leq \min\left[\frac{1}{2}f_s - B, B \times \left(\frac{N_t}{N_e} - 1\right)\right] \tag{4.15}$$

Since GNSSs are low-equivalent isotropically radiated power (EIRP) sources, losses in SNR cannot be so easily tolerated. However, using lengthened integration when performing azimuth compression or coherently accumulating the range compressed signals within mini-azimuth slot as the algorithm in Chapter 3 before performing spectrum equalization can help to mitigate SNR losses. And in some specific oper-

ative scenarios such as the permanent monitoring of bridges or mines by employing a close receiver, the losses in SNR can be acceptable.

Taking into account another associated issue, time consumption, we study it based on judging the load with regard to the number of operations. For multi-static image processing [44, 56] for improving resolution, we can easily see that the method is more time consuming than the proposed algorithm because it is applied based on generating multiple full preliminary GNSS-SAR images. Also, the availability of a multiple perspective exploiting multiple transmitter is not intended for the range resolution improvement, but provides the capability of exploiting spatial diversity in different ways. Therefore we do not compare the works [44, 56] with this chapter in detail. Comparing the proposed range compression algorithm with a conventional range compression algorithm, the former has a higher computational load due to the fact that spectrum equalization is used. To quantify the computational load, the corresponding analysis is provided as follows. Assume for received GNSS signal (both direct and reflected), there are $N_t$ samples at the range domain, $M_u$ samples at the azimuth domain, $N_s$ samples are used for range compression and $M_s$ samples for azimuth resolution cell length. For GNSS-SAR imaging based on the conventional range compression algorithm, there is $\mathcal{O}(N_s \times N_t \times M_u)$ number of operations throughout the range compression state, $\mathcal{O}(M_s \times M_u \times N_s)$ number of operations for azimuth compression per resolution cell and $\mathcal{O}((M_u - M_s) \times M_s \times M_u \times N_s)$ number of operations throughput whole azimuth compression state. Thus, the accumulated number of operations during

imaging is:

$$\mathcal{O}\left(N_s \times N_t \times M_u + (M_u - M_s) \times M_s \times M_u \times N_s\right). \tag{4.16}$$

For GNSS-SAR imaging based on the proposed range compression algorithm, for range processing of each azimuth bin, there additionally exists $\mathcal{O}\left(N_s \times N_t\right)$ number of operations for performing (4.5), $\mathcal{O}\left(N_s \cdot \log\left(N_s\right)\right)$ number of operations for performing (4.3), (4.6) and (4.10) respectively, as well as $\mathcal{O}\left(N_s\right)$ number of operations for performing (4.8). Fourier transform does not change the sample quantity. The numbers of operations for designing a spectrum equalization window is very small, which can be neglected when compared with imaging computations. For azimuth processing, the numbers of operations are the same as GNSS-SAR imaging based on the conventional range compression algorithm. Therefore the accumulated number of operations during imaging can be derived as:

$$\mathcal{O}\left(\left(2 \cdot \left(N_s \times N_t\right) + 3N_s \cdot \log\left(N_s\right) + N_s\right) \times M_u + (M_u - M_s) \times M_s \times M_u \times N_s\right) \tag{4.17}$$

where $\mathcal{O}\left(\left(2 \cdot \left(N_s \times N_t\right) + 3N_s \cdot \log\left(N_s\right) + N_s\right) \times M_u\right)$ is for range processing. It can be seen that the value of (4.17) is higher than (4.16). This indicates that the proposed range compression algorithm has a higher processing delay than the conventional range compression algorithm.

Although the proposed range compression algorithm has been demonstrated

in GNSS-SAR in this paper, due to the signal structure difference, the feasibility of the proposed algorithm in the passive radar system using other signals of opportunity besides GNSS still needs to be further studied.

### 4.5.2 Future Development

Based on the analysis above, in our future work, firstly, we will test the feasibility of the proposed range compression algorithm in the passive radar system using other sources of opportunity besides GNSS, and modify the proposed algorithm based on the corresponding signal structures. Secondly, we would like to develop a mechanism for GNSS-SAR receivers for trade-off among range resolution, range-compressed SNR degradation and compressed delay together with the corresponding field experimental studies. A machine learning [108] based approach might be helpful to be employed.

## 4.6 Summary

In this chapter, a novel range compression algorithm for enhancing the resolution of the GNSS-SAR is proposed. In range compression, the received reflected IF GNSS signal is correlated with the synchronized direct baseband signal in the range domain for each azimuth bin to narrow down the main lobe ambiguity of the compressed pulse. Then, side lobes of the range-compressed result are suppressed by a proper designed spectrum equalization window. Both theoretical

derivation, simulation and field experimental results have demonstrated that the proposed range compression algorithm can provide a superior range resolution compared to the conventional range compression algorithm in the GNSS-SAR. Moreover, the proposed algorithm is less time-consuming than multi-static image processing [44, 56] due to the fact that it is applied without the necessity for generating multiple full preliminary images, and can distinguish the targets within the original compressed ambiguity caused by the conventional range compression algorithm.

Meanwhile, a non-negligible main limitation of the proposed range compression algorithm is the loss in SNR. However, lengthened integration during azimuth compression for imaging or properly combining the proposed imaging algorithm in Chapter 3 will relieve SNR losses, as the imaging gain is enhanced. And under the specific operative scenarios such as the permanent monitoring of bridges or mines using a close GNSS-SAR receiver, the SNR losses can be acceptable.

In summary, the research in this chapter should provide a novel idea that GNSS-SAR range resolution enhancement can be achieved through adjusting the receivers IF values.

# Chapter 5

# Range Resolution Improvement based on Diff2 Peak Extraction Scheme for Imaging

## 5.1 Introduction

From Chapter 4, with a given bi-static angle, the essential step to improve range resolution is to narrow down range compressed ambiguity caused by PRN code correlation function. According to [105], it can be seen that for multi-path estimation on the basis of peak extraction, if second-order differentiation is applied on the squared GNSS signal correlation function, which known as Diff2 peak extraction scheme, the main-lobe of code correlation function can be significantly reduced as well. Within this point, in this chapter, we are going to test the feasibility for

applying Diff2 peak extraction scheme to range compression in GNSS-SAR imaging for enhancing range resolution. Based on the goal, different from Chapter 4, another new range compression algorithm is proposed. In the proposed algorithm, to narrow down range ambiguity by extracting the correlation peaks, second order differentiation is applied to the squared function of range compressed signals with respect to range delay each azimuth bin. Since carrier phase is changed during the squaring processing, to preserve carrier phase value for azimuth compression, a phase recovery procedure is then carried out. Both simulation and field experimental results shown that based on the GPS C/A code signal receiver with the sampling frequency $1.6 \times 10^7$ Hz as an example, the proposed imaging algorithm can increase range resolution to 36 m from 171 m [65].

The rest of the chapter is organized as follows. The proposed range compression algorithm based on Diff2 peak extraction scheme is illustrated in section 5.2, while the corresponding range resolution is analyzed in the same section. The simulation and experimental validation of the proposed imaging algorithm are given in section 5.3 and section 5.4, respectively. Final concluding remark and future work are shown in section 5.5.

## 5.2 The Proposed High Range Resolution Imaging Algorithm

Diff2 scheme was primarily used in GNSS signal code tracking for multi-path mitigation. With this scheme, by taking secondary order differentiation of code correlation function, multi-path signals from different code delays can be separated [105]. The schematic diagram with respect to the application of Diff2 scheme to code correlation function can be seen in Fig. 5.1. The normalized code correlation function $\Lambda(\cdot)$ and Diff2 of the squared $\Lambda(\cdot)$ are plotted in Fig. 5.1(a), while the normalized summation of $\Lambda(\cdot)$ with different code delay lag and the normalized Diff2 of the square of code correlation function summation are plotted in Fig.5.1(b) and (c).

In Fig. 5.1, we can see that Diff2 peak extraction method is very helpful for narrowing the code correlation function ambiguity. With this scheme, the multi-path code sequence separated by merely two code delay lags can be distinguished. As for range compression for GNSS-SAR imaging, with the fixed observation angle, the main-lobe ambiguity only determines by the ambiguity of the respective code correlation function, and range delay lag is identically the code delay lags. Therefore, theoretically it would be feasible that improving range resolution by applying Diff2 scheme to GNSS-SAR range compression procedure. In this remit, we propose a range compression algorithm based on Diff2 peak extraction scheme. The detail steps of the proposed range compression algorithm are analyzed as

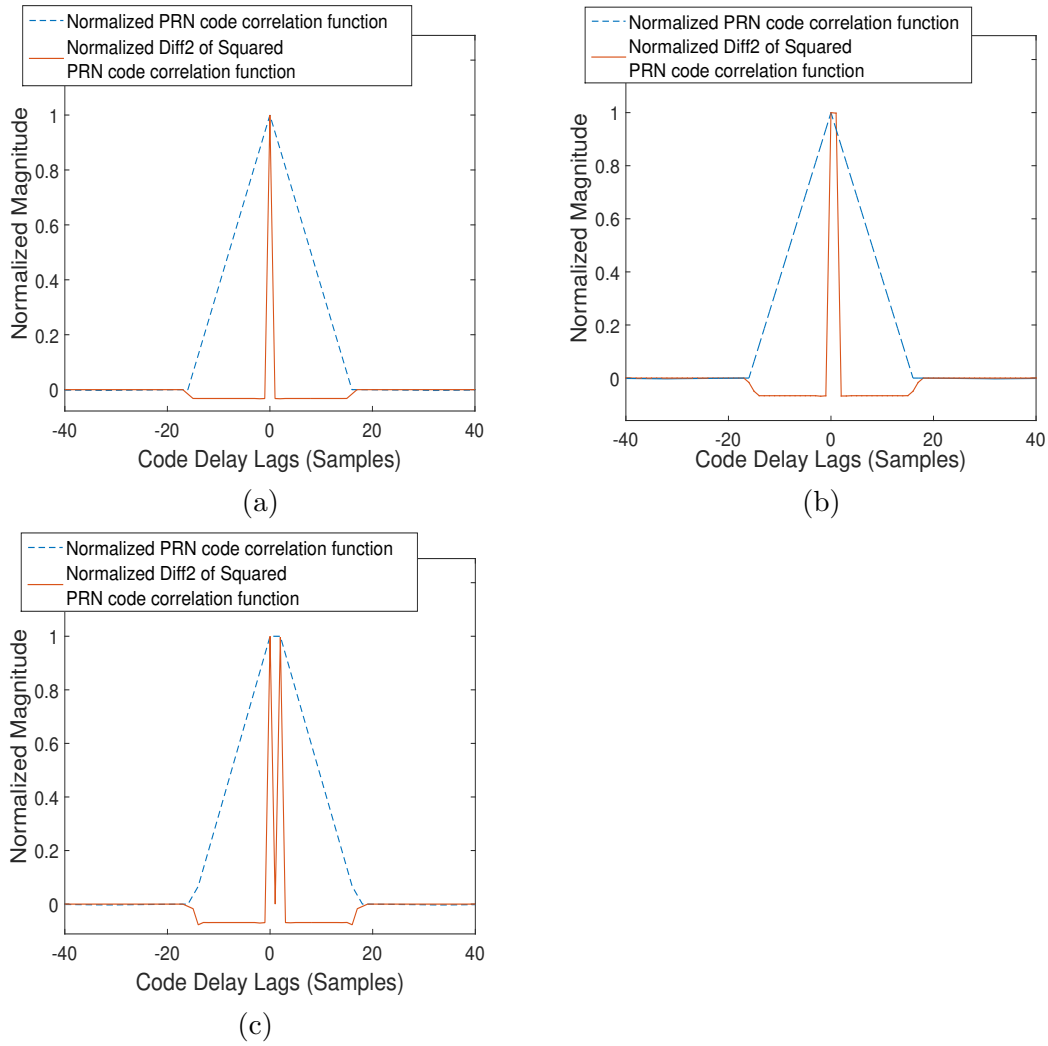


Fig. 5.1: Normalized PRN code correlation function & normalized Diff2 of squared PRN code correlation function: (a) One path PRN code sequence case, (b) Two paths PRN code sequence case with one code delay lag, (c) Two paths PRN code sequence case with two code delay lags.

follows.

The initial stage of the proposed algorithm is in the same manner as the range compression of the conventional algorithm as quadrature demodulation, signal synchronization and range signal correlation for the compression. The obtained matched filter signal is expressed as (2.7), and the intermediate range compressed signal in the form of a summation of each range delay can be expressed as follows

$$\begin{aligned} &R_{\text{in}}\left(\tau_R^l, u\right) \\ &\quad = \left(\sum_{l=0}^{N_R-1} A_r^l\left(t,u\right)\cdot\Lambda\left(t-\tau\left(u\right)-\tau_R^l\left(u\right)\right)\right)\times\exp\left(j\left(\phi_r\left(u\right)-\phi_d\left(u\right)\right)\right) \end{aligned} \tag{5.1}$$

where $l$ represents range delays of reflected signals and $N_R$ represents total reflected signal samples.

To obtain the squared code correlation function, the intermediate range compressed signal function is arithmetical squared, which can be expressed as

$$\begin{aligned} R^2 &= \left(R_{\text{in}}\left(\tau_R^l, u\right)\right)^2 \\ &= \left(\sum_{l=0}^{N_R-1} A_r^l\left(t,u\right)\cdot\left(\Lambda\left(t-\tau\left(u\right)-\tau_R^l\left(u\right)\right)\right)\right)^2 \\ &\qquad \times\exp\left(j2\left(\phi_r\left(u\right)-\phi_d\left(u\right)\right)\right). \end{aligned} \tag{5.2}$$

Thereafter, the second order differentiation of $R^2$ with respect to each com-

pressed pulse delay $\tau_R^l$ is carried out, which can be expressed as follows

$$\begin{aligned}
&\frac{\partial^2}{\partial\left(\tau_R^l(u)\right)^2}\left(R^2\right) \\
&\quad=\frac{\partial^2}{\partial\left(\tau_R^l(u)\right)^2}\left(\sum_{l=0}^{N_R-1} A_r^l\left(t,u\right)\cdot\left(\Lambda\left(t-\tau\left(u\right)-\tau_R^l\left(u\right)\right)\right)\right)^2 \\
&\qquad\times\exp\left(j2\left(\phi_r\left(u\right)-\phi_d\left(u\right)\right)\right)
\end{aligned} \tag{5.3}$$

where the peaks of the term $\frac{\partial^2}{\partial\left(\tau_R^l(u)\right)^2}\left(\sum_{l=0}^{N_R-1} A_r^l\left(t,u\right)\cdot\left(\Lambda\left(t-\tau\left(u\right)-\tau_R^l\left(u\right)\right)\right)\right)^2$ can be determined as follows [105]

$$\begin{aligned}
\text{Diff2}_{\text{Peak}} = \ \forall x_i \Bigg\{ \Bigg( & x_i \in \frac{\partial^2}{\partial\left(\tau_R^l(u)\right)^2}\left(\sum_{l=0}^{N_R-1} A_r^l\left(t,u\right)\cdot\left(\Lambda\left(t-\tau\left(u\right)-\tau_R^l\left(u\right)\right)\right)\right)^2 \Bigg) \\
& \wedge\left(x_i \geq x_i-1\right)\wedge\left(x_i \geq x_i+1\right)\wedge\left(x_i \geq \text{Diff2}_{\text{Thresh}}\right)\Bigg\}; \\
& \qquad\qquad i=2,3,...,l_{\text{Diff2}}-1
\end{aligned} \tag{5.4}$$

where $l_{\text{Diff2}}$ is the length of Diff2 and $\text{Diff2}_{\text{Thresh}}$ is the threshold of Diff2. The determination of $\text{Diff2}_{\text{Thresh}}$ should follow [105]

$$\begin{aligned}
\text{Diff2}_{\text{Thresh}} = \ & \max\left(\frac{\partial^2}{\left(\partial\tau_R^l(u)\right)^2}\left(\sum_{l=0}^{N_R-1} A_r^l\left(t,u\right)\cdot\left(\Lambda\left(t-\tau\left(u\right)-\tau_R^l\left(u\right)\right)\right)\right)^2\right)\cdot w \\
& +Thresh_{\text{noise}}
\end{aligned} \tag{5.5}$$

where $Thresh_{\text{noise}}$ represents noise threshold, which can be estimated through range compression per azimuth bin; $w$ represents the weighting factor, which value is in the interval $[0.22, 0.3]$ for binary phase shift keying (BPSK) signal, for instance GPS L1 signal, and $[0.37, 0.5]$ for SinBOC(1,1) signal [105].

Based on (5.3), it can be seen that the original carrier phase term is distorted.

However for performing the further step azimuth compression, original carrier phase should be preserved. Therefore to obtain the final range compressed signal, a processing with regard to original carrier phase recovery by multiply the component $\exp\left(-j\left(\phi_r-\phi_d\right)\right)$ should be carried out. In this processing, firstly the tangent value of the carrier phase in (5.3) is obtained as follows

$$\begin{aligned}\tan\left(2\left(\phi_r-\phi_d\right)\right) &= \frac{\sin(2(\phi_r-\phi_d))}{\cos(2(\phi_r-\phi_d))} \\ &= \frac{\text{Imag}\left(\frac{\partial^2}{\partial\left(\tau_R^l(u)\right)^2}\left(R^2\right)\right)}{\text{Real}\left(\frac{\partial^2}{\partial\left(\tau_R^l(u)\right)^2}\left(R^2\right)\right)}\end{aligned} \tag{5.6}$$

where 'Imag' represents the imaginary part and 'Real' represents the real part. Then we can have

$$\phi_r-\phi_d=\frac{1}{2}\arctan\left(\frac{\text{Imag}\left(\frac{\partial^2}{\partial\left(\tau_R^l(u)\right)^2}\left(R^2\right)\right)}{\text{Real}\left(\frac{\partial^2}{\partial\left(\tau_R^l(u)\right)^2}\left(R^2\right)\right)}\right). \tag{5.7}$$

Thus the component $\exp\left(-j\left(\phi_r-\phi_d\right)\right)$ is generated as the following form

$$\exp\left(-j\frac{1}{2}\arctan\left(\frac{\text{Imag}\left(\frac{\partial^2}{\partial\left(\tau_R^l(u)\right)^2}\left(R^2\right)\right)}{\text{Real}\left(\frac{\partial^2}{\partial\left(\tau_R^l(u)\right)^2}\left(R^2\right)\right)}\right)\right) \tag{5.8}$$

and the final range compressed signal is obtained as

$$
\begin{aligned}
&R_p\left(\tau_R^l, u\right) \\
&\quad = \frac{\partial^2}{\partial\left(\tau_R^l(u)\right)^2}\left(\sum_{i=0}^{N_R-1} A_r^l\left(t,u\right)\cdot\left(\Lambda\left(t-\tau\left(u\right)-\tau_R^l\left(u\right)\right)\right)\right)^2 \\
&\qquad \times\exp\left(j2\left(\phi_r\left(u\right)-\phi_d\left(u\right)\right)\right) \\
&\qquad\quad \times\exp\left(-j\frac{1}{2}\arctan\left(\frac{\mathrm{Imag}\left(\frac{\partial^2}{\partial\left(\tau_R^l(u)\right)^2}\left(R^2\right)\right)}{\mathrm{Real}\left(\frac{\partial^2}{\partial\left(\tau_R^l(u)\right)^2}\left(R^2\right)\right)}\right)\right) \\
&\quad = \frac{\partial^2}{\partial\left(\tau_R^l(u)\right)^2}\left(\sum_{i=0}^{N_R-1} A_r^l\left(t,u\right)\cdot\left(\Lambda\left(t-\tau\left(u\right)-\tau_R^l\left(u\right)\right)\right)\right)^2 \\
&\qquad \times\exp\left(j\left(\phi_r\left(u\right)-\phi_d\left(u\right)\right)\right)
\end{aligned}
\tag{5.9}
$$

Based on the final range compressed signal (5.9), it can be seen that the phase information $\phi_r\left(u\right)-\phi_d\left(u\right)$ is recovered successfully. Then azimuth compression is performed for generating full GNSS-SAR image based on the phase information of the final range compressed signals at different azimuth position $u$, which is expressed as

$$
I_i^p = \int_{u_r=-\frac{N_u}{2}}^{u_r=\frac{N_u}{2}} R_p\left(\tau_R^l, u\right)\cdot R_p^*\left(\tau_R^l, u-u_r\right)du_r \tag{5.10}
$$

where $u_r$ represents azimuth samples for matched filtering. The processing (5.10) is repeated for every azimuth cell.

Overall, the procedure of the proposed range compression algorithm for GNSS-SAR imaging algorithm is summarized as Algorithm 5.1.

As can be seen that in the proposed range compression algorithm in this chapter, when system bi-static angle is fixed, the range resolution is only determined

**Algorithm 5.1** Steps of the proposed range compression algorithm for GNSS-SAR imaging

1: Quadrature demodulating both direct and reflected GNSS signals into base-band and save into both range time domain $t$ and azimuth time domain $u$.
2: Matched filer signal is generated as (2.7).
3: Range compression per azimuth bin is performed as (5.1).
4: Obtaining the squared function of (5.1) per azimuth bin as (5.2).
5: Obtaining the second-order differentiation of (5.2) with respect to range pulse delay $\tau_R^l$ as (5.3).
6: Generating the carrier phase recovery component as (5.8).
7: Multiplying (5.3) with the carrier phase recovery component to obtain the final range compressed signal (5.9).
8: Azimuth compression per azimuth cell is performed as (5.10).
9: Repeat the step 8 for every azimuth cell.
10: Obtaining the final GNSS-SAR image.

by the term

$$\frac{\partial^2}{\left(\partial \tau_R^l(u)\right)^2}\left(\sum_{i=0}^{N_R-1} A_r^l(t,u)\cdot\left(\Lambda\left(t-\tau(u)-\tau_R^l(u)\right)\right)\right)^2,$$

as it is the only function with respect to range delay $\tau_R^l$. According to Fig. 5.1, we can have that by taking the second order differentiation of the summation of PRN code correlation function with different code delay lag, the correlation peaks with merely two lags can be distinguished. This indicates that range resolution of the proposed algorithm can be achieved at the level two range delay samples. For GNSS receiver, the quantity of range delay samples is determined by the sampling frequency, and in order to satisfy the Nyquist criterion [110], the sampling frequency should be at least twice higher than the signal base-band frequency. This indicates that with the proposed range compression algorithm in this chapter, the range resolution can be improved at least twice higher than conventional

range compression algorithm that based on base-band GNSS signals correlation operation only. Taking the standard GPS C/A code signal receiver produced by ip-solution as an example, where the number of samples in each range time domain is 16368, in theoretical, the proposed algorithm can improve range resolution to 36 m, which is significantly higher than the best range resolution level 171 m obtained by conventional range compression algorithm.

## 5.3 The Simulation Study

GNSS-SAR based on GPS C/A code receiver with L1 frequency continues to be employed as an example in this chapter. The same as Chapter 4, the bi-static angle is considered as zero. The rest parameter values of the receiver is the same as TABLE 4.1.

Based on TABLE 4.1, we can have that the number of samples in each range domain is 16368, and the distance between two range samples can be calculated as $c \times \frac{1\text{ms}}{16368} \approx 18$ m. Using parameters from TABLE 4.1, firstly, the simulations of the normalized range compressed signals without background noise for both the conventional range compression algorithm and the proposed range compression algorithm in this chapter are given in Fig. 5.2(a) and Fig. 5.2(b), respectively.

According to Fig. 5.2, it can be seen that using GPS C/A code signal, the range ambiguity of the proposed range compression algorithm can be dramatically reduced to the level 36 m, while it is 171 m for the conventional range compression

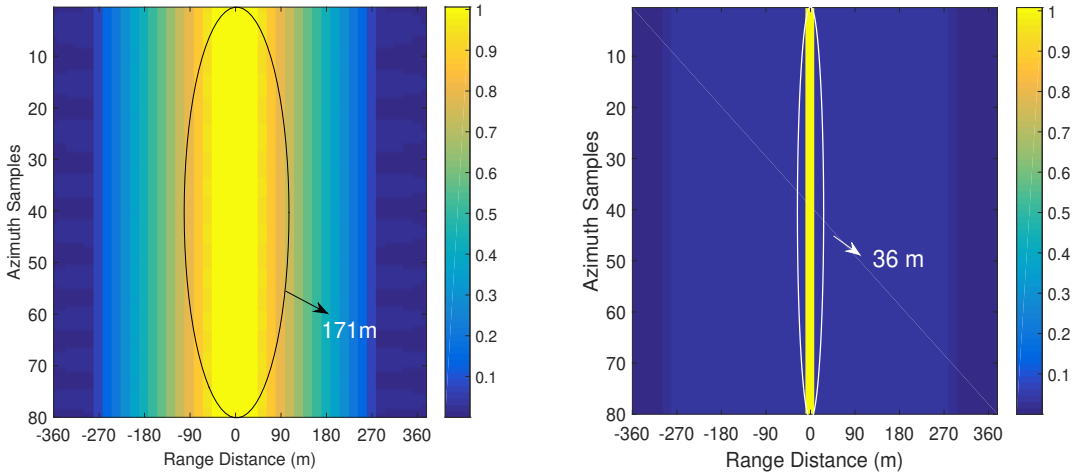


Fig. 5.2: Normalized range compressed signal: (a) The conventional range compression algorithm, (b) The proposed range compression algorithm in Chapter 5 (color scale: pixel intensities sweep from the smallest value to the largest value).

algorithm.

A simulation test is carried out to evaluate the proposed algorithm. Different from chapter 4, the main purpose of this simulation test is to examine whether the proposed range compression algorithm can distinguish the objects with the range position difference 36 m. In addition, the simulation also aims to test the lower bound of range position difference that two objects can be distinguished by conventional range compression approach. On the basis of these respects, within the same azimuth position, we vary the range positions between two different objects. The model for the simulation scenario is illustrated in Fig. 5.3.

In Fig. 5.3, the rotational movement of GNSS-SAR is used for performing an uniform circular motional trace of surveillance antenna to form synthetic aperture for the GNSS-SAR image formation. The duration of the aperture synthetic is

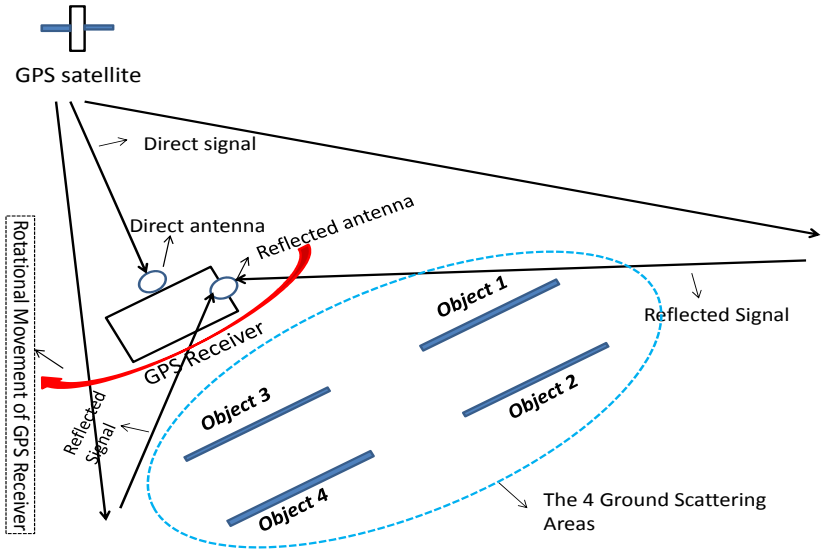


Fig. 5.3: The simulation model of Chapter 5.

2 minutes. In the simulation, the objects 1 to 4, are the four strong scattering areas on the earth, with reflectability of 90%, and no reflections are from the background. The background noise of the simulation is assumed to be addictive white Gaussian noise (AWGN), which value can be calculated using the relevant values in TABLE 4.1 and based on the formula $\sigma = kTB \cdot \left(1 + \frac{T}{290}\right)$ [101]. The objects and GNSS-SAR receiver are assumed with the approximated same horizontal coordinate, where the bi-static angle $\beta$ can be approximated to 0°. For each object, the width of the strip is exactly one range sample length 18 m, and the azimuth duration is 25° angular length. The azimuth gap between the two objects with the same range position is 10° angular length. In this simulation test, we fixed Object 1 and Object 3 at the range position 0 m, but place Object 2 and Object 4 at different range positions as 18 m, 36 m, 216 m and 360 m for forming GNSS-

SAR images respectively to evaluate if the imaging algorithms (both the proposed and the conventional) can separate these objects at range distance domain. The values were chosen on the basis of typical results from the test. The distance between satellite and earth surface in the test is 22200 km. The received direct and reflected signal models at receiver front end for the simulation are generated on the basis of the models (2.4) and (2.5), respectively. Based on the simulation set ups, the results with regard to the both proposed imaging algorithm and the conventional imaging algorithm are illustrated in Fig. 5.4 and Fig. 5.5, respectively. For the ease of comparison, the simulated GNSS-SAR images based on the conventional algorithm is normalized, while the images based on the proposed algorithm is zoomed out by the same level as Fig 5.5.

Based on Fig. 5.4 and Fig. 5.5, it can be seen that within GPS C/A code signal receiver platform, indeed the proposed range compression algorithm in this chapter can clearly separate the objects located at two different range position as close as 36 m, while based on the conventional range compression algorithm, it is hard to separate the objects at two different range position within the distance even at the level 216 m, as the limitation of ranging code with $B = 1.023$ MHz, the theoretical best achievable range resolution is merely 171 m.

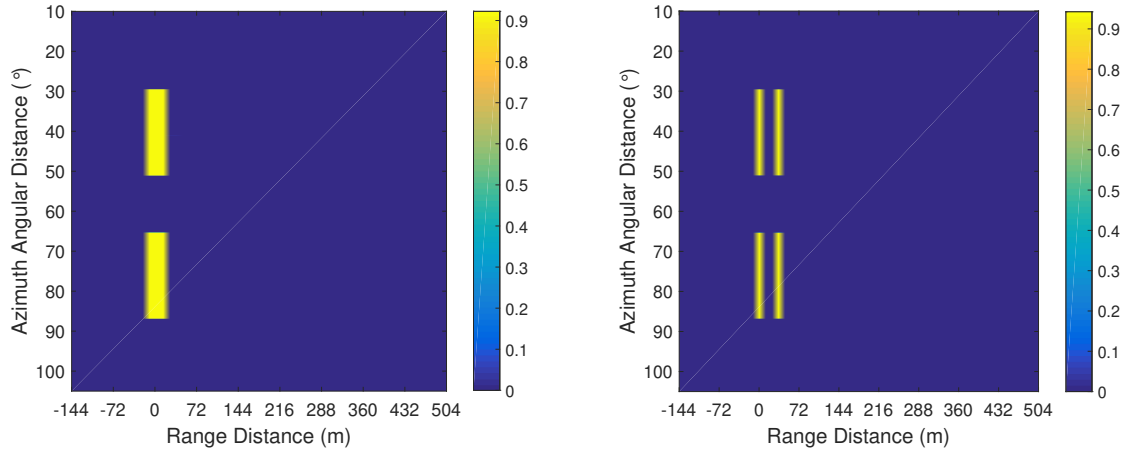


(a) Range distance 18 m

(b) Range distance 36 m

(c) Range distance 72 m

(d) Range distance 162 m

(e) Range distance 216 m

(f) Range distance 360 m

Fig. 5.4: The simulated GNSS-SAR images based on the proposed range compression algorithm in Chapter 5 (color scale: pixel intensities sweep from the smallest value to the largest value).

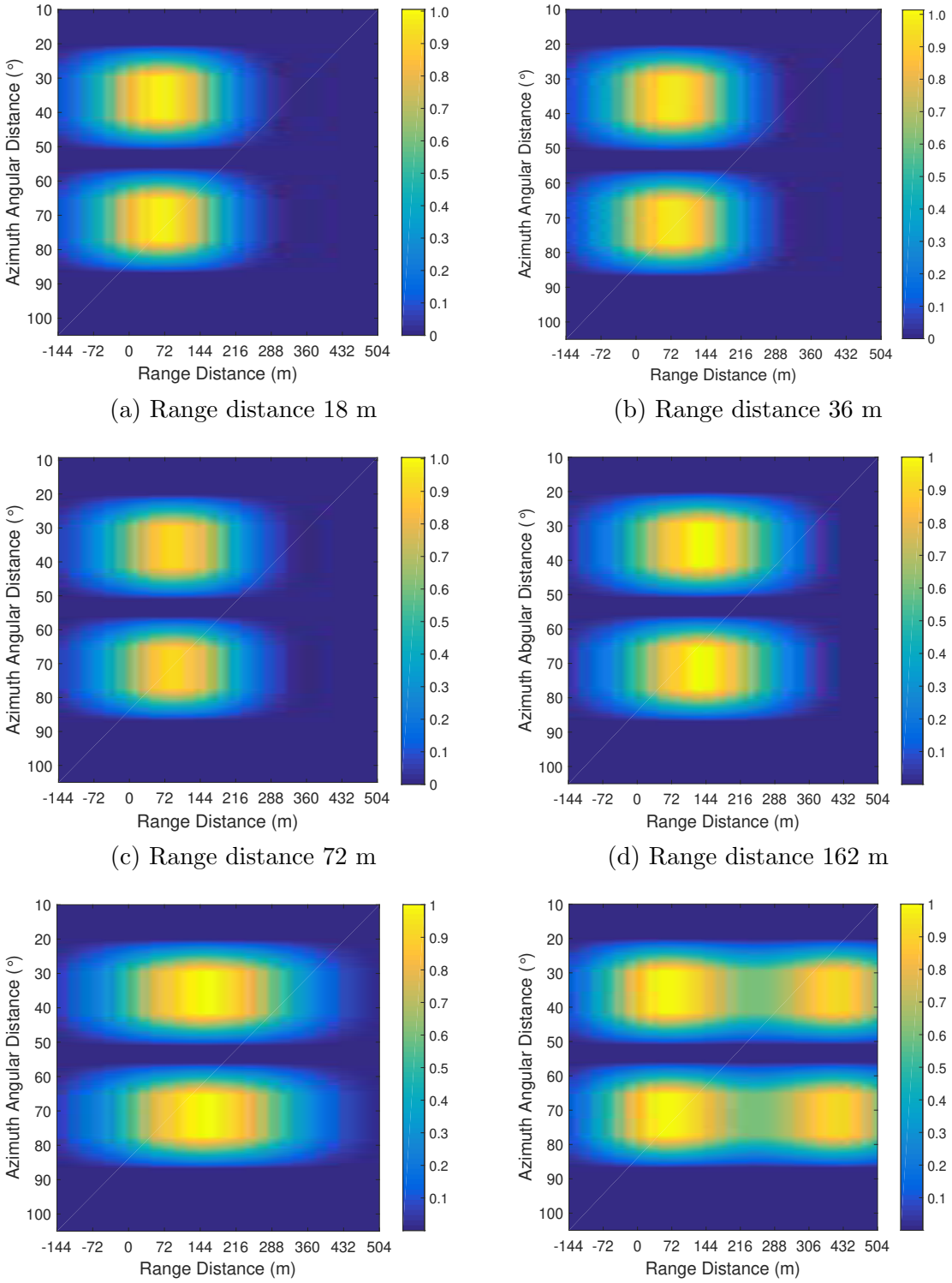


(a) Range distance 18 m

(b) Range distance 36 m

(c) Range distance 72 m

(d) Range distance 162 m

(e) Range distance 216 m

(f) Range distance 360 m

Fig. 5.5: The simulated GNSS-SAR images based on the conventional range compression algorithm (color scale: pixel intensities sweep from the smallest value to the largest value).

## 5.4 Field Experimental Confirmation

To further confirm the effectiveness of the proposed algorithm for the range resolution improvement, an experiment is carried out using a GNSS-SAR system to imaging two objects separated at different locations. The parameters for the GNSS-SAR receiver is the same as TABLE 4.1. The experimental equipment are the same as Fig. 3.3, in which, the geometric positions for direct and surveillance antennas remain the same as Fig. 3.3(a) as well. Circular movement of surveillance antenna is still used for forming synthetic aperture. The data flow for processing the collected signals is the same as Fig. 3.4. The object for the experimental study is the reflection boards (see Fig. 3.5) with a surface area 0.2 $m^2$ and a significantly higher contrast than the background.

On the basis of the experimental equipment and parameter values, the aim of the experiment is to provide a field test to confirm whether the proposed imaging algorithm can distinguish the objects with the range distance difference level less than 171 m by reducing the range compressed ambiguity level, while the best range resolution with the conventional imaging algorithm is only 171 m. The experimental model is the same as Fig. 4.7, while the same field GPS C/A code signal data as Chapter 4 was used. The experimental result with respect to both conventional range compression algorithm and the proposed range compression algorithm in this chapter are illustrated in Fig. 5.6. For the ease of comparison, the same as section 5.3, in Fig. 5.6(a), the images obtained by the conventional

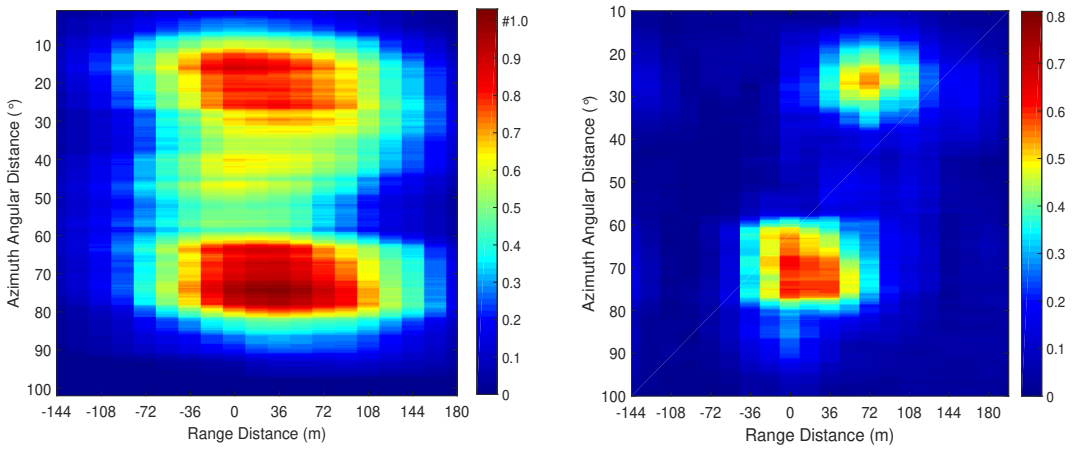


(a) (b)

Fig. 5.6: (a) GNSS-SAR image on the basis of conventional range compression algorithm; (b) GNSS-SAR image on the basis of the proposed range compression algorithm in Chapter 5 (color scale: pixel intensities sweep from the smallest value to the largest value).

algorithm is normalized, while the images obtained by the proposed algorithm (see Fig. 5.6(b)) is zoomed out by the same level as Fig. 5.6(a).

Comparing Fig. 5.6(b) to Fig. 5.6(a), indeed the range position differences for the two objects can be clearly seen based on the proposed algorithm for range compression, and through a coarse measurement on Fig. 5.6(b), the range distance between the centers of the two illuminated regions is indeed around 70 m. However when using the conventional range compression algorithm, it is difficult to identify the range position differences for the two objects, since the theoretical best range resolution is only 171 m on the basis of the employed GNSS receiver in this experiment.

Since the received signals for the SAR receiver using other GNSS satellites as transmission of opportunity have a similar model as the received GPS C/A

code signal, but the higher sampling rate, the proposed algorithm can also be implemented in the other GNSS-SAR systems, where the enhancement level can be higher than using GPS C/A code signal receiver. Using full length Galileo E5 signal receiver as an example, the sampling rate should be more than twice higher than the base-band frequency 51 MHz, thus based on the proposed range compression algorithm in this chapter, theoretically range resolution can be improved to several tenth centimeters level.

In addition, based on the both section 5.3 and section 5.4, it can be seen that the proposed algorithm will cause less degradation of signal magnitude, compared with the algorithm in Chapter 4. Thus it will be more suitable for the application under a longer sensing distance.

## 5.5 Summary

In this chapter, another new GNSS-SAR range compression algorithm is proposed for enhancing resolution, besides Chapter 4. With the proposed algorithm, to extract the correlation peaks for reducing the range ambiguity caused by PRN code, range compressed signal is generated on the basis of Diff2 peak extraction scheme under multi-path environment [105] by second-order differentiation processing of code correlation function. The simulation and experimental results reveal that the proposed imaging algorithm can also provide a significant enhancement with respect to range resolution, compared to the conventional imaging algorithm. To

be more detail, taking a standard GPS C/A code receiver produced by ip-solution with the sampling rate $1.6 \times 10^7$ Hz as an example, the proposed imaging algorithm increases range resolution to 36 m level, while the best range resolution under the conventional imaging algorithm is merely at 171 m level.

This chapter assumes the received SNR is sufficient for obtaining code correlation peak. However under some weak reflected signal condition, the SNR might be very low, and code correlation peak will not be very obvious. Then how to improve range resolution under low SNR scenario remains another interested issue. The comprehensively combing the imaging algorithm in Chapter 3 and the proposed range compression algorithm in this chapter would be helpful for the further investigations.

# Chapter 6

# Applications in Environmental Sensing Using GNSS-SAR

## 6.1 Introduction

In this chapter, we mainly aim to obtain more results by applying GNSS-SAR technique using the comprehensive combinations of the proposed algorithms from chapters 3 to 5, in addition to the current implementations. Accordingly, we will: 1). Analyze the radar sensing range, to test whether longer sensing distance can be handle by GNSS-SAR using the algorithms proposed in previous chapters, compared to the most exampled result in current works that with several hundreds field of vision (FOV); 2). Evaluate GNSS-SAR performance for maritime object sensing with a suppression of ocean background scattering. Working towards these goals, we will firstly derive a theoretical formula to estimate the

operation range of GNSS-SAR with some system parameters i.e. the transmission power, the signal flux density can be received by GNSS radio frequency (RF) front end, etc. A field experiment with a FOV 2 km was carried out for the investigation. The experimental results show that based on GPS L1 receiver, with an omi-directional antenna, the targets can be clearly identified up to 2 km, under urban land environment [62]. At second, under maritime environment, unlike [57, 58, 59], ocean background scattering is considered, we have developed a ship identification scheme to distinguish ship and ocean background scattering on GNSS-SAR images. In the designed scheme, ship presence image identification procedure and ship extraction procedure are carried out based on the properly designed pixel intensity thresholds and region of interests. The procedures are formed into mathematical optimization problems, respectively, and proved to be quasi-convex, so that local optimal values can be found using Lagrange based approach [106]. The effectiveness of the designed scheme is demonstrated by ship identification field results.

The rest of the chapter is structured as follows. The radar sensing distance analysis is illustrated in section 6.2. The implementation of maritime object identification is given in section 6.3. Section 6.4 concludes the chapter.

## 6.2 Analysis of GNSS-SAR Radar Sensing Range

### 6.2.1 Theoretical Operational Distance

We study the theoretical operation distance by examining the reflected power flux density can be received by surveillance antenna. The power flux density of object at surveillance antenna $\rho_{\text{object}}$ can be derived as [23, 101]

$$\rho_{\text{object}} = \frac{P_t \cdot G_t \cdot \sigma_{\text{object}}}{(4\pi)^3 \times R_d^2 \times R_r^2} \tag{6.1}$$

where $P_t$ represents the transmission power of GNSS satellite, $G_t$ represents the gain of GNSS transmission antenna, $\sigma_{\text{object}}$ represents object radar cross section, $R_d$ represents the distance between GNSS satellite and earth surface and $R_r$ represents the distance between the target and GNSS-SAR receiver. In order to let objects being detected on the GNSS-SAR image, the received signal flux density should be larger than threshold $\rho_{\text{T}}$ for imaging processing. The radar cross section of object and background can be expressed as $\sigma_{\text{object}} = \frac{4\pi \cdot A_{\text{eff\_O}}^2}{\lambda^2}$ and $\sigma_{\text{back}} = \frac{4\pi \cdot A_{\text{eff\_B}}^2}{\lambda^2}$, respectively, where $A_{\text{eff\_O}}$ represents the effective reflection area of object and $A_{\text{eff\_B}}$ represents the effective reflection area of background. Based on these, from the expression (6.1), we can have the sensing distance of GNSS-SAR is bounded by the following expression:

$$R_r \leq \sqrt{\frac{P_t \cdot G_t}{(4\pi)^2 \cdot R_d^2 \cdot \rho_{\text{T}} \cdot \lambda^2}} \times A_{\text{eff\_O}}. \tag{6.2}$$

Taking GPS C/A code signal receiver as an example, $P_t \cdot G_t = 50$ w, $R_d = 22200$ km and $\lambda = 0.19$ m, then (6.2) can be specifically expressed as follows

$$R_r \leq 3.47 \times 10^{-8} \times \frac{A_{\text{eff\_O}}}{\sqrt{\rho_{\text{T}}}}. \tag{6.3}$$

From chapter 3, it can be seen that with a false alarm probability less than 0.1, the proposed imaging algorithm can detect the object with a signal strength $-160$ dBm, while it is $-140$ dBm for the conventional imaging algorithm. Thus with the same parameter values as chapter 3, the radar sensing range for the proposed algorithm can be expressed as

$$R_r \leq 109.97 \times A_{\text{eff\_O}}, \tag{6.4}$$

for the conventional imaging algorithm is

$$R_r \leq 10.99 \times A_{\text{eff\_O}}. \tag{6.5}$$

Based on (6.4) and (6.5), it can be seen that the proposed algorithm can provide a significant longer sensing range. The verdict will be verified based on the results from real remote sensing scenario.

### 6.2.2 Experimental Investigations

The purpose of this experiment is to test the sensing range levels that can be achieved by comprehensively combining the proposed algorithms from chapters 3 to 5 in the real application scenario. The experimental parameter values are the same as TABLE 3.1. The experimental equipment is the same as Fig. 3.3. Based on the set up, we compare the performances by comprehensively combining the proposed algorithms from chapters 3 to 5 with the conventional GNSS-SAR imaging algorithm. When combining the proposed algorithms in chapter 3 and chapter 4, in order to have a less degradation in scene illumination level, spectrum equalization is applied after performing accumulating the range compressed signals within the mini-slot $m_s$. Meanwhile the combination of the proposed algorithms in chapter 3 and chapter 5 is carried out in a similar manner, by applying Diff2 scheme to the accumulated range compressed signals within each $m_s$ slot.

Land environmental sensing scenario, which was carried out on the 6/F garden, Block Z, The Hong Kong Polytechnic University, was chosen as a typical application. The optical image for the study is shown in Fig. 6.1.

In Fig. 6.1, it can be seen that there are two main scattering areas, which denoted as 'Targeted Areas 1' and 'Targeted Areas 2', in the field of vision (FOV). In 'Targeted Areas 1', there distributes a tall building and several vegetation, which occupies the approximated range coverage varies from around 200 meter to 500 meter from the location of GPS receiver. 'Targeted Areas 2' are mainly consisted of several tall buildings, which distance from GPS receiver is around 1.8

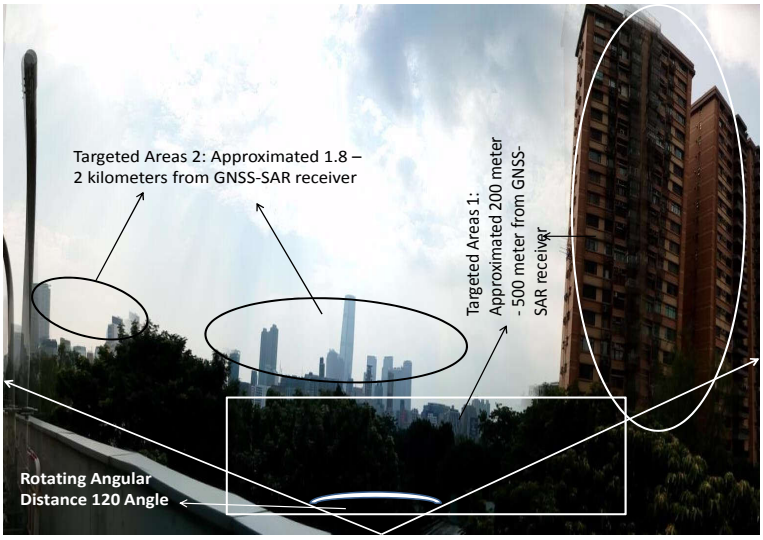


Fig. 6.1: Optical image view of the land experiment.

to 2.0 km. The range distance values of Fig. 6.1 are roughly estimated based on Goggle map, and based on Goggle map, there are no strong scattering areas between 'Targeted Areas 1' and 'Targeted Areas 2'.

Under the land scenario, for reflectability of objects, through the experienced values, the reflective coefficient for vegetation, building with concrete surface are around 5%–10%, while it is around 15% to 20% for the architecture with the glass surface. The real surface size of the targeted areas are around several thousands meters square. Therefore based these, combining the parameter values in TABLE 3.1, formula (6.4) and the signal threshold $\rho_{\mathrm{T}} = -160$ dBm together, we can have that for land sensing scenario, in theoretical, the upper detection distance can reach the level 4 km to 5 km using GNSS-SAR based on the GPS L1 receiver based on the proposed algorithm in chapter 3 with the same parameters. In this remit, all the considered objects in Fig. 6.1 can be identified on the GNSS-

SAR images. However for the conventional imaging algorithm, using the same parameter values in chapter 3, based on (6.5), the sensing range is merely around 500 m. To demonstrate, the results are given in Fig. 6.2, in which, the SAR image generated by the conventional imaging algorithm is normalized (see Fig. 6.2(a)), while the images obtained by the proposed algorithms are zoomed out by the same level as the normalization factor as Fig. 6.2(a).

Fig. 6.2 presents the results originally obtained from imaging algorithms without further image processing. It can be seen that using the proposed imaging algorithm in chapter 3, the noise variance is suppressed, and by combining it with one of the range compression algorithms proposed in chapter 4 and chapter 5, the ambiguities of the illuminated specular points are reduced. The degradation of the illumination level of Fig. 6.2(c) compared to Fig. 6.2(b) and (d) is caused by spectrum equalization. From Fig. 6.2(b) to (d), we can see that the 'Targeted Areas 1' can be clearly identified in the SAR image. The distances from the receiver to the targets obtained from SAR image generally match with the ground truth.

Based on Fig. 6.2, we specifically zoom in the regions at range axis [936m, 2016m] for the investigation. For the ease of comparisons, we choose a scaling factor for pixel intensity based on trial and error tests, and all the zoomed images in Fig. 6.2 are further processed by the same scaling factor for the range region [936m, 2016m]. The results are given in Fig. 6.3.

From Fig. 6.3, we can see that by applying the proposed algorithm in chapter 3

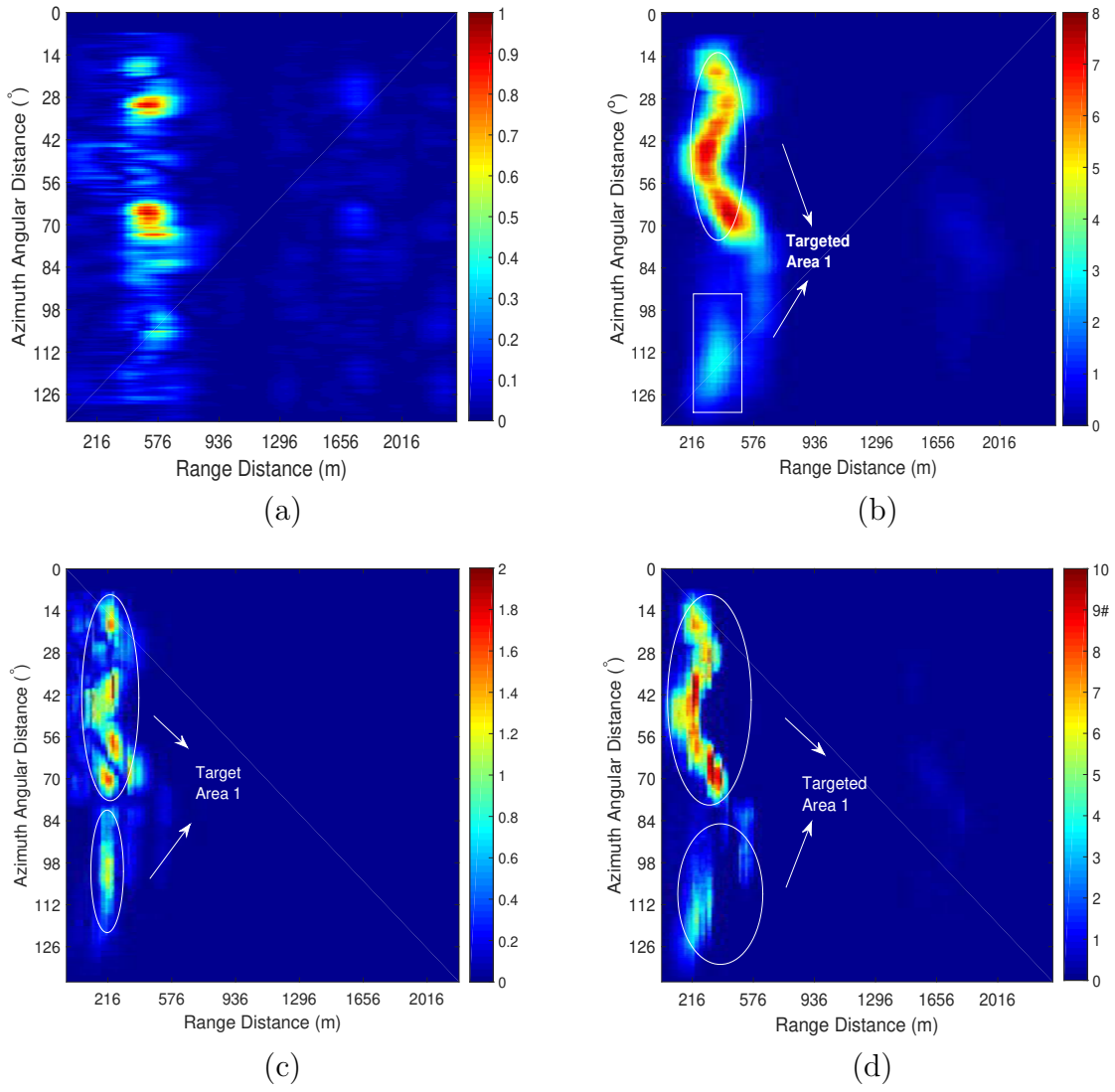


Fig. 6.2: The obtained GNSS-SAR images of the land experimental study: (a). The conventional imaging algorithm; (b). The proposed algorithm in chapter 3; (c). The combination of the proposed algorithms of chapters 3 and 4; (d). The combination of the proposed algorithms of chapter 3 and 5 (color scale: pixel intensities in the images sweep from the smallest value to the largest value).

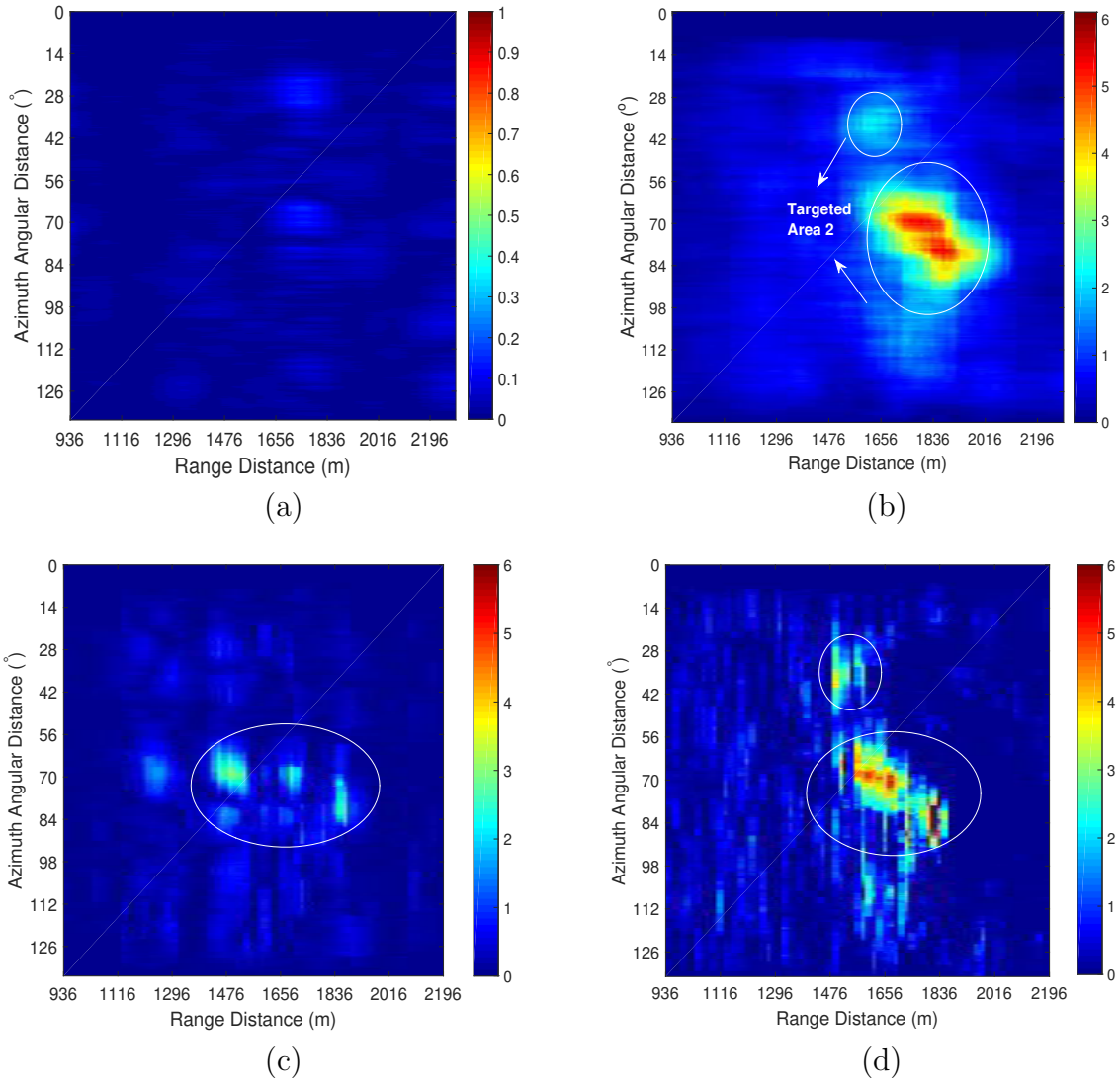


Fig. 6.3: The zoomed GNSS-SAR images at the range region [936m, 2016m] of Fig. 6.2: (a). The conventional imaging algorithm; (b). The proposed algorithm in chapter 3; (c). The combination of the proposed algorithms of chapters 3 and 4; (d). The combination of the proposed algorithms of chapter 3 and 5 (color scale: pixel intensities in the images sweep from the smallest value to the largest value).

in land sensing scenario, the signals from the objects 2 km away from the receiver can indeed be detected on the GNSS-SAR images. The range ambiguity of the specular points in the 'Targeted Area 2' becomes less when chapter 3's algorithm is combined with the proposed range compression algorithm in chapter 4 or chapter 5. The degradation in the scene illumination in Fig. 6.3(c) is because of spectrum equalization.

## 6.3 Maritime Ship Identification Implementations

Since SAR is a promising technique for identifying maritime ships at night, where the visual system might fail to work [72, 73, 74]. With this point, in contrast with many SAR related works [72, 73, 74], this section provides an implementation study with respect to maritime objects identification using passive SAR system using GNSS signals. The comprehensively combined proposed algorithms from chapter 3 to chapter 5 continues to be used for SAR imaging, where the combination is processed in the same manner as aforementioned in section 6.2. Ocean background scattering case is considered in the study, which is different from the works [57, 58, 59]. To improve the visual detectability under ocean background interference, a scheme for maritime ship extraction is designed. The scheme involves two procedures – maritime ship presence image identification and ship extraction. The details are follows.

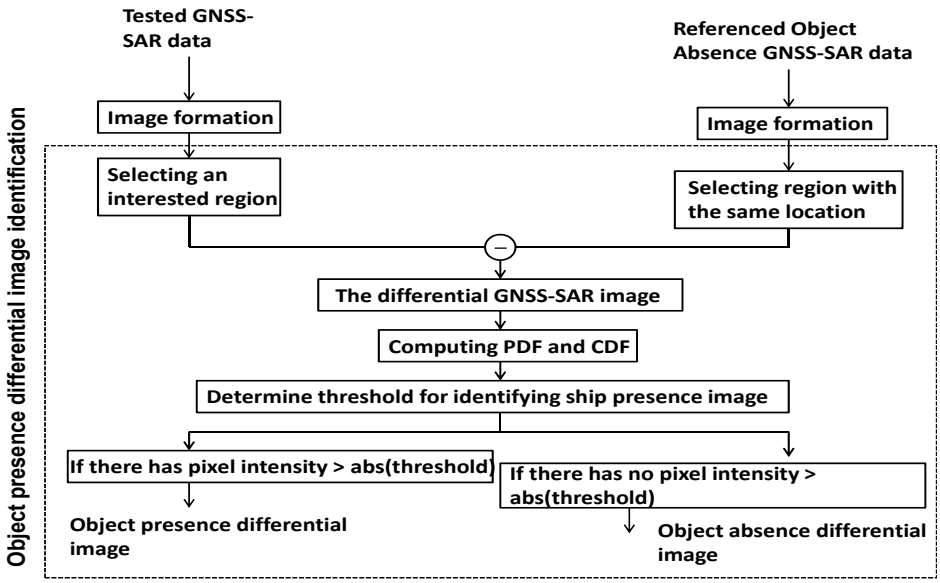


Fig. 6.4: The flow diagram of ship presence differential image identification

### 6.3.1 Maritime Ship Identification Procedure

**Maritime Ship Presence Image Identification:**

For maritime ship presence image identification, we partitioned received long term GNSS-SAR data into different data set for SAR imaging, respectively. In each data set, the first set is used as a reference. The methodology for data set partition is not the concentration in this thesis. The overall view of the designed procedure for each data set is modeled in Fig. 6.4.

For image formation modules in Fig. 6.4, we apply the enhanced imaging algorithm proposed in chapter 3, which will be more benefit for the ship object extraction procedure. With this point, we compare three algorithms, i.e. the proposed algorithm in chapter 3 only, the combined proposed algorithms in chapters 3 and 4, the combined proposed algorithms in chapters 3 and 5.

Thereafter, maritime object identification procedure is carried out as the rest steps in Fig. 6.4. At first, the preliminary region of interests on the tested GNSS-SAR image is selected, while on the referenced GNSS-SAR image, the region with the same size and the same locations as the tested GNSS-SAR image is chosen. The differential GNSS-SAR image is generated based on performing subtraction between tested GNSS-SAR image and referenced GNSS-SAR image within the interested region. The threshold is determined based on probability density function (PDF) and cumulative density function (CDF) of the differential GNSS-SAR image. Assume size of the interested region is $N \times M$, and accumulated number of object pixels is $n \times m$ ($n < N$, $m < M$). Then whether presence of object on the differential GNSS-SAR image can be formulated as a binary hypothesis problem [103] as follows

$$\begin{aligned} H_0: \quad & T = \tfrac{1}{N\times M} \textstyle\sum_{j_\delta=0}^{M-1} \sum_{i_\delta=0}^{N-1} \left[ S_{\text{back}} \left( i_\delta, j_\delta \right) + N \left( i_\delta, j_\delta \right) \right], \\ H_1: \quad & T = \tfrac{1}{N\times M} \Big\{ (n \times m) \cdot \mathrm{E} \left[ S_{\text{object}} \left( i_\delta, j_\delta \right) \right] \\ & \qquad + \left( (N-n) \times (M-m) \right) \cdot \mathrm{E} \left[ S_{\text{back}} \left( i_\delta, j_\delta \right) \right] + \textstyle\sum_{j_\delta=0}^{M-1} \sum_{i_\delta=0}^{N-1} N \left( i_\delta, j_\delta \right) \Big\} \end{aligned} \tag{6.6}$$

where $H_0$ denotes absence of objects, $H_1$ denotes presence of objects, E denotes mathematical expectation within the $N \times M$ region, $i_\delta$ and $j_\delta$ denotes the pixel number at range and azimuth domain, $S_{\text{object}}$ denotes the differential object pixels, $S_{\text{back}}$ denotes the differential background pixels and $N$ denotes background noise, which is assumed to follow Gaussian distribution [104]. Assume within the $N \times M$ region, the mean pixel intensity value of referenced GNSS-SAR image is $\mu_{\text{back}}^1$,

variance is $\sigma_1^2$; the mean pixel intensity value of tested object absence GNSS-SAR image is $\mu_{\text{back}}^k$, variance is $\sigma_k^2$. Because the sample quantity of selected pixels is large enough, according to central limit theory [104], under $H_0$ in (6.6), the false alarm probability of the differential image is derived as follows

$$P_{f_1}(\xi) = Q\left(\frac{\xi - \left(\mu_{\text{back}}^k - \mu_{\text{back}}^1\right)}{\sqrt{\sigma_k^2 - \sigma_1^2}}\right) \tag{6.7}$$

where $\xi$ denotes decision threshold. The decision threshold $\xi$ is an absolute value (denoted as abs$(\cdot)$ in Fig. 6.4) since the reference image can be either ship presence or ship absence. For object presence differential GNSS-SAR image, within the $N \times M$, there exists $n \times m$ ($n < N$, $m < M$) object pixels, then the mean pixel intensity value can be derived as $\frac{m \cdot n}{M \cdot N}\mu_{\text{object}}^k + \frac{(M-m)\cdot(N-n)}{M \cdot N}\mu_{\text{back}}^k$. Then under $H_1$ of (6.6), the detected probability is derived as follows

$$P_{d_1}(\xi) = Q\left(\frac{\xi - \left(\frac{m \cdot n}{M \cdot N}\mu_{\text{object}}^k + \frac{(M-m)\cdot(N-n)}{M \cdot N}\mu_{\text{back}}^k - \mu_{\text{back}}^1\right)}{\sqrt{\sigma_k^2 - \sigma_1^2}}\right). \tag{6.8}$$

Initially to constraint $P_{d_1} > 0.5$ and $P_{f_1} < 0.5$, $\xi$ should follow as

$$\mu_{\text{back}}^k - \mu_{\text{back}}^1 < \xi < \frac{m \cdot n}{M \cdot N}\mu_{\text{object}}^k + \frac{(M-m)\cdot(N-n)}{M \cdot N}\mu_{\text{back}}^k - \mu_{\text{back}}^1. \tag{6.9}$$

To refine the $\xi$ value, the following optimization problem is formulated.

$$\begin{aligned} \max_{\xi} \quad & \pi_1 = P_{d_1}(\xi) + 1 - P_{f_1}(\xi) \\ \text{s.t.} \quad & \mu_{\text{back}}^k - \mu_{\text{back}}^1 < \xi \\ & < \tfrac{m \cdot n}{M \cdot N} \mu_{\text{object}}^k + \tfrac{(M-m)\cdot(N-n)}{M \cdot N} \mu_{\text{back}}^k - \mu_{\text{back}}^1. \end{aligned} \tag{6.10}$$

By investigating the property, we can have that (6.10) is a quasi-convex optimization problem, where the local optimal $\xi$ can be obtained by Lagrange approach [106] (The proof of (6.10) can be seen in Appendix B). Firstly, the Lagrange function with respect to (6.10) can be expressed as

$$\begin{aligned} L(\xi) = \quad & \pi + \lambda_L \left[\xi - \left(\mu_{\text{back}}^k - \mu_{\text{back}}^1\right)\right] \\ & -\mu_L \left[\xi - \tfrac{m \cdot n}{M \cdot N} \mu_{\text{object}}^k + \tfrac{(M-m)\cdot(N-n)}{M \cdot N} \mu_{\text{back}}^k - \mu_{\text{back}}^1\right]. \end{aligned} \tag{6.11}$$

Then, Lagrange approach for finding the local optimal $\xi$ is carried out as follows

$$\begin{cases} \frac{\partial L(\xi)}{\partial \xi} = 0 \\ \lambda_L \left[\xi - \left(\mu_{\text{back}}^k - \mu_{\text{back}}^1\right)\right] = 0 \\ \mu_L \left[\xi - \tfrac{m \cdot n}{M \cdot N} \mu_{\text{object}}^k + \tfrac{(M-m)\cdot(N-n)}{M \cdot N} \mu_{\text{back}}^k - \mu_{\text{back}}^1\right] = 0. \end{cases} \tag{6.12}$$

where $\lambda_L \geq 0$, $\mu_L \geq 0$. Based on the optimal $\xi$ value $\xi^\dagger$, if there exists pixel intensities larger than the threshold, the differential GNSS-SAR image is identified as maritime object presence; otherwise it is absence.

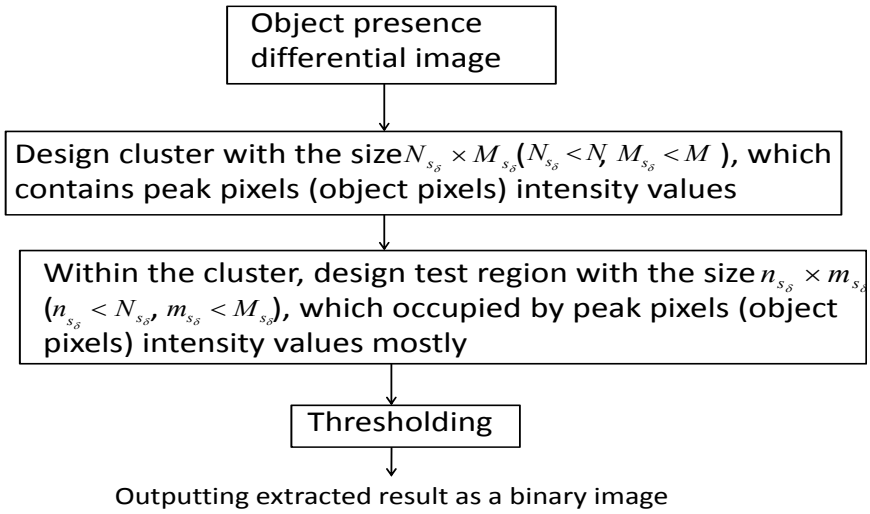


Fig. 6.5: The flow diagram of object pixels extraction

**Maritime Ship Extraction:**

After performing the procedure above, the energy of ocean background scattering is largely suppressed. Because according to dielectric constant, the average scattering capability of maritime ship is higher than the ocean background, based on the identified object presence differential GNSS-SAR image, the pixel intensity with the peak value are contained under maritime ship pixels. Then to extract the ship objects, a refined procedure is carried out, which flow diagram can be seen in Fig. 6.5.

In Fig. 6.5, $N_{s_\delta} < N$, $M_{s_\delta} < M$. We assume that the test region $n_{s_\delta} \times m_{s_\delta}$ ($n_{s_\delta} < N_{s_\delta}$, $m_{s_\delta} < M_{s_\delta}$) is the region within the $N_{s_\delta} \times M_{s_\delta}$ cluster and mainly occupied by object pixels, then the background pixels region is assumed to be $(N_{s_\delta} - n_{s_\delta}) \times (M_{s_\delta} - m_{s_\delta})$. To extract object, another binary hypothesis problem

is formed as

$$\begin{aligned} H_0: \quad T_d &= \frac{1}{\left(N_{s_\delta}-n_{s_\delta}\right)\cdot\left(M_{s_\delta}-m_{s_\delta}\right)} \sum_{j_1=0}^{M_{s_\delta}-m_{s_\delta}-1} \sum_{i_1=0}^{N_{s_\delta}-n_{s_\delta}-1} \left[S_{\text{back}}^{d}\left(i_1,j_1\right)+N^{d}\left(i_1,j_1\right)\right], \\ H_1: \quad T_d &= \frac{1}{n_{s_\delta}\cdot m_{s_\delta}} \sum_{j_2=0}^{m_s-1} \sum_{i_2=0}^{n_{s_\delta}-1} \left[S_{\text{object}}^{d}\left(i_2,j_2\right)+N^{d}\left(i_2,j_2\right)\right]. \end{aligned} \tag{6.13}$$

where $S_{\text{back}}^{d}$ denotes background pixels within the $(N_{s_\delta}-n_{s_\delta})\times(M_{s_\delta}-m_{s_\delta})$ region on the differential image, $S_{\text{object}}^{d}$ denotes object pixels within the $n_{s_\delta}\times m_{s_\delta}$ region on the differential image, $N^d$ denotes background noise on the differential image, $i_1$, $j_1$ denote pixel number at range and azimuth domain within the $(N_{s_\delta}-n_{s_\delta})\times(M_{s_\delta}-m_{s_\delta})$ region, $i_2$, $j_2$ denote pixel number at range and azimuth domain within the $n_{s_\delta}\times m_{s_\delta}$ region. Assume within the $(N_{s_\delta}-n_{s_\delta})\times(M_{s_\delta}-m_{s_\delta})$ region, the mean pixel intensity value is $\mu_{\text{back}}^{d}$ and variance is $\sigma_{d_1}^2$; within the region $n_{s_\delta}\times m_{s_\delta}$, the mean pixel intensity is $\mu_{\text{object}}^{d}$ and variance is $\sigma_{d_2}^2$. Then still based on central limit theory, the false alarm and detection probability with respect to the test region $n_{s_\delta}\times m_{s_\delta}$ and pxiel intensity threshold can be derived as follows

$$P_{f_2}=Q\left(\frac{\epsilon-\mu_{\text{back}}^{d}}{\sigma_{d_1}^2}\right) \tag{6.14}$$

and

$$P_{d_2}=Q\left(\frac{\epsilon-\mu_{\text{object}}^{d}}{\sigma_{d_2}^2}\right) \tag{6.15}$$

where $\epsilon$ is the threshold for extracting object. For the determination of $\epsilon$ value,

similar as the last sub-section, initially $\epsilon$ should satisfy the following constraint:

$$\mu_{\text{back}}^{d} < \epsilon < \mu_{\text{object}}^{d}. \tag{6.16}$$

To refine the $\epsilon$ value and determine the suitable test region size $n_s \times m_s$, similarly another optimization problem is formed as follows.

$$\begin{aligned} \max_{\epsilon, n_{s_\delta} \times m_{s_\delta}} \quad & \pi_2 = P_{d_2}\left(\epsilon, n_{s_\delta} \times m_{s_\delta}\right) + 1 - P_{f_2}\left(\epsilon, n_{s_\delta} \times m_{s_\delta}\right) \\ s.t. \quad & \mu_{\text{back}}^{d} < \epsilon < \mu_{\text{object}}^{d}. \end{aligned} \tag{6.17}$$

By studying the property of (6.17), we can have that the problem is a quasi-convex with $\epsilon$ or $n_{s_\delta} \times m_{s_\delta}$ when one of the parameter is fixed (The proof of quasi-convexity of (6.17) is similar as (6.10)). Then the local optimal $\epsilon$ and suitable $n_{s_\delta} \times m_{s_\delta}$ value can be found using Langrange based iterative method [107].

Finally maritime object extracted result is outputted as a binary image in gray scale.

### 6.3.2 Field Experimental Implementation

Experimental study is carried out in this section based on the scheme in subsection 6.3.1. GPS C/A code signal is selected as source of opportunity to form SAR images as an example. The experimental equipment at GNSS-SAR receiver side are shown in Fig. 3.3. The synthetic aperture is still achieved by the angular trace of the surveillance antenna.

(a)

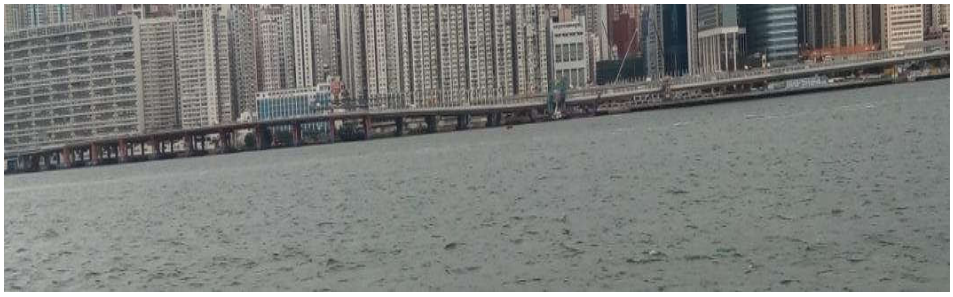

(b)

Fig. 6.6: (a) Ship presence optical image; (b) Ship absence optical image.

The parameter values for the experimental study is given in TABLE 3.1.

The optical image is shown in Fig. 6.6.

In Fig. 6.6(a), we can see that there is no ship. The architectures at the opposite coast are more than 1000 m away from GNSS-SAR receiver, in which, the corresponding interference can be easily eliminated by selecting the appropriate range delay samples for imaging. In Fig. 6.6(b), at the same area as Fig. 6.6(a), there exists three ships with the azimuth length approximately 100 m. From the left to the right hand side, through a coarse measurement by laser rangefinder, the first is approximately 290 m away from GNSS-SAR receiver, the second ship is approximately 320 m from GNSS-SAR receiver and the third ship is approximately 275 m away from GNSS-SAR receiver. The azimuth angular distance for

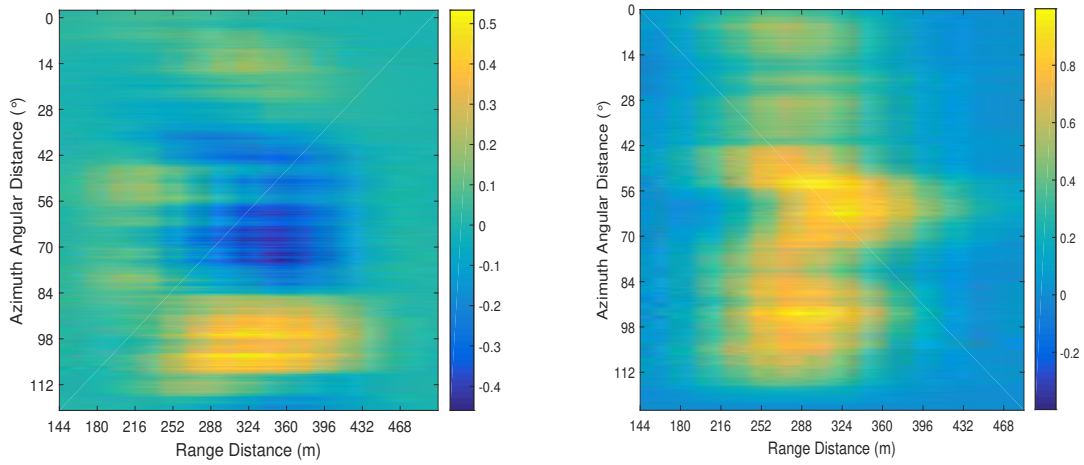


(a) (b)

Fig. 6.7: (a) The differential image based on the data between 15:42 and 15:20; (b) The differential image based on the data between 15:35 and 15:20 (color scale: pixel intensities in the images sweep from the smallest value to the largest value).

performing aperture synthesizing is around 112°. The experimental data were acquired at May 26th, 2017 at Victoria harbor, Hong Kong, in which, the referenced ship absence data was acquired at the time 15:20, the tested ship presence data was acquired at the time 15:35 and the tested ship absence data was acquired at 15:42.

At first, using as one of examples, image formation is based on the proposed algorithm in chapter 3 only. At ship presence image identification stage, the obtained differential GNSS-SAR images based on the data between 15:35 and 15:20, between 15:42 and 15:20 are shown in Fig. 6.7(a) and Fig. 6.7(b), respectively.

Fig. 6.7(a) represents ship absence differential image while Fig. 6.7(b) represents ship presence. In Fig. 6.7(b), we select the illuminated region i.e. 216 m to 360 m at range domain, 0° to 112° at azimuth domain for the investigation,

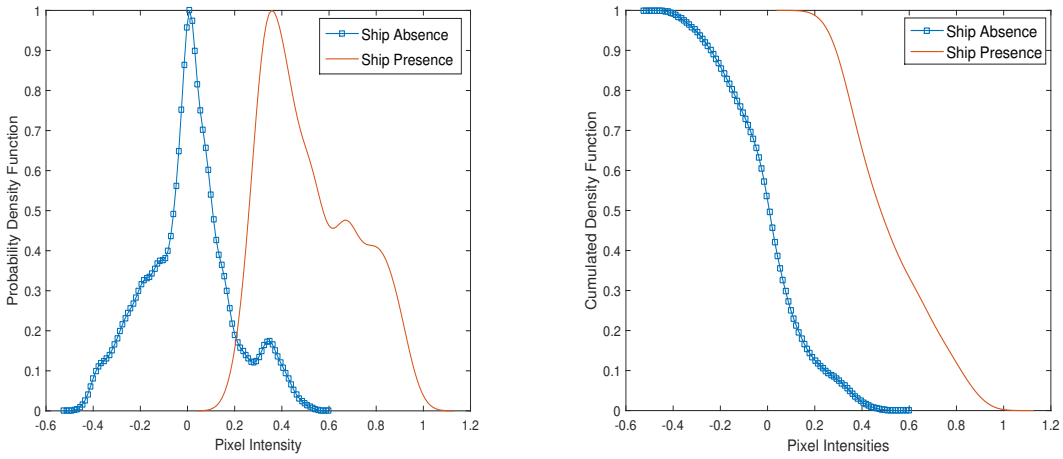


(a) (b)

Fig. 6.8: (a) PDFs of the investigated region on Fig. 6.7(a) and (b); (b) CDFs of the investigated region on Fig. 6.7(a) and (b).

while in Fig. 6.7(a), the same region size with the same location is selected for the comparison. The corresponding PDFs and CDFs are plotted in Fig. 6.8.

In Fig. 6.8(a), it can be seen that when presence of ship objects, the mean value of pixel intensities is obviously higher than absence of ship objects. The reason is that the ship objects has a stronger reflections than ocean background. According to Fig. 6.8, to identify ship presence differential image, we set the normalized threshold value $\xi$ as 0.3, which is the local optimal value obtained based on criterion (6.12). Thereafter, Fig. 6.7(b) has been successfully identified as ship presence differential GNSS-SAR image.

Based on Fig. 6.7(b), ship targets extraction procedure is carried out. The clusters contain three brightest regions pixels are designated. The three clusters size are designated as 150 m range distance $\times$ 15° azimuth angular distance.

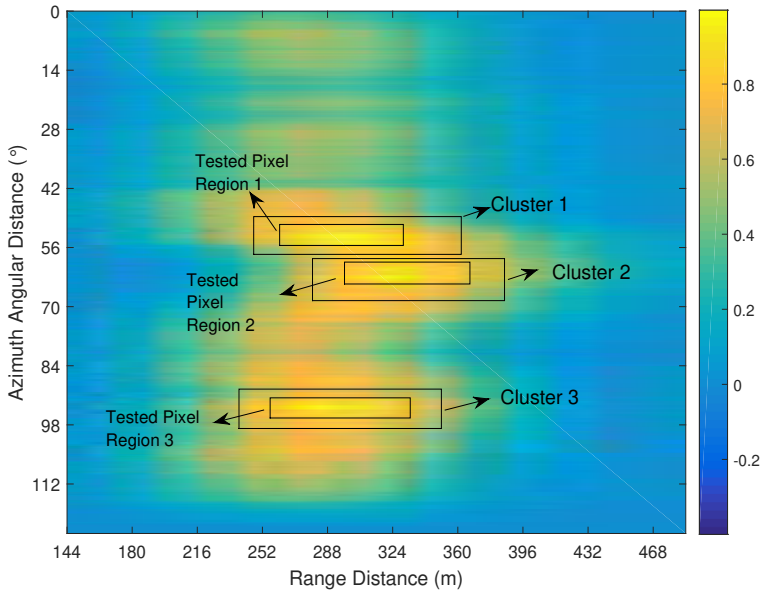


Fig. 6.9: Ship presence differential GNSS-SAR image with the considered regions (color scale: pixel intensities in the images sweep from the smallest value to the largest value).

Within the clusters, the region 100 m range distance $\times$ 5° azimuth angular distance occupied by brightest pixel values is selected as tested pixel region, which assumed occupied by ship pixels. The ship presence differential GNSS-SAR image with respect to the considered clusters and regions is shown in Fig. 6.9.

In Fig. 6.9, from the top to the base side, the corresponding PDFs and CDFs with respect to the considered clusters are shown in Fig. 6.10.

According to Fig. 6.10, to extract ship target, the optimal threshold $\epsilon$ is determined as 0.7, where the detected probability can obtained at the level above 0.9 and false alarm probability can be constrained lower than 0.1. Based on the threshold value $\epsilon = 0.7$, the ship extracted result is outputted as a binary image, which is illustrated as Fig. 6.11.

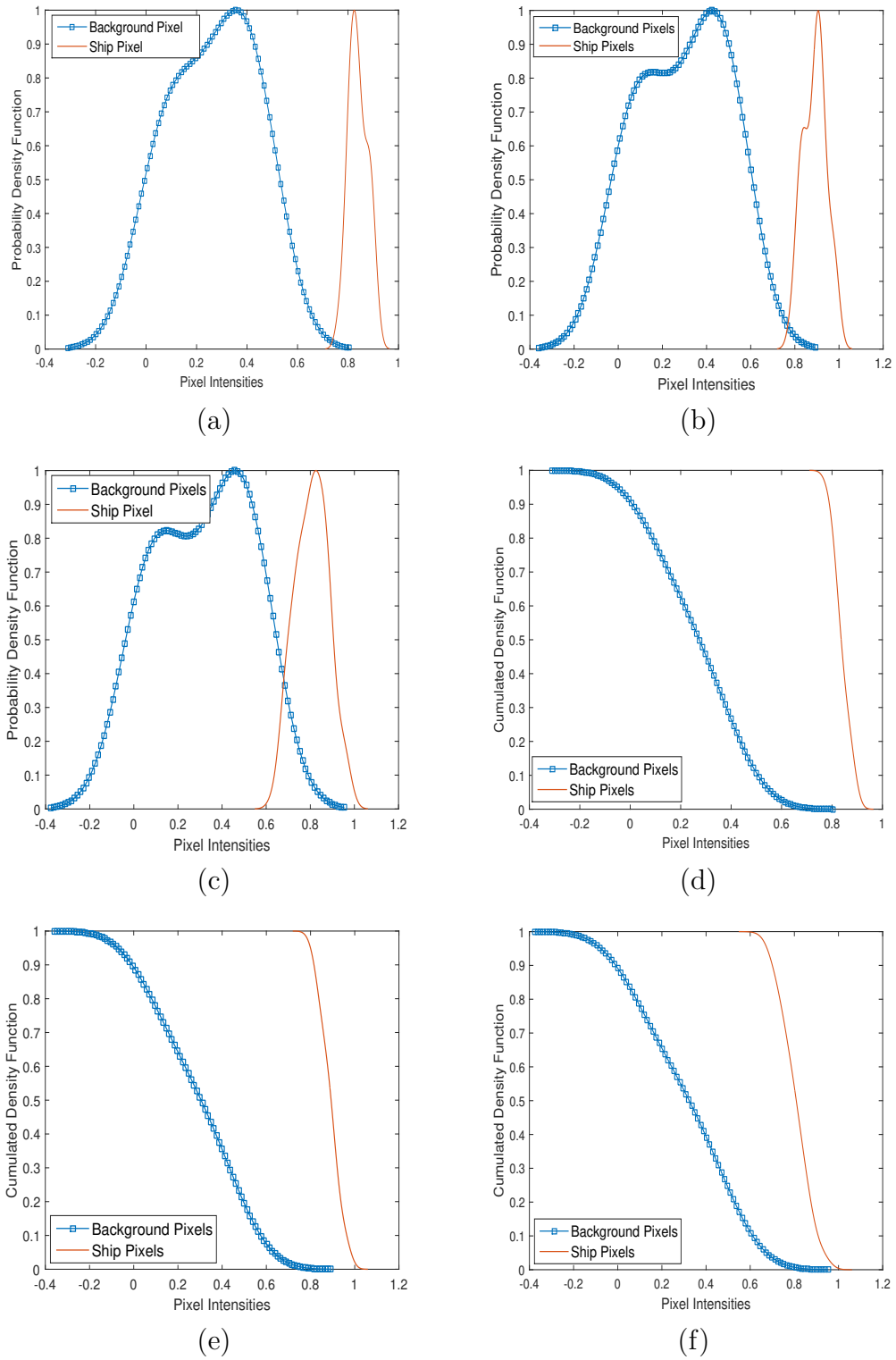


Fig. 6.10: (a). PDFs in cluster 1 of Fig. 6.9; (b). PDFs in cluster 2 of Fig. 6.9; (c). PDFs in cluster 3 of Fig. 6.9; (d). CDFs in cluster 1 of Fig. 6.9; (e). CDFs in cluster 2 of Fig. 6.9; (f). CDFs in cluster 3 of Fig. 6.9.

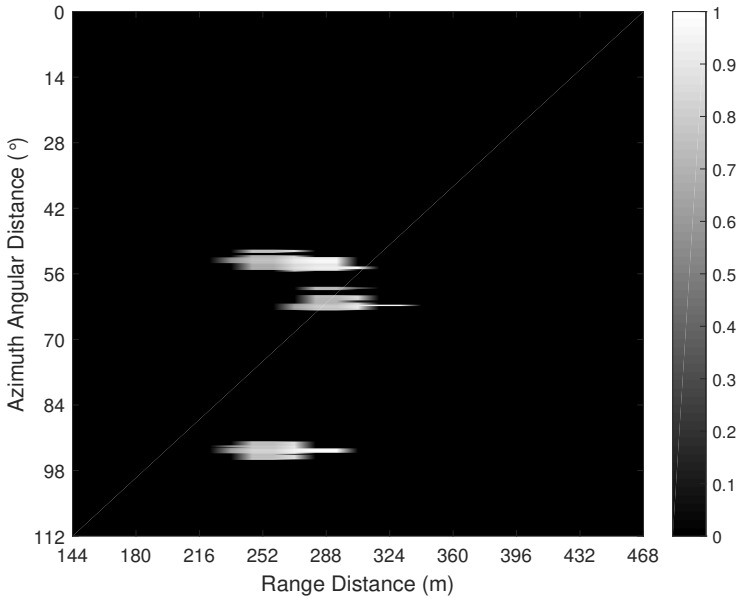


Fig. 6.11: The final ship extracted binary GNSS-SAR image.

As we can see that in Fig. 6.11, the extracted pixels region are clearly illustrated, where the location of scene centers at range domain can be matched with the range distances between GNSS-SAR receiver and ship objects. The range ambiguity in Fig. 6.11 is because of the code correlation property of the signal.

Thereafter, as another examples, to reduce the range ambiguity, the combined proposed algorithms in chapters 3 and 4, chapters 3 and 5 are applied, respectively. The generated GNSS-SAR images are shown in Fig. 6.12, where Fig. 6.12(a) is normalized, and Fig. 6.12(b) is scaled at the same level as the normalization factor of Fig. 6.12(a).

Compared with Fig. 6.12(b), spectrum equalization causes some degradations in scene illumination level in Fig. 6.12(a). On the basis of Fig. 6.12, we run the same ship identification procedure again. The final ship extracted images are

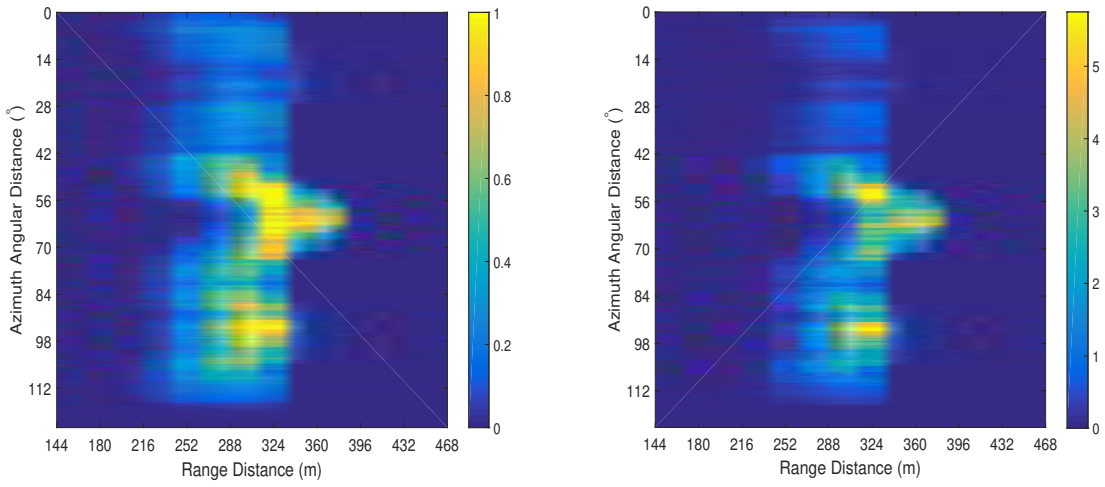


(a) (b)

Fig. 6.12: GNSS-SAR images of ship objects: (a). The combined proposed algorithms in chapters 3 and 4; (b). The combined proposed algorithms in chapters 3 and 5 (color scale: pixel intensities in the images sweep from the smallest value to the largest value).

shown in Fig. 6.13.

Comparison with Fig. 6.11 reveals that range ambiguity is significantly reduced so that the range position differences among each ship become more distinguishable. Therefore the proposed algorithms in chapters 4 and 5 are better for the application in ship identification when combining with the imaging enhancement algorithm in chapter 3.

## 6.4 Summary

In this chapter, firstly, we implement GNSS-SAR technique into urban land sensing scenario by combining the proposed algorithms from chapters 3 to 5 for investigating the radar sensing range for GNSS-SAR. In the experiments, we have

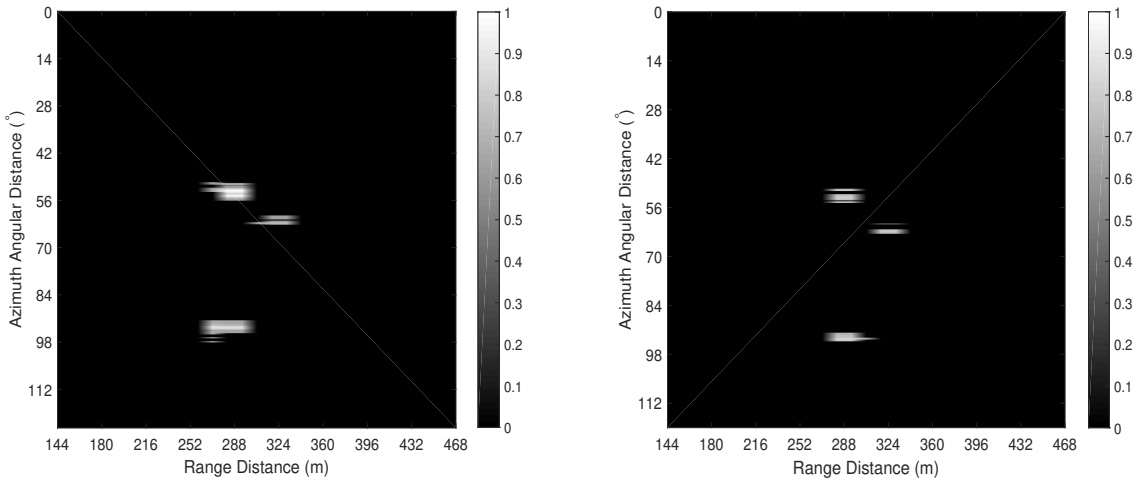


(a) (b)

Fig. 6.13: Ship extracted binary GNSS-SAR images: (a). The combined proposed algorithms in chapters 3 and 4; (b). The combined proposed algorithms in chapters 3 and 5.

demonstrated that signals from the targets at FOV 2 km can be detected on GNSS-SAR images using comprehensively combined the proposed algorithms from chapters 3 to 5, while conventional imaging algorithm with the same parameter values cannot. Secondly, we apply GNSS-SAR technique into maritime ship identification, on the basis of the combined proposed algorithms from chapters 3 to 5 as well. A scheme for extracting maritime ships from ocean background scattering is designed. The implementation results illustrate that GNSS-SAR is also feasible to be used for maritime ship detection under ocean background interference. In summary, the results given in this chapter reveal that compared with conventional imaging algorithm, comprehensively combining the proposed algorithms from chapters 3 to 5 is better for the application of GNSS-SAR.

In the future, we will use air-borne based GNSS-SAR receiver, where a larger

FOV with more objects can be provided for the investigations. A more complicated scenario for object identification will be considered. Meanwhile, we will apply the proposed algorithms in this thesis to the other GNSS receivers i.e. GLONASS signal receiver, Galileo signal receiver and Beidou signal receiver for the performance evaluation.

# Chapter 7

# Conclusions and Future Works

This thesis aims to improve object detection performances for the new remote sensing technique GNSS-SAR system. To achieve this objective, the contributions are summarized in this chapter, and the further developments of this research are presented.

## 7.1 Conclusions

This thesis makes the following progress in the research and development of GNSS-SAR technique:

A new GNSS-SAR imaging algorithm for enhancing objects under weak reflected signals is proposed. In the proposed algorithm, within each pre-determined azimuth resolution cell, multiple non-overlapped mini slots are partitioned. Thereafter, before performing azimuth compression, migration corrected range com-

pressed signals are accumulated within each partitioned mini slots. The results show that with a given detectability, the proposed algorithm can provided an obviously better imaging gain in signal strength than that of the conventional imaging algorithm; under the same weak reflected signal condition, the proposed algorithm can give a significant higher detectability. Based on the experimental instances in chapter 3, the proposed algorithm can still identify the object with reflected signal strength $-160$ dBm, while the conventional imaging algorithm with the same azimuth cell size cannot. Meanwhile, the proposed algorithm is apparently less time consuming than the conventional GNSS-SAR imaging algorithm, where the number of operations is reduced by the level of $10^5$, according to the exampled experimental results in chapter 3.

To deal with low range resolution problem, different from the approaches that using wider bandwidth GNSS base-band signals, we have proposed two new range compression algorithms on the basis of reducing the range compressed ambiguity. One is to use reflected GNSS IF signal for imaging (see Chapter 4), the other is to use Diff2 peak extraction scheme [105] to extract range compressed peaks with different delays (see Chapter 5). In the proposed algorithm in Chapter 4, range compression is performed by correlating reflected GNSS IF signal with direct base-band local replica signal, in which, the main lobe of the compressed pulse is narrowed down significantly. Then spectrum equalization [54, 55] is performed on the compressed result to surpass side-lobes. For the proposed algorithm in Chapter 5, Diff2 scheme is applied to range compressed signals, where the reflected

signals with two range delay samples can be distinguished. In specific, under a standard GPS C/A code receiver platform, the results show that the proposed range compression algorithm in Chapter 4 improves range resolution to 40 m with the IF value 4 MHz, while the proposed range compression algorithm in Chapter 5 provides the range resolution 36 m under the sampling rate $1.6 \times 10^7$ Hz, compared to the 171 m level provided by conventional range compression algorithm. Different from many current GNSS-SAR related research works, the main attractions of chapters 4 and 5 is that the restraint for range resolution improvement with respect to ranging code ambiguity has been addressed.

At the chapter 6, we implement GNSS-SAR in several environmental sensing scenario by investigating the radar sensing distance and maritime ship identification. We have field experimentally demonstrated that using a GPS L1 receiver, we can clearly detect objects at 2 km in the land and sea backgrounds on the GNSS-SAR images. Also, we have shown that GNSS-SAR is capable for maritime ship identifications with presence of ocean background scattering. In conclusion, the results shown in chapter 6 indicate that the comprehensively combined proposed algorithms are better for the environmental sensing, compared to conventional imaging algorithm.

## 7.2 Future Works

Based on the accomplished works, the following general remained issues are meaningful to be considered as future research directions.

All the results in this thesis are obtained through the post-processing manner. However for the application of surveillance system like SAR, real time processing for object detection is very important. Therefore in the future, we are going to develop a field-programmable gate array (FPGA) [111] based signal processing mechanism to process the collected GNSS-SAR data for object detection in real time. Since range compression at different azimuth position and azimuth compression at different range position are independent, parallel computation [112] is a helpful tool for further improving the imaging efficiency.

In terms of the receiver used for GNSS data collections, on one hand, air-borne based receiver will be utilized in the future. A larger FOV with an increased radar cross section area based on the flying height can be provided for the further applications. However the issues that a more complicated scenario and even lower spatial resolution because of the lower signal strength for each scattering point will occur at the same time. How to trade-off the flying height and the received signal strength will be an interested research topics for air-borne based receivers. On the other hand, in the experimental tests in thesis, only GPS C/A code receiver is utilized. In the future, besides GPS C/A code signal receiver, the performance of all the proposed algorithms in this thesis will be evaluated based on the other GNSS

signal receivers i.e. GLONASS receiver, Galileo receiver and Beidou receiver with the respective field data.

Meanwhile, we aim to apply GNSS-SAR technique into various environment sensing or target reconnaissance scenario. On one hand, as aforementioned in chapter 1, it is hard to detect GNSS-SAR receiver as it only receives data. If such technique can be applied for real time object reconnaissance, the concealment will be much better than using traditional active SAR. On the other hand, ocean pollution such as oil slick is a heated discussed environmental topic in recent years. However traditional SAR that transmits L frequency band chirp signal for ocean oil pollutant monitoring has a high expense. As GNSS signals are also transmitted on L frequency band, thus to apply GNSS-SAR for monitoring ocean oil slick would be a very promising future direction, because the technique is more cost effective. And due to the fact that the received signals are integrated, in theoretical, GNSS-SAR should have a higher sensitivity than traditional GNSS-R when performing the respective surveillance.

# Appendix A

# Derivation of (4.9) and (4.10)

## A.1 Derivation of (4.9)

Denoting $\omega_f$ as the frequency range when performing inverse Fourier transform, the derivation of (4.9) can be seen as follows

$$
\begin{aligned}
&\mathcal{F}^{-1}\left\{\mathcal{F}\left[s_{r\_2} \circledast s^{*}_{m\_f}\right] \times W\right\} \\
&\quad = A_r^l \cdot \exp\left(j\left(\phi_r^l(u) - \phi_d(u)\right)\right) \\
&\qquad \times \int_{f_{\mathrm{IF}}-B}^{f_{\mathrm{IF}}+B} \exp\left(j2\pi \cdot \omega_f \cdot \left(t - \tau(u) - \tau_R^l(u)\right)\right) d\omega_f \\
&\quad = \tfrac{1}{2\pi} \cdot A_r^l \cdot \exp\left(j\left(\phi_r^l(u) - \phi_d(u)\right)\right) \times \tfrac{1}{j\left(t-\tau(u)-\tau_R^l(u)\right)} \\
&\qquad \times \left\{\exp\left(j2\pi \cdot (f_{\mathrm{IF}} + B) \cdot \left(t - \tau(u) - \tau_R^l(u)\right)\right)\right. \\
&\qquad\quad \left. - \exp\left(j2\pi \cdot (f_{\mathrm{IF}} - B) \cdot \left(t - \tau(u) - \tau_R^l(u)\right)\right)\right\} \\
&\quad = \tfrac{1}{2\pi} \cdot A_r^l \cdot \exp\left(j\left(\phi_r^l(u) - \phi_d(u)\right)\right) \times \tfrac{1}{j\left(t-\tau(u)-\tau_R^l(u)\right)} \\
&\qquad \times \left\{\cos\left(2\pi \cdot (f_{\mathrm{IF}} + B) \cdot \left(t - \tau(u) - \tau_R^l(u)\right)\right)\right. \\
&\qquad\quad + j \cdot \sin\left(2\pi \cdot (f_{\mathrm{IF}} + B) \cdot \left(t - \tau(u) - \tau_R^l(u)\right)\right) \\
&\qquad\quad - \cos\left(2\pi \cdot (f_{\mathrm{IF}} - B) \cdot \left(t - \tau(u) - \tau_R^l(u)\right)\right) \\
&\qquad\quad\quad \left. - j \cdot \sin\left(2\pi \cdot (f_{\mathrm{IF}} - B) \cdot \left(t - \tau(u) - \tau_R^l(u)\right)\right)\right\}
\end{aligned}
$$

$$
\begin{aligned}
&= \tfrac{1}{2\pi} \cdot A_r^l \cdot \exp\left(j\left(\phi_r^l(u) - \phi_d(u)\right)\right) \times \tfrac{1}{j\cdot\left(t-\tau(u)-\tau_R^l(u)\right)} \\
&\quad \times \left\{2 \cdot \sin\left(2\pi \cdot f_{\mathrm{IF}} \cdot \left(t - \tau(u) - \tau_R^l(u)\right)\right) \cdot \sin\left(-2\pi \cdot B \cdot \left(t - \tau(u) - \tau_R^l(u)\right)\right)\right. \\
&\quad\quad + j \cdot \sin\left(2\pi \cdot (f_{\mathrm{IF}} + B) \cdot \left(t - \tau(u) - \tau_R^l(u)\right)\right) \\
&\quad\quad\quad \left. + j \cdot \sin\left(2\pi \cdot (B - f_{\mathrm{IF}}) \cdot \left(t - \tau(u) - \tau_R^l(u)\right)\right)\right\}
\end{aligned}
\tag{A-1}
$$

Here completes the derivation of (4.9).

## A.2 Derivation of (4.10)

After filtering the frequency components lower than $f_{\mathrm{IF}} + B$, (4.9) can be transformed into the following:

$$
\begin{aligned}
&R_{c\_\mathrm{proposed}} \\
&\quad = \tfrac{1}{2\pi} \cdot A_r^l \cdot \exp\left(j\left(\phi_r^l(u) - \phi_d(u)\right)\right) \times \tfrac{1}{j\left(t-\tau(u)-\tau_R^l(u)\right)} \\
&\quad\quad \times j \cdot \sin\left(2\pi \cdot (f_{\mathrm{IF}} + B) \cdot \left(t - \tau(u) - \tau_R^l(u)\right)\right) \\
&\quad = A_r^l \cdot \exp\left(j\left(\phi_r^l(u) - \phi_d(u)\right)\right) \times (f_{\mathrm{IF}} + B) \\
&\quad\quad \times \mathrm{sinc}\left(2\pi \cdot (f_{\mathrm{IF}} + B) \cdot \left(t - \tau(u) - \tau_R^l(u)\right)\right).
\end{aligned}
\tag{A-2}
$$

The right hand side of the second equation of (A-2) is exactly (4.10)).

Here completes the derivation of (4.10).

# Appendix B

# Proof of Quasi-convexity of the problem (6.10)

The proof is based on examining second order differentiation of the objective function $\pi$. The second order differentiation of $\pi$ is shown as follows

$$\begin{aligned}\frac{\partial^2 \pi_1}{\partial \xi^2} = & \frac{1}{\sqrt{2\pi \cdot \left(\sigma_k^2 - \sigma_1^2\right)}} \times \left\{ \exp\left( -\frac{1}{2} \left( \frac{\xi - \left( \frac{m \cdot n}{M \cdot N} \mu_{\text{object}}^k + \frac{(M-m)\cdot(N-n)}{M \cdot N} \mu_{\text{back}}^k - \mu_{\text{back}}^1 \right)}{\sqrt{\sigma_k^2 - \sigma_1^2}} \right)^2 \right) \right. \\ & \times \left( \frac{\xi - \left( \frac{m \cdot n}{M \cdot N} \mu_{\text{object}}^k + \frac{(M-m)\cdot(N-n)}{M \cdot N} \mu_{\text{back}}^k - \mu_{\text{back}}^1 \right)}{\sqrt{\sigma_k^2 - \sigma_1^2}} \right) \\ & \left. - \exp\left( -\frac{1}{2} \left( \frac{\xi - \left( \mu_{\text{back}}^k - \mu_{\text{back}}^1 \right)}{\sqrt{\sigma_k^2 - \sigma_1^2}} \right)^2 \right) \times \left( \frac{\xi - \left( \mu_{\text{back}}^k - \mu_{\text{back}}^1 \right)}{\sqrt{\sigma_k^2 - \sigma_1^2}} \right) \right\}. \end{aligned} \tag{B-1}$$

Because of the constraint (6.9), we can have that (B-1) is no larger than zero. Thus the objective function satisfies convex optimization criterion. And because the constraint in (6.10) is an open interval, according to the definition in [106], we can have that the problem (6.10) is quasi-convex.

Here completes the proof.

# References


[1] J. C. Curlander and R. N. McDonough, *Synthetic aperture radar*, New York, NY, USA: John Wiley & Sons, 1991.

[2] W. M. Brown, 'Synthetic aperture radar', *IEEE Transactions on Aerospace and Electronic Systems*, No. 2, pp. 217–229, 1967.

[3] J. P. Fitch, *Synthetic aperture radar*, Springer Science & Business Media, 2012.

[4] G. Franceschetti and R. Lanari, *Synthetic aperture radar processing*, CRC press, 1999.

[5] I. G. Cumming and F.H. Wong, *Digital processing of Synthetic Aperture Radar data*. 2005: Artech House.

[6] M. Cherniakov, editor, *Bistatic radars: Emerging technology*, John Wiley & Sons, 2008.

[7] R. Saini and M. Cherniakov, 'DTV signal ambiguity function analysis

for radar application', *IEE Proceedings In Radar, Sonar and Navigation*, Vol. 152, No. 3, pp. 133–142, 2005.

[8] D. Poullin, M. Flecheus and M. Klein, 'New capabilities for PCL system: 3D measurement for receiver in multidonors configuration', *in 2010 European Radar Conference*, 2010, pp. 344–347.

[9] R. Cardinali, F. Colone, P. Lombardo, O. Crognale, A. Cosmi and A. Lauri, 'Multipath cancellation on reference antenna for passive radar which exploits FM transmission', *IET International Conference on InRadar Systems*, pp. 1–5, 2007.

[10] M. Cherniakov, D. Nezlin and K. Kubik, 'Air target detection via bistatic radar based on LEOS communication signals', *IEE Proceedings-Radar, Sonar and Navigation*, Vol. 149, No. 1, pp. 33–38, 2002.

[11] H. D. Griffiths, C. J. Baker, J. Baubert, N. Kitchen and M. Treagust, 'Bistatic radar using satellite-borne illuminators', *IET InRADAR*, pp. 1–5, 2002.

[12] B. Mojarrabi, J. Homer, K. Kubik, I. D. Longstaff, 'Power budget study for passive target detection and imaging using secondary applications of GPS signals in bistatic radar systems', *2002 IEEE International InGeoscience and Remote Sensing Symposium*, Vol. 1, pp. 449–451, 2002.

[13] D. K. Tan, H. Sun, Y. Lu, M. Lesturgie and H. L. Chan, 'Passive radar using

global system for mobile communication signal: theory, implementation and measurements', *IEE Proceedings- InRadar, Sonar and Navigation*, Vol. 152, No. 3, pp. 116–123, 2005.

[14] P. Misra and P. Enge, *Global Positioning System: Signals, Measurements and Performance*, Second Edition, Lincoln, MA: Ganga-Jamuna Press, 2006.

[15] M. Martin-Neira M, 'A passive reflectometry and interferometry system (PARIS): Application to ocean altimetry', *ESA journal*, Vol. 17, No. 4, pp. 331–355, 1993.

[16] N. G. Ruffini, F. Soulat, M. Caparrini, O. Germain and M. MartnNeira, 'The Eddy Experiment: Accurate GNSSR ocean altimetry from low altitude aircraft', *Geophysical research letters*, Vol. 31, No. 12, 2004.

[17] P. Ferrazzoli, L. Guerriero, N. Pierdicca and R. Rahmoune, 'Forest biomass monitoring with GNSS-R: Theoretical simulations', *Advances in Space Research*, Vol. 47, No. 10, pp. 1823–1832, 2011.

[18] A. Egido, G. Ruffini, M. Caparrini, C. Martin, E. Farres and X. Banque, 'Soil moisture monitorization using GNSS reflected signals', *arXiv preprint arXiv:0805.1881*, 2008 May 13.

[19] M. D. Jacobson, 'Dielectric-covered ground reflectors in GPS multi-path receptionTheory and measurement', *IEEE Geoscience and Remote Sensing Letters*, Vol. 5, No. 3, 396–399, 2008.

[20] B. Hofmann-Wellenhof, H. Lichtenegger and E. Wasle, *GNSSglobal navigation satellite systems: GPS, GLONASS, Galileo, and more*, Springer Science & Business Media, 2007.

[21] I. Z. Nesreen, GNSS receivers for weak signals, Artech House Publishers, 2006.

[22] G. R. Nudd and O. W. Otto, 'Chirp signal processing using acoustic surface wave filters', *IEEE In1975 Ultrasonics Symposium*, pp. 350–354, 1975.

[23] Z. Zeng, 'Passive bistatic SAR with GNSS transmitter and a stationary receiver', PhD Thesis, University of Birmingham, 2013.

[24] K. Borre, D. M. Akos, N. Bertelsen, et al, *A software-defined GPS and Galileo receiver: a single-frequency approach*, Springer Science & Business Media, 2007.

[25] E. Kaplan and C. Hegarty, editors, *Understanding GPS: principles and applications*, Artech house; 2005.

[26] Glonass IC. GLONASS ICD. Russian Space Agency, Version. 2002, No. 5, 2002.

[27] R. Wu, W. Wang, D. Lu, L. Wang and Q. Jia, 'Principles of Satellite Navigation System', *InAdaptive Interference Mitigation in GNSS 2018*, Singapore, pp. 1–29.

[28] https://www.glonass-iac.ru/en/guide/beidou.php (Accessed on June 12th, 2018).

[29] T. Lindgren and D. M. Akos, 'A multistatic GNSS synthetic aperture radar for surface characterization', *IEEE Transactions on Geoscience and Remote Sensing*, Vol. 46, No. 8, pp. 2249–2253, 2008.

[30] M. Antoniou, M. Cherniakov and C. Hu, 'Space-surface bistatic SAR image formation algorithms', *IEEE Transactions on Geoscience and Remote Sensing*, Vol. 47, No. 6, pp. 1827–1843, 2009.

[31] R. Zuo, 'Bistatic synthetic aperture radar using GNSS as transmitters of opportunity', PhD Thesis, University of Birmingham, 2012.

[32] M. Antoniou, Z. Zeng, L. Feifeng and M. Cherniakov, 'Experimental demonstration of passive BSAR imaging using navigation satellites and a fixed receiver', *IEEE Geoscience and Remote Sensing Letters*, Vol. 3, No. 9, pp. 477–481, 2012.

[33] M. Antoniou and M. Cherniakov, 'GNSS-based bistatic SAR: a signal processing view', *EURASIP Journal on Advances in Signal Processing*, 2013(1), pp. 1–16, 2013.

[34] R. Saini, R. Zuo and M. Cherniakov, 'Problem of signal synchronisation in space-surface bistatic synthetic aperture radar based on global navigation

satellite emissions-experimental results', *IET radar, sonar & navigation*, Vol. 4, No. 1, pp. 110–125, 2010.

[35] M. Antoniou, Z. Hong, Z. Zhangfan, R. Zuo, Q. Zhang and M. Cherniakov, 'Passive bistatic synthetic aperture radar imaging with Galileo transmitters and a moving receiver: experimental demonstration', *IET Radar, Sonar & Navigation*, Vol. 7, No. 9, pp. 985–993, 2013.

[36] T. Ebinuma, Y. Mikawa and S. Nakasuka, 'Quasi-monostatic algorithm for GNSS-SAR', *IEEE 2013 Asia-Pacific Conference on InSynthetic Aperture Radar (APSAR)*, pp. 164–166, 2013.

[37] W. Tian, Z. Tao and H. Cheng, 'Imaging algorithm for bistatic SAR based on GNSS signal', *Journal of Radars*, Vol. 2, No. 1, pp. 39–45, 2013.

[38] F. Liu, M. Antoniou, Z. Zeng and M. Cherniakov, 'Point spread function analysis for BSAR with GNSS transmitters and long dwell times: theory and experimental confirmation', *IEEE Geoscience and Remote Sensing Letters*, Vol. 10, No. 4, pp. 781–785, 2013.

[39] W. Tian, T. Zhang, T. Zeng, C. Hu and T. Long, 'Space-surface BiSAR based on GNSS signal: Synchronization, imaging and experiment result', *2014 IEEE InRadar Conference*, pp. 512–516, 2014.

[40] T. Zeng, D. Ao, C. Hu, T. Zhang, F. Liu, W. Tian and K. Lin, 'Multi-angle BSAR Imaging Based on BeiDou-2 Navigation Satellite System: Ex-

periments and Preliminary Results', *IEEE Transactions on Geoscience and Remote Sensing*, Vol. 53, No. 10, pp. 5760-5773, 2015.

[41] T. Zeng, T. Zhang, W. Tian, C. Hu and X. Yang, 'Bistatic SAR imaging processing and experiment results using BeiDou-2/Compass-2 as illuminator of opportunity and a fixed receiver', *2015 IEEE 5th Asia-Pacific Conference on In Synthetic Aperture Radar (APSAR)*, pp. 302–305, 2015.

[42] F. Santi, M. Antoniou and D. Pastina, 'Point spread function analysis for GNSS-based multistatic SAR' *IEEE Geoscience and Remote Sensing Letters*, Vol. 12, No. 2, pp. 304–308, 2015.

[43] H. C. Zeng, P. B. Wang, J. Chen, W. Liu, L. Ge and W. Yang, 'A Novel General Imaging Formation Algorithm for GNSS-Based Bistatic SAR', *Sensors*, Vol. 16, No. 3, pp. 1–15, 2016.

[44] T. Zeng, T. Zhang, W. Tian and C. Hu, 'Space-Surface Bistatic SAR image enhancement based on repeat-pass coherent fusion with Beidou-2/Compass-2 as illuminators', *IEEE Geoscience and Remote Sensing Letters*, Vol. 13, No. 12, pp. 1832–1836, 2016.

[45] G. Turin, 'An introduction to matched filters', *IRE transactions on Information theory*, Vol. 3, No. 6, pp. 311–329, 1960.

[46] M. Antoniou, F. Liu, Z. Zeng, V. Sizov, and M. Cherniakov, 'Coherent

change detection using GNSS-based passive SAR: first experimental results', *IET International Conference on In Radar Systems* , pp. 1–5, 2012.

[47] F. Liu, M. Antoniou, Z. Zeng, and M. Cherniakov, 'Coherent change detection using passive GNSS-based BSAR: experimental proof of concept', *IEEE Transactions on Geoscience and Remote Sensing*, Vol. 51, No. 8, pp. 4544–4555, 2013.

[48] Q. Zhang, M. Antoniou, W. Chang, and M. Cherniakov, 'Spatial decorrelation in GNSS-based SAR coherent change detection', *IEEE Transactions on Geoscience and Remote Sensing*, Vol. 53, No. 1, pp. 219–228, 2015.

[49] Z. Zhangfan, M. Antoniou, L. Feifeng and M. Cherniakov, 'First space surface bistatic fixed receiver SAR images with a navigation satellite', *12th International Radar Symposium (IRS)*, 2011.

[50] A. Lazarov, V. C. Chen, T. Kostadinov and J. Passos Morgado, 'Bistatic SAR system with GPS transmitter', *IEEE InRadar Conference (RADAR)*, pp. 1–6, 2013.

[51] J. Zhen, Z. Zhang and S. Wu, 'A GPS signal based numeric range migration algorithm of space-surface bistatic SAR', *2009 IEEE International In Geoscience and Remote Sensing Symposium*, Vol. 2, pp. 49–52, 2009.

[52] J. Zhen, Z. Zhang, S. Wu and G. Huang, 'GNSS illuminator based high range resolution algorithm in space-surface bistatic SAR', *IEEE Interna-*

*tional In Geoscience and Remote Sensing Symposium (IGARSS)*, pp. 4608–4611, 2010.

[53] F. Santi, D. Pastina, M. Bucciarelli, M. Antoniou, D. Tzagkas and M. Cherniakov, 'Passive multistatic SAR with GNSS transmitters: preliminary experimental study', *IEEE 11th InEuropean Radar Conference (EuRAD)*, pp. 129–132, 2014.

[54] H. Ma, M. Antoniou and M. Cherniakov, 'Passive GNSS-based SAR imaging and opportunities using Galileo E5 signals', *Science China Information Sciences*, Vol. 58, No. 6, pp. 1–11, 2015.

[55] H. Ma, M. Antoniou and M. Cherniakov, 'Passive GNSS-Based SAR Resolution Improvement Using Joint Galileo E5 Signals', *IEEE Geoscience and Remote Sensing Letter*, Vol. 12, No. 8, pp. 1640–1644, 2015.

[56] F. Santi, M. Bucciarelli, D. Pastina, M. Antoniou and M. Cherniakov, 'Spatial resolution improvement in GNSS-Based SAR using multistatic acquisitions and feature extraction', *IEEE Transactions on Geo-science and Remote Sensing*, Vol. 54, No. 10, pp. 6217–6231, 2016.

[57] F. Santi, D. Pastina and M. Bucciarelli, 'Maritime moving target detection technique for passive bistatic radar with GNSS transmitters' *2017 18th IEEE International InRadar Symposium (IRS)*, pp. 1–10, 2017.

[58] H. Ma, M. Antoniou, D. Pastina, F. Santi, F. Pieralice, M. Bucciarelli and

M. Cherniakov, 'Maritime Moving Target Indication Using Passive GNSS-based Bistatic Radar', *IEEE Transactions on Aerospace and Electronic Systems*, 2017, DOI: 10.1109/TAES.2017.2739900.

[59] H. Ma, M. Antoniou, M. Cherniakov, D. Pastina, F. Santi, F. Pieralice and M. Bucciarelli, 'Maritime target detection using GNSS-based radar: Experimental proof of concept', *2017 IEEE InRadar Conference (RadarConf)*, pp. 464–469, 2017.

[60] Y. Zheng, Y. Yang and W. Chen, 'Enhanced GNSS-SAR Range-Doppler Algorithm for The Target Detection of Weak Reflected Signals: An Experimental Study', *Journal of Aeronautics, Astronautics and Aviation, Series A*, Vol. 49, No. 2, pp. 83–92, 2017.

[61] N. Metropolis, 'Monte Carlo Method', *From Cardinals to Chaos: Reflection on the Life and Legacy of Stanislaw Ulam*, p. 125, 1989.

[62] Y. Zheng, Y. Yang and W. Chen, 'Analysis of Radar Sensing Coverage of a Passive GNSS-Based SAR System', *2017 IEEE International Conference on Localization and GNSS (ICL-GNSS 2017)*, Nottingham, UK, June 2017.

[63] Y. Zheng, Y. Yang and W. Chen, 'A Novel Range Compression Algorithm for Resolution Enhancement in GNSS-SARs', *Sensors*, Vol. 17, No. 7, pp. 1496, 2017.

[64] Y. Zheng, Y. Yang and W. Chen, 'An New Imaging Algorithm for Passive

GNSS-Based SAR under Weak Reflected Signals', *Radio Science* (Under Review).

[65] Y. Zheng, Y. Yang and W. Chen, 'A New Imaging Algorithm for Range Resolution Improvement in Passive GNSS-based SAR', *IET Radar Sonar & Navigation* (Under Review).

[66] F. Maussang, F. Daout, G. Ginolhac and F. Schmitt, 'GPS ISAR passive system characterization using point spread function', *IEEE In New Trends for Environmental Monitoring Using Passive Systems*, pp. 1–4, 2008.

[67] F. Daout, F. Schmitt, G. Ginolhac and P. Fargette, 'Multistatic and multiple frequency imaging resolution analysis-application to gps-based multistatic radar', *IEEE Transactions on Aerospace and Electronic Systems*, Vol. 48, No. 4, pp. 3042–3057, 2012.

[68] Y. Mikawa, T. Ebinuma and S. Nakasuka, 'The study of the remote-sensing application using the GNSS reflected signal with the aperture synthesis', *IEEE International Conference on InGeoscience and Remote Sensing Symposium (IGARSS)*, pp. 400–403, 2012.

[69] M. Cherniakov, R. Saini, M. Antoniou, R. Zuo and E. Plakidis, 'Experiences Gained during the Development of a Passive BSAR with GNSS Transmitters of Opportunity', *International Journal of Navigation and Observation*, pp. 1–12, 2008.

[70] R. L. Peterson, R. E. Ziemer and D. E. Borth, '*Introduction to spread-spectrum communications*', New Jersey: Prentice Hall, April 1995.

[71] Y. Mikawa, T. Ebinuma and S. Nakasuka, 'The study of the remote-sensing application using the GNSS reflected signal with the aperture synthesis', *IEEE International In Geoscience and Remote Sensing Symposium (IGARSS)*, pp. 400–403, 2012.

[72] G. Gao, G. Shi and S. Zhou, 'Ship Detection in High-Resolution Dual-Polarization SAR Amplitude Images', *International Journal of Antennas and Propagation*, pp. 1–5, 2013.

[73] G. Gao, G. Shi, L. Yang and S. Zhou, 'Moving Target Detection Based on the Spreading Characteristics of SAR Interferograms in the Magnitude-Phase Plane', *Remote Sensing*, Vol. 7, No. 2, pp. 1836–1854, 2015.

[74] C. Wang, S. Jiang, H. Zhang, F. Wu and B. Zhang, 'Ship detection for high-resolution SAR images based on feature analysis', *IEEE Geoscience and Remote Sensing Letters*, Vol. 11, No. 1, pp. 119–123, 2014.

[75] B. W. Parkinson, *Progress in Astronautics and Aeronautics: Global Positioning System: Theory and Applications*, Aiaa, 1996.

[76] A. El-Rabbany, *Introduction to GPS: the global positioning system*, Artech House, 2002.

[77] B. Hofmann-Wellenhof, H. Lichtenegger and J. Collins, *Global positioning system: theory and practice*, Springer Science & Business Media, 2012.

[78] F. J. MacWilliams and N. J. Sloane, 'Pseudo-random sequences and arrays', *Proceedings of the IEEE*, Vol. 64, No. 12, pp. 1715–1729, 1976.

[79] R. N. Mutagi, 'Pseudo noise sequences for engineers', *Electronics & Communication Engineering Journal*, Vol. 8, No. 2, pp. 79–87, 1996.

[80] B. Sklar, *Digital communications*, NJ: Prentice Hall, 2001.

[81] J. W. Mark and W. Zhuang, *Wireless Communications and Networking*, Prentice Hall, ISBN 0-13-040905-7, 2003.

[82] W. C. Lee, 'Overview of cellular CDMA', *IEEE Transactions on Vehicular Technology*, Vol. 40, No. 2, pp. 291–302, 1991.

[83] A. J. Viterbi, *CDMA: principles of spread spectrum communication*, Addison Wesley Longman Publishing Co., Inc.; 1995.

[84] R. Prasad, *CDMA for wireless personal communications*, Artech House, Inc.; 1996.

[85] M. Martorella, J. Homer, J. Palmer, V. Chen, F. Berizzi, B. Littleton, and D. Longstaff, 'Inverse synthetic aperture radar', *EURASIP Journal on Advances in Signal Processing*, No. 1, pp. 1–4, 2006.

[86] C. Ozdemir, E. Yigit and S. Demirci, 'A Comparison of Focusing Algorithms for Ground Based SAR System', *Progress in electromagnetics research symposium proceedings online*, Vol. 7, No. 1, pp. 21-26, 2011.

[87] E. Rodriguez and J. M. Martin, 'Theory and design of interferometric synthetic aperture radars', *IEE Proc.-F*, vol. 139, no. 2, pp. 147-159, 1992.

[88] F. K. Li and R. M. Goldstein, 'Studies of multi-baseline spaceborne interferometric synthetic aperture radars', *IEEE Transaction on Geo-science and Remote Sensing*, vol. 28, no. 1, pp. 88-97, 1990.

[89] F. Gatelli et al., 'The wavenumber shift in SAR interferometry', *IEEE Transaction on Geo-science and Remote Sensing*, vol. 32, no. 4, pp. 855-865, 1994.

[90] C. Prati and F. Rocca, 'Improving slant range resolution of stationary objects with multiple SAR surveys', *IEEE Transactions on Aerospace and Electronic Systems*, vol. 29, no. 1, pp. 135-144, 1993.

[91] T. Zeng, M. Cherniakov and T. Long, 'Generalized approach to resolution analysis in BSAR', *IEEE Transactions on Aerospace and Electronic Systems*, Vol. 41, No. 2, pp. 461–474, 2005.

[92] M. Antoniou, M. Cherniakov and H. Ma, 'Space-surface bistatic synthetic aperture radar with navigation satellite transmissions: a review', *Science China Information Sciences*, Vol. 58, No. 6, pp. 1–20, 2015.

[93] T. Zeng, T. Zhang, W. Tian and C. Hu, 'Recent progress in Bistatic SAR with illuminators of opportunity', *Science China Technological Sciences*, Vol. 59, No. 12, pp. 1965–1967, 2016.

[94] X. Rao, H. Tao, J. Xie, J. Su and W. Li, 'Long-time coherent integration detection of weak manoeuvring target via integration algorithm, improved axis rotation discrete chirp-Fourier transform', *IET Radar, Sonar & Navigation*, Vol. 9, No. 7, pp. 917-926, 2015.

[95] X. Chen, J. Guan, N. Liu and Y. He, 'Maneuvering target detection via Radon-fractional Fourier transform-based long-time coherent integration', *IEEE Transactions on Signal Processing*, Vol. 62, No. 4, pp. 939–953, 2014.

[96] J. Zhen, Z. Wu and S. Zhang, 'Performance of multi-static SAR system based on GNSS satellite signal', *Journal of Dalian Maritime University*, Vol. 35, No. 2, pp. 43-46, 2009.

[97] J. Zhen, Z. Zhang and S. Wu, 'Study on SNR in GPS satellite signal based on bistatic SAR system', *Radar science and technology*, Vol. 8, No. 2, pp. 119-124, 2010.

[98] T. Zeng, D. Ao, C. Hu, T. Zhang, F. Liu, W. Tian and K. Lin, 'Multi-angle BSAR Imaging Based on BeiDou-2 Navigation Satellite System: Experiments and Preliminary Results', *IEEE Transactions on Geoscience and Remote Sensing*, Vol. 53, No. 10, pp. 5760–5773, 2015.

[99] W. S. Steven, *The scientist and engineers guide to digital signal processing*, California Technical Pub, 1997.

[100] V. Erceg, L. J. Greenstein, S. Y. Tjandra, S. R. Parkoff, A. Gupta, B. Kulic, A. A. Julius and R. Bianchi, 'An empirically based path loss model for wireless channels in suburban environments', *IEEE Journal on selected areas in communications*, Vol. 17, No. 7, pp. 1205–1211, 1999.

[101] H. M. Jol, editor, *Ground penetrating radar theory and applications*, Elsevier, 2008.

[102] G. V. Rosenbaum, 'Determination of GPS RF signal strengths', *2008 IEEE/ION InPosition, Location and Navigation Symposium*, pp. 449–458, 2008.

[103] B. C. Levy, 'Principles of signal detection and parameter estimation', Springer Science & Business Media, July 7, 2008.

[104] H. Kobayashi, B. L. Mark, and W. Turin, *Probability, Random Processes, and Statistical Analysis*, United Kingdom at the University Press, Cambridge, 2012.

[105] Bhuiyan, M. Z. H., Lohan, E. S. and Renfors, M. EURASIP J. Adv. Signal Process. (2007) 2008: 863629. https://doi.org/10.1155/2008/863629.

[106] S. Boyd and L. Vandenberghe, '*Convex optimization*', Cambridge university press, Mar. 8, 2004.

[107] Y. Zheng, 'Spectrum Sensing, Access, and Leasing in Cognitive Radio Networks', Master Thesis, University of Alberta, Canada, 2014.

[108] D. E. Goldberg and J. H. Holland, *Genetic algorithms and machine learning. Machine learning*, Vol. 3, No. 2, pp. 95–99, 1988.

[109] S. Arora and B. Barak, *Computational complexity: a modern approach*, Cambridge University Press, 2009.

[110] B. V. Sukhatme, *Sampling Theory of Surveys with Applications*; Iowa State University Press: Ames, IA, USA, 1954.

[111] S. D. Brown, R. J. Francis, J. Rose and Z. G. Vranesic, '*Field-programmable gate arrays*', Springer Science & Business Media, 2012 Dec 6.

[112] L. G. Valiant, 'A bridging model for parallel computation', *Communications of the ACM*, Vol. 33, No. 8, pp. 103–111, 1990.